# Microstructural Analysis of Additive Manufactured Walls of AA5083 and AA4020 alloys produced by Cold Metal Transfer

Martin Løvøy


Master Thesis
Materials Science and Nanotechnology

Department of Chemistry
The Faculty of Mathematics and Natural Science

UNIVERSITY OF OSLO

May / 2018

## Acknowledgements

This thesis is submitted as a part of the master's degree in Material Science and Nanotechnology by the Department of Chemistry at the University of Oslo (UiO). The experimental work has been performed in the Structure Physics group (Department of physics, UiO) from August 2016 to May 2018.

I would like to give thanks to my three supervisors: Anette E. Gunnæs, Amin S. Azar and Spyros Diplas for their guidance, motivation and interesting discussions through the two most educational years of my life. Furthermore, Ole Bjørn Karlsen, Phuong D. Nguyen and Domas Birenis are thanked for their teaching and for all the great discussions that made me think differently.

I would also like to acknowledge the support from the Research Council of Norway through the Norwegian Center for Transmission Electron Microscopy (NORTEM (197405/F50)), SINTEF, for awarding my work and me the SINTEF Scholarship 2017 and the AddMan-Al group at SINTEF for including me in the project. The presented work would not have been the same without your support.

Thanks to the MENA cohorts of 2011, with whom I started this journey with, and to all of the newer members I have met since then. Also, a thanks to the participants of Structure Physics- and Electrochemistry group at Oslo Science Park, for the numerous lunches, coffee breaks and social events. You all have made these years memorable.

A special thanks to my family. To my mom, dad and sister for believing that I can, to my two aunts- and uncles for cheering me on. To my grandparents for always making me feel appreciated. And last, but not least: To my dear Toini for your everlasting love and support.

## Abstract

Additive manufacturing (AM), also known as 3D-printing, of metals has just recently become possible and fundamental studies are of high interest. In the current project wire arc additive manufacturing (WAAM) by cold metal transfer (CMT) have been used to build three walls with a single weld bead width and heights of about 3, 5- and 5.5 cm tall. Two of the walls are made of the Si rich Al-alloys AA4020 while the third is from the Mn-rich Al-alloy AA5083. Using the same processing parameters, it is seen that the alloy type strongly affect the shape of the walls. The Si-rich alloy pronounced signs of "sagging" while the AA5083 alloy was straighter with only a small bump mid-way up.

The mechanical properties of the walls have been characterised by Vickers hardness- and tensile tests while the microstructure has been characterised by visible light microscopy and analytical scanning and transmission electron microscopy. The goal of the thesis has been to correlate the mechanical properties and the microstructural features observed.

The microstructure analysis of the first wall of AA4020 alloy showed that the wall had layers of higher Si content with complex dendritic networks of crystalline silicon. These layers were measured to be harder in average (≈42HV) than those without the silicon enrichments (≈34HV). In addition, intermetallic particles of $Al_6$(Mn,Fe) and Al(Mn,Fe)Si were found to be situated in between the dendrites. The third wall structure made out of the AA5083 alloy had short edge-fractures at the interface between two beads. In the same area was a region with high concentration of intermetallic particles. The tensile strengths were measured to an average value of ≈310MPa in the horizontal direction and ≈243 in the vertical direction, in which the weld beads are crossed, supporting too little heat during deposition.

## Table of Contents

# 1 Introduction

Additive manufacturing (AM) is a process for constructing structures in a layer-upon-layer fashion. This is one of reasons for why the name AM often is interchanged with the phrase 3D printing. The process is used for cost effective production of different types of components at high precision. By using the AM processing technology, the production becomes more efficient with respect to time and amount of material used. It has a potential high impact factor on several different industries, such as the automotive-, consumer products-, medical- and aerospace-industry. These and several other industries could benefit from AM production by the means of cost and also by the free-form ability AM provides. Free-form production makes it possible to produce complex structures, which provides a higher degree of design-freedom. This kind of freedom appeals to the niche-marked, where a low-volume need usually means high costs. The ability to produce complex structures provides the ability to reduce the weight of certain components by design. It also permits the use of more expensive materials without any substantial cost-increase, due to better design and less material waste. A selection AM production systems are mobile, which gives the opportunity of on-site parts production. Production of this kind would be of great interest for remote workplaces such as oilrigs and ships, where critical parts are a long distance away. [1-6]

The AM technology is a complementary, and in many cases a substitute method for conventional subtractive methods such as computer numerical control (CNC) machining. In these subtractive methods, a large piece of material is fastened to a bench and a cutting device is positioned close to the fastened object in order to remove the material from it. By rotating either the object or the cutting device, the material is made into the desired shape according to the requested designed specification. However, the processes produces fine debris and metallic chips, which entail a longer and costlier value chain to recycle and reshape them back into a useful product. Therefore, subtractive manufacturing methods lack sustainability and efficiency, at least from an energy consumption viewpoint [7].

The ability of parts-repair is another great achievable benefit of AM, which will improve the efficiency in the complete production-chain.

## 1.1 The General Process of Additive Manufacturing of Metals

The AM process of metals is generally based upon the concept of joining metal through a selection of processes, in order to produce a finished product. The American Society for Testing and Materials (ASTM) defines AM of materials as "*The process of joining materials to make objects from 3D model data, usually layer upon layer, as opposed to subtractive manufacturing technologies*" (ASTM-F2792-10 E. Herderick) [6]. Most products produced by AM is said to be near-net shape products. That is, the product will have a minimum need of post-processing, if any. Although the concept of joining metal is valid for the general process, the many varieties of processing techniques, technologies and equipment makes the AM process of very non-general. Several different AM-techniques are developed and the hierarchy below (figure 2.1) shows a selection, along with the route of interest for this project (highlighted in red).

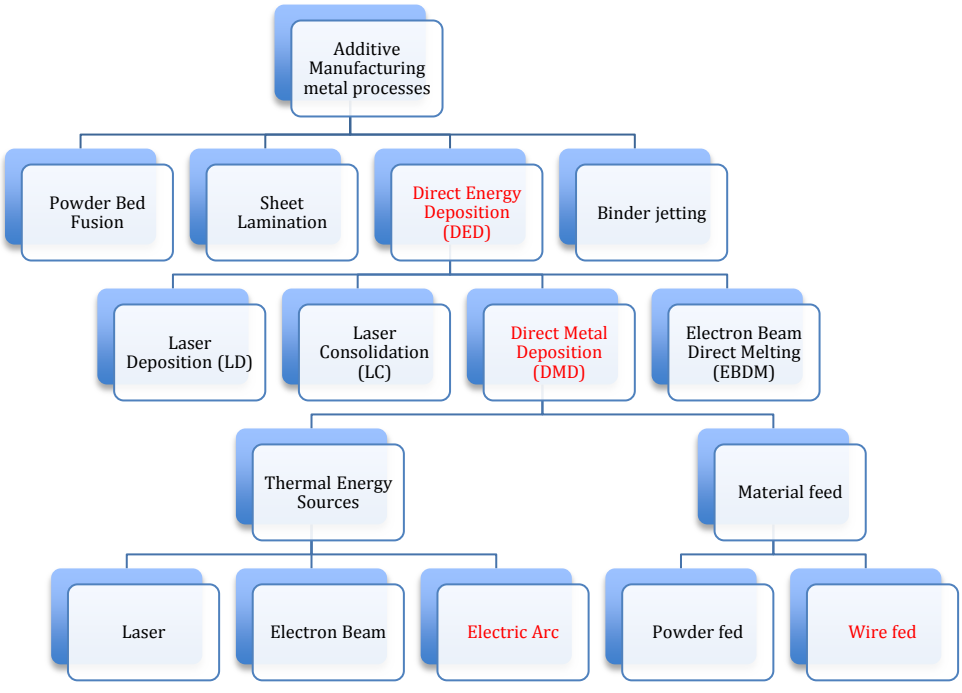


Figure 2.1: A simplified hierarchy displaying the AM route of interest.

As the hierarchy shows (figure 2.1), the process of interest for this project is the *Direct Energy Deposition (DED)* with a *Direct Metal Deposition (DMD)* technique. The material to-be deposited is *Wire fed* and thermally melted by an *Electric Arc*. As a consequence of the above, the process studied in this thesis would be better defined as *"Wire Arc Additive Manufacturing (WAAM)"*. However, as the following theory chapter will explain that this is not an outright description [7, 8]

## 1.2 Motivation for the project

AM has since the late 1980s been a method for rapid-prototyping (RP), a method for modelling of the finished product. Within the last 25 years the AM technology has developed from an RP-method to an important industrial process of producing final parts [7]. The AM technology is still under great development with regards to equipment optimization and material selection. This thesis will deal with the latter challenge, where aluminium alloys are investigated, more specifically the AA4020- and the AA5083-alloy. The use of these alloys will expand the potential applications of AM production.

# 2 Theory

This chapter will introduce the reader to the most essential theory necessary to understand and reflect upon the results presented. It is advised to refer to the suggested references for additional information on to topics. In addition to the presented theory in this chapter, complementary theory will be given whenever it is assumed to be unavoidable during the presentation of the results.

The presented theory will elaborate on the concepts behind the welding-technology that is used. It will also introduce aluminium alloys, especially the two alloys that have been investigated. Furthermore, the chapter will include the theory behind the experimental instruments and techniques which has been used.

## 2.1 Welding

Chapter 1 introduced the concept of additive manufacturing (AM) and the route of interest. This led to a general description of the process that is used in this project, which is; Wire Arc Additive Manufacturing (WAAM). Within this description are the underlying concepts of, direct energy deposition (DED) and direct metal deposition (DMD), which will be explained by the following sub-chapters. It was initially stated that WAAM was not an outright description, and this statement will be justified.

### 2.1.1 Direct Energy Deposition (DED) and Direct Metal Deposition (DMD)

The AM process studied is based upon the process of *Direct Energy Deposition (DED)*. The process can be described as a heat source that directly melts the metal that is to-be deposited.

The most common heat sources are *Laser*, *Electron Beam* and *Electric Arc*. The main difference is the confinement of the thermal radiation. The laser and the electron beam have the most confined radiation, which makes it possible to process the material with very high precision.

The electron beam has the most confined radiation of the two, but high-precision electron beams demands special conditions such as vacuum and an inert environment. The most desirable feedstock for the laser and the electron beam is powder due to the high surface area and small grains of metal. A feedstock is the raw material, which is melted during the DED- and DMD process. The result is a melt arising at lower temperatures, while the high precision is retained. [2, 8, 9]

Melting a solid metal wire or powder is the basic concept of *Direct Metal Deposition (DMD)* and doing so with an electric arc is a more straightforward and faster way of processing the material. The general process of welding with an electric arc can be explained by the following. An electric current flows from the welder and through the wire, at a certain, close distance from the base metal it short-circuits with the grounded substrate, hence creating an electric arc. Because of the continuous wire feed, the arc remains during operation. In addition, to avoid impurities from the air, a shielding gas is continuously flowing out of the nozzle during welding. The shielding gas usually consists mainly of argon, but gas mixtures are also common.

Figure 2.2 below illustrates, the whole process takes place from the tip of what is known as the "swan neck" of the welder. The illustration shows the three incoming sources necessary for the welding process, a solid wire electrode, a current conductor and a shielding gas tube. The shielding gas tube ends within the swan neck, which makes the gas flow out of the nozzle and surrounding the rest of the process. The wire electrode makes contact with the current conductor at the outermost part of the nozzle. The contact between the two electrifies the wire. When the electrified wire gets close to the base metal, an electric arc occurs. The work distance, often referred to as; contact-to-wire-distance (CTWD), is an important parameter for welding. A high CTWD yields a low temperature of the weld pool (molten metal that make up the weld), at the expense of less penetration. Too high CTWD can also cause the weld pool to pile up, instead of fusing to the base material. A low CTWD causes a higher heat transfer and will make the molten material to spread out more. It will generally fuse more in to the base material, but too much heat will melt it. It is therefore important to find a good balance between the two extremes. The CTWD will depend on the other parameters of the welder, such as voltage, current, wire feed speed, travel speed and of course the metal.

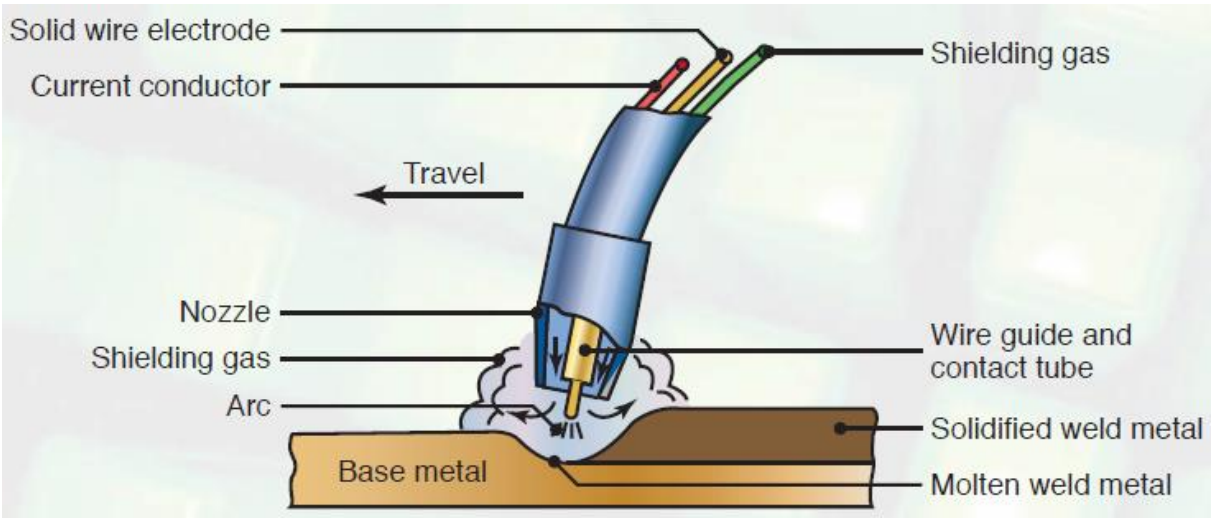


Figure 2.2: A simplified illustration of the “swan neck” of the welder. Adapted from [10]

The illustration in figure 2.2 is of course a very simplified drawing of the equipment that is used in the AM process. A real piece of equipment used in AM is shown in figure 2.3 below.

Figure 2.3: Illustration of a Fronius CMT robotic welder. Adapted from [11]

Figure 2.3 illustrates a multiple-axis robotic welder, which means that it is free to move in multiple directions. This enables welding in the horizontal, vertical and almost any direction in between. The device next to it is the wire feeder. The wire feeder provides the “swan neck” (at the tip of the robot) with current, shielding gas and weld wire.

### 2.1.2 Cold Metal Transfer (CMT)

There are main challenges in the process of AM of aluminium. One is the low melting point of aluminium, which sets high demands for arc stability. The second is to join material with previous joined material and by this building a structure in three dimensions. Cold metal transfer (CMT) is a method developed specifically to address these issues.

CMT is based on transferring and joining the metal at lower temperatures than those of the basic process. Thus, avoiding the molten material to spread out and causing the structure to sag. In CMT welding, the wire feeder is converted in to a dynamic process that retracts the wire as soon as it has short-circuited, and then pushes it towards the substrate to form an arc again. This movement reduces the heat transfer, because the arc is cut off in after a molten metal droplet is formed. Figure 2.4 is an illustration of the CMT process where the arrows indicate the direction of the wire movement. It shows how the arc is formed during the first downward wire-movement and how it is cut off when the droplet is formed. After droplet formation, the wire retracts and thus, leaving the molten material. The motion is then repeated [12, 13]

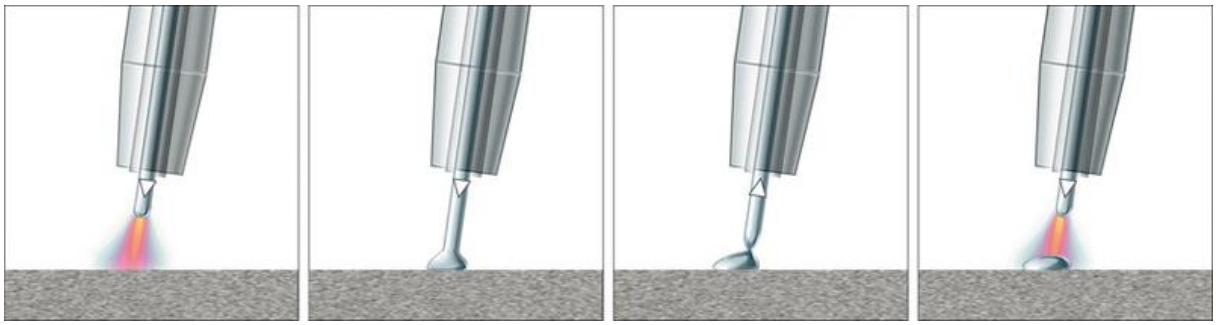

Figure 2.4: Illustration of the general CMT process. The arrows show the movement of the wire as the weld bead is deposited. Adapted from [14]

There are several sub-technologies of CMT that exploit this concept of wire feed. The one used as a part of this project is named *CMT Advanced*, which is illustrated in figure 2.5. This process combines the general CMT process with a reversal of the polarity of the current that passes through the wire. This leads to a two-stage arc formation. One as the wire goes down against the substrate, and another when the wire is pulled back up. During the retraction of the wire, the polarity of the current is reversed, resulting in a

second arc formation. This sub-technology is said to improve the arc stability, which means that the heat transfer caused by the electric arc is more consistent, and thus producing a better weld. Also, the heat input is reduced even more compared to the regular CMT.

The mechanism is better understood by the following illustration (figure 2.5). The figure shows the wire-motion, recognized by the black rod and the directional arrows, and the associated current polarity (plus and minus signs). By the blue "cloud", the figure indicates at which point the electric arc is formed.

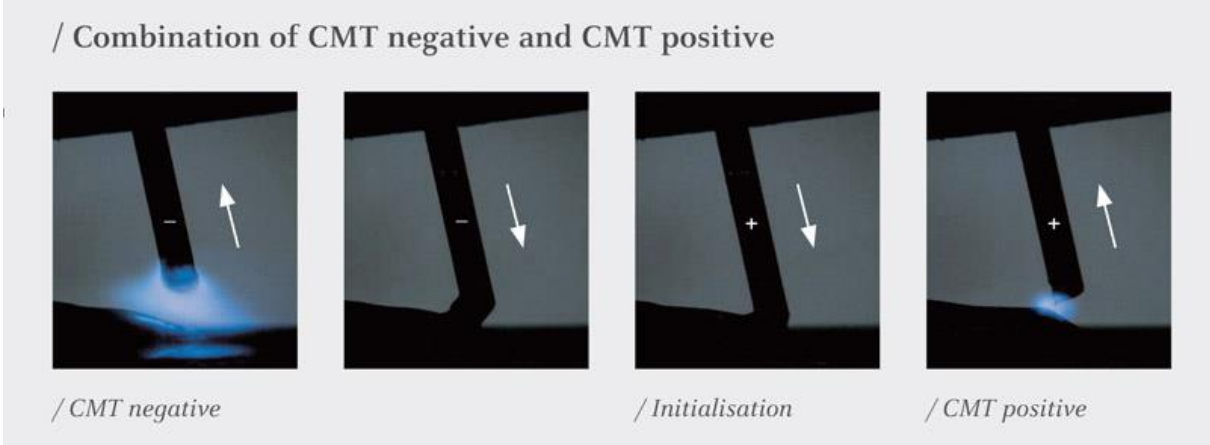


Figure 2.5: Illustration of the CMT-advanced. The arrows shows the wire movement, whilst the plus and minus signs shows the polarity of the wire. The blue "clouds" indicates arc formation. Adapted from [17]

To be able to not only weld two pieces of metal together, but welding a continuous structure in three dimensions, one will have to set all the parameters of the welder perfectly. The most basic welders have three settings; current, wire speed and gas flow. In addition to these, parameters such as working distance, travel speed and the direction of travel, is controlled manually by the weldor. CMT is developed for the challenges of construction in three dimensions, but adds even more parameters to optimize [12, 15-17].

Because the technology of CMT greatly improves the welding process and holds some of the most crucial properties necessary for AM, the better description of the complete manufacturing process would be *Wire Arc Additive Manufacturing by Cold Metal Transfer* (WAAM CMT).

## 2.2 The 4xxx and 5xxx series aluminium alloys

In this section and the following subsections, the aluminium alloys that have been used to produce the samples will be briefly accounted for as well as the general properties of the alloy series they belong to. There are eight different series or classes of the wrought aluminium alloys and because there are a numerous number of differences, with regards to e.g. secondary alloying elements, within each of the series, the classification is generally designated as 1xxx - 8xxx. The first number directly relates to the main alloying element and the x's belongs to the rest of the alloying elements and in some cases, special characteristics to make them easier to distinguish. The theory is based on the presented work of L. F. Mondolfo [18], J. R. Davis [19], J. Gilbert Kaufman [20] and A. Johansen [21].

The alloy-series of interest for this project is the 4xxx- and 5xxx-series alloys. Their main characteristics will briefly be accounted for below

### The 4xxx series alloy

The *4xxx* series aluminium alloy is the common group name for the alloys that have silicon (Si) as their main alloying element. Silicon-addition to the aluminium provides better fluidity of the molten material and lowers the melting temperature. Furthermore, silicon reduces the shrinkage of the material during solidification. The mechanical properties is highly dependent on the silicon content of the alloy, which can, for the 4xxx series, be up to 25wt% [18-20].

### The 5xxx series alloy

The *5xxx* series aluminium alloys are the common group name for those of the aluminium alloys that have magnesium (Mg) as their main alloying element. The addition of magnesium provides mechanical strength to the aluminium as well as exceptional corrosion resistance. Even though those properties have been enhanced, other important properties such as ductility, formability –and probably the most important property for this project, weldability, are kept at a high level. Throughout the series of the 5xxx alloys, the concentration of Mg is ranging from ≈0.5wt% up to ≈13wt%[18-20].

Although the main alloying element is responsible for the main characteristics of the alloys, the secondary alloying elements provides the alloy with additional properties. The secondary alloying elements are not necessarily added intentionally, but can be bi-products from the production of the raw material. Nevertheless, these secondary elements will yield some kind of property, and thus, the most common is shortly accounted for below.

### Common Alloying elements

#### Iron (Fe)

Iron is generally considered an impurity element. It is considered an alloying element, because it is difficult and expensive to produce aluminium without iron contamination. It is almost always present, and has to be accounted for. Its effect on the alloy is detrimental with regards to ductility and corrosion resistance. A common intermetallic that Fe forms with presence of manganese (Mn), is the $Al_6$(Mn,Fe)-phase [18, 22]

#### Manganese (Mn) and Chromium (Cr)

Manganese is added as an alloying element to correct for the corroding effects of iron. It will also improve the strength and control over the recrystallization. Manganese forms large constituents during solidification. Chromium has a similar effect on the alloy, just stronger. It is often added together with Mn [18, 22].

#### Copper (Cu)

Added to improve the strength and the fatigue resistance. However, Copper decreases the corrosion resistance and weldability; therefore, it is usually added in small amounts (0-5wt%) [18, 22]

#### Magnesium (Mg)

Magnesium is the main alloying element of the 5xxx series alloys. In the other alloys it is added to increase the strength and corrosion resistance. The ductility decreases with addition of Mg, thus, small amounts are usually added (0-2wt%) in other alloys [18, 22]

**Titanium (Ti)**

Titanium is added to work as a grain refiner. Together with aluminium it forms intermetallic phases [18, 22].

**Silicon (Si)**

Silicon is the main alloying element of the 4xxx series alloys and it is often considered an impurity element in the 5xxx series alloys. In some varieties of the 5xxx-series alloys it is added intentionally to increase the fluidity, which is the general purpose of silicon addition in all of the alloys [18, 22]

### 2.2.1 AA4020 alloy

The 4xxx series alloy that has been studied in this project is the aluminium alloy (AA) AA4020 or ISO: AlSi3Mn1, depending on the nomenclature. The chemical composition, listed in wrought state in table 2.1, is not entirely reflected by the ISO name; therefore, the naming will proceed as AA4020. The alloy have been chosen because of its high degree of weldability, finishing characteristics and the wide range of applications it can be used for. Examples of applications is suggested below the table.

#### Chemical Composition

**Table 2.1 - Listed chemical composition of wrought AA4020 aluminium alloy [provided by SINTEF]**

| Element: | Si | Fe | Cu | Mn | Mg | Ti | Be | Others | Al |
|---|---|---|---|---|---|---|---|---|---|
| [wt%] | 2.5-3.5 | <0.20 | <0.30 | 0.8-1.2 | <0.01 | <0.005 | <0.0003 | <0.02 | Rest |

#### Applications

The high silicon content of the 4xxx series alloys yields a high flowability. This is good for applications such as plug welding[1] where it acts as a filler weld. Plug welding is widely used in the automotive industry, where aluminium has become a desired metal. The 4xxx series alloys are also widely used for forging of for instance aircraft pistons (AA4032). It is said to be readily weldable through common techniques such as gas metal arc welding (GMAW), which was presented in chapter 2.1 [19-21].

[1] Welding technique where two pieces of metal is joined through a punched hole in an upper metal plate.

### 2.2.2 AA5083 alloy

The 5xxx series alloy in this study is the AA5083 alloy, or ISO: AlMg4.5Mn. The choice of this alloy is due to its properties such as, toughness, corrosion resistance, weldability, and its wide range of applications. Examples of applications are suggested below and the listed chemical composition of the wrought alloy is shown in table 2.2 [19-21].

#### Chemical composition

**Table 2.2 - Listed chemical composition of wrought AA5083 aluminium alloy [provided by SINTEF]**

| Element: | Mg | Mn | Fe | Zn | Cu | Si | Cr | Ti | Others | Al |
|---|---|---|---|---|---|---|---|---|---|---|
| [wt%]: | 4.3-5.2 | 0.4-1.0 | <0.4 | <0.25 | <0.1 | <0.2 | <0.05 | <0.15 | <0.15 | Rest |

#### Applications

The 5xxx series aluminium alloys are, as stated, one of the most corrosion resistant of all aluminium alloys as well as being of those with the highest mechanical strength. Because of these facts, the applications are often related to parts and constructions that have to withstand harsh environments such as open atmosphere and seawater. Typical examples of applications are highway structures, bridges, storage tanks, pressure vessels, cryogenic systems for temperatures as low as -270°C and marine applications in general. The 5083 alloy is also readily weldable, which means that the alloy in the study is used as a weld filler and for general welding as such [19-21]

## 2.3 Crystallography

This section and its subsections are based on the theory by C. Kittel [23], P. C. Hemmer [24] and R. J. D. Tilley [25]. The reader is encouraged to refer to these books in order to gain a full understanding of the topics. Only the most essential concepts are presented below.

Materials such as diamonds, calcites and most metals are known for being crystalline. The structure of a crystal can be described by the smallest repeating element(s), the *motif*, and an array of regularly arranged discrete lattice points in an infinite vector space. One such three-dimensional array, that remains invariant under translation by any vector $\mathbf{T}_{uvw}$, is called a *Bravais lattice*. There are 14 Bravais lattices, and a combination with the motif generates the *unit cell* of the crystal. The unit cell is therefore, the smallest repeating unit that can completely define the entire crystal structure. However, a real crystal is not constructed until a motif of atoms is defined.

The relation in (eq. 2.1) defines a real lattice vector. It describes that at any lattice point, chosen to be the origin, any other lattice point can be defined as

$$\boldsymbol{R}(uvw) = u\boldsymbol{a} + v\boldsymbol{b} + w\boldsymbol{c} \quad u.v,w \in \mathbb{Z}, \qquad \text{(eq. 2.1)}$$

where **a** ,**b** and **c** are the *basis vectors* that spans a volume, whose edges of length $a_0$, $b_0$ and $c_0$ defines the unit cell.

In addition to the above, certain symmetry operations can be applied. Combinations of the three main operations, rotation axis, mirror planes and center of symmetry, returns the 32 crystallographic point groups. The complete symmetry of the inner structure is found through a combination with the 14 Bravais lattices, which yields the 230 space groups.

### 2.3.1 Reciprocal space

When studying crystals through diffraction of photons, x-rays, neutrons or electrons, it is common to encounter what is known as the reciprocal space. The reciprocal space is often explained through the description of the lattice. A definition states; *«the reciprocal lattice of a given Bravais-lattice, is the set of all vectors* $\vec{g}$ *that produces planar waves* $e^{i\boldsymbol{gR}}$*, while preserving the periodicity of the Bravais-lattice»* (P. C. Hemmer, s33.) [24]. As a consequence, the planar wave is invariant under translation by any lattice vector $\mathbf{R}_{i+1}=(\mathbf{R}_i+\mathbf{r})$, hence the reciprocal lattice vectors, $\boldsymbol{g}$, is determined by

$$e^{i\boldsymbol{gR}} = 1, \qquad \text{(eq. 2.2)}$$

for all lattice vectors **R.** The reciprocal lattice vector **g** is given as

$$\boldsymbol{g} = h\boldsymbol{a}^* + k\boldsymbol{b}^* + l\boldsymbol{c}^*, \qquad \text{(eq. 2.3)}$$

where *h*, *k* and *l* are the integers named *Miller indices*, which describes lattice planes, and **a***, **b*** and **c*** the *reciprocal basis vectors*. These relate to the real space basis vectors by the following three expressions,

$$\boldsymbol{a}^* = \frac{\boldsymbol{b}\times\boldsymbol{c}}{V_{uc}},\ \boldsymbol{b}^* = \frac{\boldsymbol{c}\times\boldsymbol{a}}{V_{uc}},\ \boldsymbol{c}^* = \frac{\boldsymbol{a}\times\boldsymbol{b}}{V_{uc}}, \qquad \text{(eq. 2.3)}$$

where $V_{uc}$= $\mathbf{a}\cdot(\mathbf{b}\times\mathbf{c})$ is the volume of the unit cell. Furthermore, the dot product of the reciprocal- and real space basis vector have the property of

$$\boldsymbol{a}^* \cdot \boldsymbol{a} = \boldsymbol{b}^* \cdot \boldsymbol{b} = \boldsymbol{c}^* \cdot \boldsymbol{c} = 1, \qquad \text{(eq. 2.4)}$$

whilst a mix yields zero, e.g. $\boldsymbol{a}^* \cdot \boldsymbol{b} = 0$.

### 2.3.2 Planes and directions

As stated, *h, k* and *l* are known as the Miller indices. These indices describe the lattice planes in real space and thus, the reciprocal lattice points in the reciprocal space. A lattice plane in the real space is denoted *(hkl)*, where the indices corresponds to the intersection with the unit cell axes, **a**, **b** and **c**, at the positions $1/h$, $1/k$ and $1/l$, respectively. In the case of intersections at infinity, $1/\infty$, the indices are denoted 0. The set of equivalent planes has the collective notation $\{hkl\}$. Furthermore, a direction in a crystal is written as $[uvw]$, and equivalent directions as $\langle uvw \rangle$. Finally, the direction shared by two planes when they intersect, is called the *zone axis* (ZA). That is, the zone axis is perpendicular to the plane normal $(hkl)$ that encloses the zone. The following relation is known as the *zone law*

$$uh + vk + wl = 0 \qquad \text{(eq. 2.5)}$$

## 2.4 Scattering and diffraction

The following theory compressed and will just briefly elaborate what is necessary to understand the presented results. Therefore, for a better understanding and general interest, the reader is recommended to refer to the books by C. Kittel [23], P.C. Hemmer [24] and and David B. Williams & C. Berry Carter [26] which is used as the main sources of information to this section.

Scattering is a process in which a particle (e.g. an electron) interacts with matter and deviates from its initial trajectory. There are two main scattering processes, named *elastic*- and *inelastic* scattering, which refer to scattering without transfer of energy, and transfer of energy, respectively. Diffraction is often referred to as the wave-opponent to the scattering process. That is, diffraction is the alteration of waves by interaction with matter. As a consequence, the scattering processes of elastic –and inelastic scattering is translated to their wave-synonyms, namely *coherent*- and *incoherent* scattering.

It should be mentioned that diffraction very often refers to a microscopy-technique, in which diffraction patterns (DP) are generated. In this case, diffraction is related to the *coherent* electron waves after interaction with matter.

### 2.4.1 Laue condition and Bragg's law

In 1913, Max von Laue suggested that waves of much shorter wavelengths than electromagnetic radiation would cause diffraction or interference when passing through a crystal. The hypothesis was successfully proved by an X-ray experiment performed by Paul Knipping. Von Laue further explained the hypothesis through a light-optics experiment. He argued that the diffracted waves would be in phase, if the path difference between the scattered waves of adjacent scattering centers were of integer lengths. Parallel with von Laue's optical experiment, Bragg and Bragg (father and son) proposed a simplification of von Laue's argument. They suggested that the waves reflected off adjacent scattering centers would remain in phase, if the path difference were equal to integral number of wavelengths.

Most of the work in this thesis, which includes these two concepts, is performed on electron microscopes. Hence, the reciprocal space has to be introduced into the equations.

The von Laue condition states that diffraction from a crystal may only occur if

$$\boldsymbol{k}_f - \boldsymbol{k}_i = \Delta\boldsymbol{k} = \boldsymbol{g} \qquad \text{(eq. 2.6)}$$

, where $\boldsymbol{k}_f$ is the diffracted, final wave and $\boldsymbol{k}_i$ is the initial, incident, wave. That is, the change of the wave vector due to diffraction is equal to a specific reciprocal lattice vector, $\boldsymbol{g}$, as defined in equation 2.6. As a consequence, Bragg's law, restricted by Laue's condition, can be deduced. The geometry of figure 2.7 below, can be described by the following relation

$$\Delta\boldsymbol{k} = 2\boldsymbol{k}sin\theta = 2\frac{1}{\lambda}sin\theta \qquad \text{(eq. 2.7)}$$

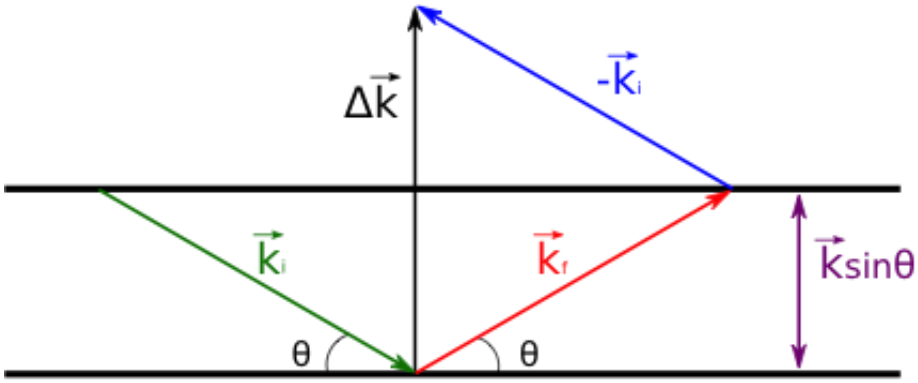


Figure 2.7: Illustration of the relationship between $\Delta\dot{k}$ and $\theta$ for elastic scattering. $\dot{k}_i$, and $\dot{k}_f$ represent the incident –and the final wave vector. The spacing between the planes is defined by $\dot{k}\sin\theta$. The horizontal black lines represent lattice planes.

The distance between the two planes may be expressed as

$$d_{hkl} = \frac{1}{|\boldsymbol{g}_{hkl}|} \qquad \text{(eq. 2.8)}$$

by geometry consideration of a (*hkl*) plane and the equation 2.6. A combination of the equations 2.7 and 2.8 returns Bragg's law

$$2dsin\theta = \lambda \qquad \text{(eq. 2.9)}$$

The Greek letter λ is the wavelength of the incident wave, whose magnitude will differ by the source of radiation. In the case of electron, this wavelength is defined as

$$\lambda = \frac{h}{E^{1/2}}, \qquad \text{(eq. 2.9)}$$

where $h$ is Planck's constant and $E$ is the energy of the electron in $[eV]$. Resultantly, the wavelength of a 200keV electron is approximately 2.7 pm.

### 2.4.2 Dynamic and kinematic scattering conditions

Dynamic- and kinematic-scattering conditions refer to the number of times the electron is scattered, when penetrating the specimen. A single scattering event is referred to be under *kinematic* scattering conditions. To fulfil such conditions, the sample has to be very thin. That is, the condition is dependent on the mean-free-path of the electron through the specimen. A typical value is a few tens of *nm*, with the acceleration voltages obtained by electron microscopes. If the specimen, or an area on the specimen is thicker, the electrons will be scattered multiple times. The conditions are then *dynamical*.

## 2.5 Electron Microscopy

Electron microscopes (EM) utilize the electron wave-particle duality (deBroglie 1925) [27] in order to analyse specimens of different kinds. Max Knoll and Ernst Ruska proposed the first EM in *1931*, reportedly without knowing of deBroglie's proposition from a few years earlier. Since then, the EM have been developed and improved greatly and they are of the important for the future's demand of materials characterization, and nanotechnology. This and the following subchapters on instrumentation and characterization techniques with electron microscopes are based on the theory in the books of Yang Leng [28] and David B. Williams & C. Berry Carter [26].

A great advantage of EM's is that the sample under investigation can be both observed and chemically analysed in the same instrument, given that it has the right equipment to do so. The EM's that have been used in this project is the *scanning electron microscope (SEM)* and the *transmission electron microscope (TEM)*; consequently these will be elaborated further below.

EM's, like the SEM's and the TEM's, often have a vertical columnar setup with some similarities. The electron source is usually mounted at the top of the microscope. The electron source is very often referred to as the *electron gun,* because it emits electrons with high energy. There are two types of electron guns that are commonly used, a *thermionic gun (TG)* and a *field emission gun (FEG)*, the latter is becoming more and more popular due to the better resolution it provides. The main difference between them, in terms of how they function, is that the TG acts almost like a light bulb with a filament that is heated, which in turn emits electrons. A common Schottky-FEG are not too different. It is also heated to some extent, but an electromagnetic field close to the filament helps to extract the electrons. The result is a narrower energy spread of the electrons with the FEG, than with a TG ($\Delta E_{S\text{-}FEG}$=0.7eV *vs.* $\Delta E_{TG\text{-}LaB6}$=1.5eV, where S-FEG=Schottky-FEG and TG-$LaB_6$=thermionic gun with $LaB_6$ filament)(W&C, p. 74) [26]. On the downside, the FEG's produces fewer electrons than the TG, which could be disadvantageous for some purposes.

After the initial emission, an electromagnetic accelerator further accelerates the electrons. This accelerator increases the electron energy, and thus the velocity, to energies ranging from a few hundred eV up to more than 1000 keV [29]. Lenses are used in order to focus the fast travelling electrons from the source onto the sample

As with the visible light microscopes (VLM), numerous lenses are fixed consecutively to alter the path of the radiation, which in the end gives a magnified image of the sample. Contrary to the VLM's, which uses glass lenses to alter the visible light, the EM's uses electromagnetic lenses to alter the electrons. When the electrons finally hit the sample, several interactions occur, and it is the detection of these that makes up the analysis itself, whether it is an image, chemical composition analysis or conduction band measurements. This is where most of the similarities end, because, although both the SEM and the TEM are electron microscopes, do they differ greatly with regards to both the setup, and the detection of the electron-interactions with the sample. An elaboration of the two EM's continues below.

### 2.5.1 The Scanning Electron Microscope

In an SEM, the electrons are converged in to a cone-shape that probes the sample surface. The probe is moved to another area and continues to do so in a step-wise manner. This movement is called scanning because the electron probe scans the surface and supplies the detection systems with signals. For imaging, the two main sources of signal originates from the *elastically* –and *inelastically* scattered electrons. In SEM imaging terms, these two types of scatter are called *backscattered electrons (BSE)* and *secondary electrons (SE)*, respectively. The backscattered electrons are those who have been scattered to high angles, and consequently the detectors are positioned above the sample, concentrically around the electron beam.

The amount of electrons that reaches back to the detector is highly dependent on the average atomic number, $\bar{Z}$, of the interaction volume at each electron probe position. Therefore, the BSE's provides information related to differing composition, such as different phases or particles, as well as thicknesses.

In addition, the number of BSE's that hits the detector is also dependent on the crystal orientation, yielding crystallographic orientation information, an analysis method named; *electron backscatter diffraction (EBSD)*. The BSE's provides signal from a relatively large part of the total interaction volume, and thus, the produced image will consist of information from relatively deep in to the sample.

Changing the acceleration voltage will vary the interaction volume, that is, increasing the acceleration voltage yields an increase of the total interaction volume. The interaction volume will also be affected by different elements in the sample, where the higher $\bar{Z}$ limits the depth of penetration.

As a result of inelastic scattering and excitation of electrons from the specimen, the SE's have less energy than the BSE. Although SE's are produced in most of the total interaction volume, only the SE's originating from the shallower depth of the sample is able to reach the detector, a consequence of the electrons short *mean-free-path* in the sample. The produced SE's are scattered in all directions, and those who manage to escape the specimen will have randomly distributed trajectories. In order to detect these, a positively charged faraday cage is mounted in front of the detector's scintillator, to attract the electrons. This is the most common SE-detector and it is named an *Everhart-Thornley detector (E-T detector),* after its creators.

Because the SE's that reaches the detector have been exceedingly limited by the mean-free-path, the signal that is produced originates from the uppermost part of the specimen, resultantly, the formed SE-image is sensile to topography –and morphology changes.

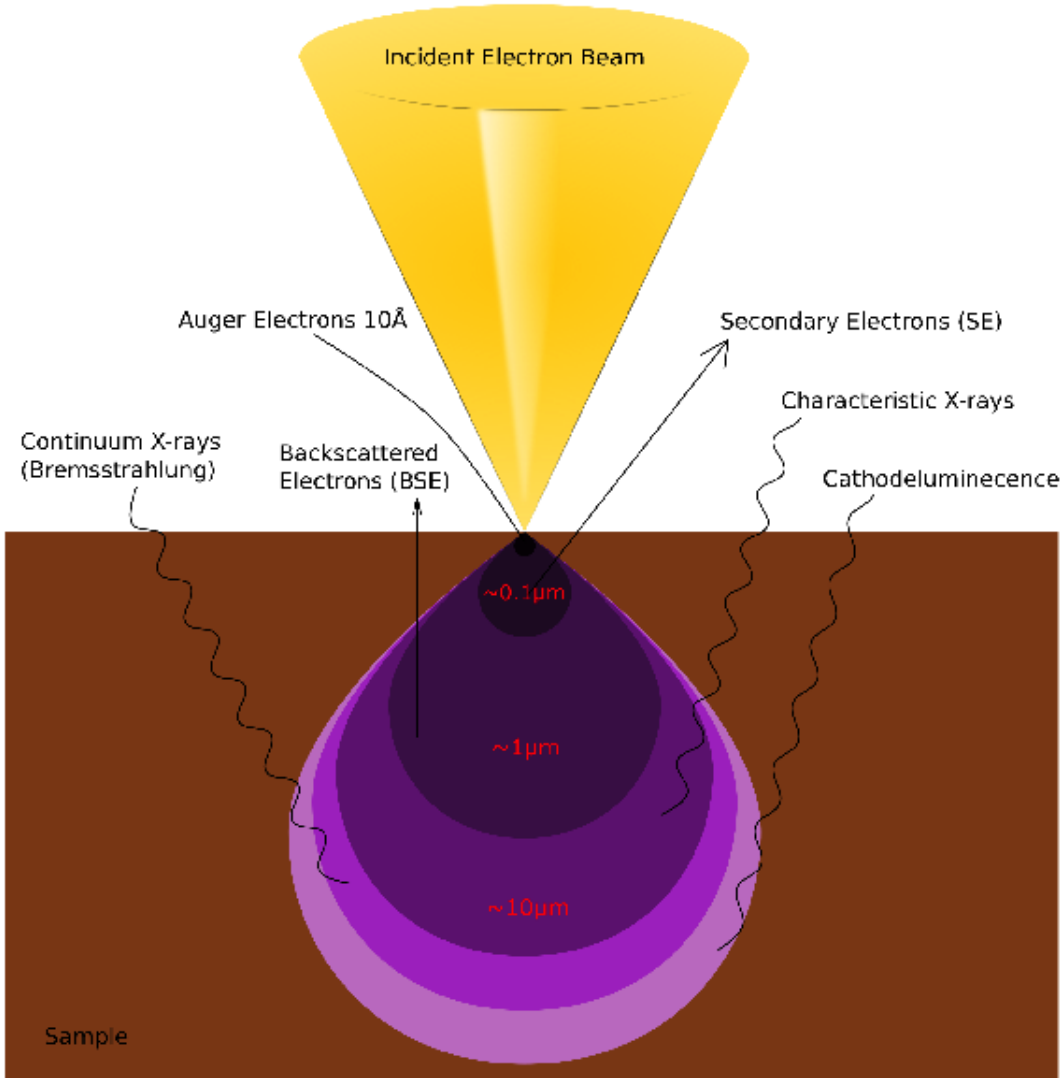


Figure 2.8: Illustration of a typical SEM interaction volume at 20keV acceleration voltage.

Since the two types of signal yields different information in the resulting image, the two images are often set together to form a third, mixed image. The mixed image will then contain information of both the chemical composition and topography/morphology. Figure 2.9 show the different imaging modes, BSE, SE and MIX.

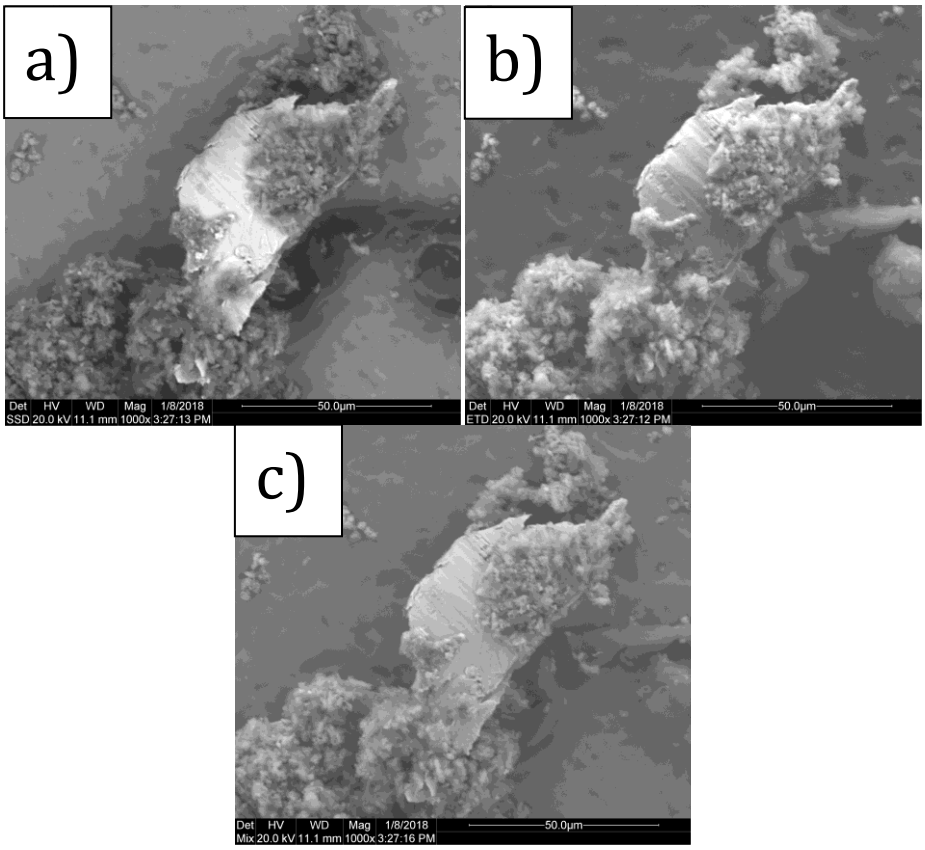


Figure 2.9: The effect of observation modes on an iron rich particle surrounded by AA5083 aluminium alloy. a) BSE image collected with a *Solid State Detector (SSD)*. b) SE image collected with an *E-T detector*. c) BSE and SE forming a MIX-image.

### 2.5.2 The Transmission Electron Microscope

In a TEM, the image formation happens below the specimen, and thus, the electrons have to transmit the sample. In order for them to do so, the sample have to be very thin, preferably less than 100nm. Prior to the sample interactions, the accelerated electron beam (commonly: 60-300 keV) is deflected by electric fields and several electromagnetic lenses, limited by an aperture(s) and in some instruments, monochromated. After interacting with the sample, the beam is again deflected by another set of lenses. These serve the purpose of image formation, e.g., magnification. The final image is projected on to a *fluorescent screen* or a *Charge Coupled Device (CCD)*, the latter enables computer screen observation. Because the TEM consists of several different sections, where each of them serves their own purpose, it is common to divide the microscope in to four individual systems that collectively makes out the instrument. The four systems, from the top are the *electron source system, the illumination system, the objective system* and *the projection system.*

**Experimental techniques**

It is common to distinguish between *conventional* TEM-mode and *scanning transmission electron microscopy (STEM)*-mode. In conventional TEM-mode, the electron beam is adjusted in order to get it as parallel as possible before it hits the sample. The technique enables *bright field (BF)* –and *dark field (DF)* imaging, which is imaging of the forward scattered electrons, and the scattered electrons, respectively. In addition, conventional TEM-mode enables diffraction imaging, where the *back focal plane (BFP)* is projected on to the viewing screen. In STEM mode, the beam in converged into a cone, which is scanned over the specimen, similar to the SEM. The following sub-sections will briefly describe the theory behind the experimental techniques that have been performed on the TEM. The difference with regards to the nature of incident beam is shown in figure 2.10 below.

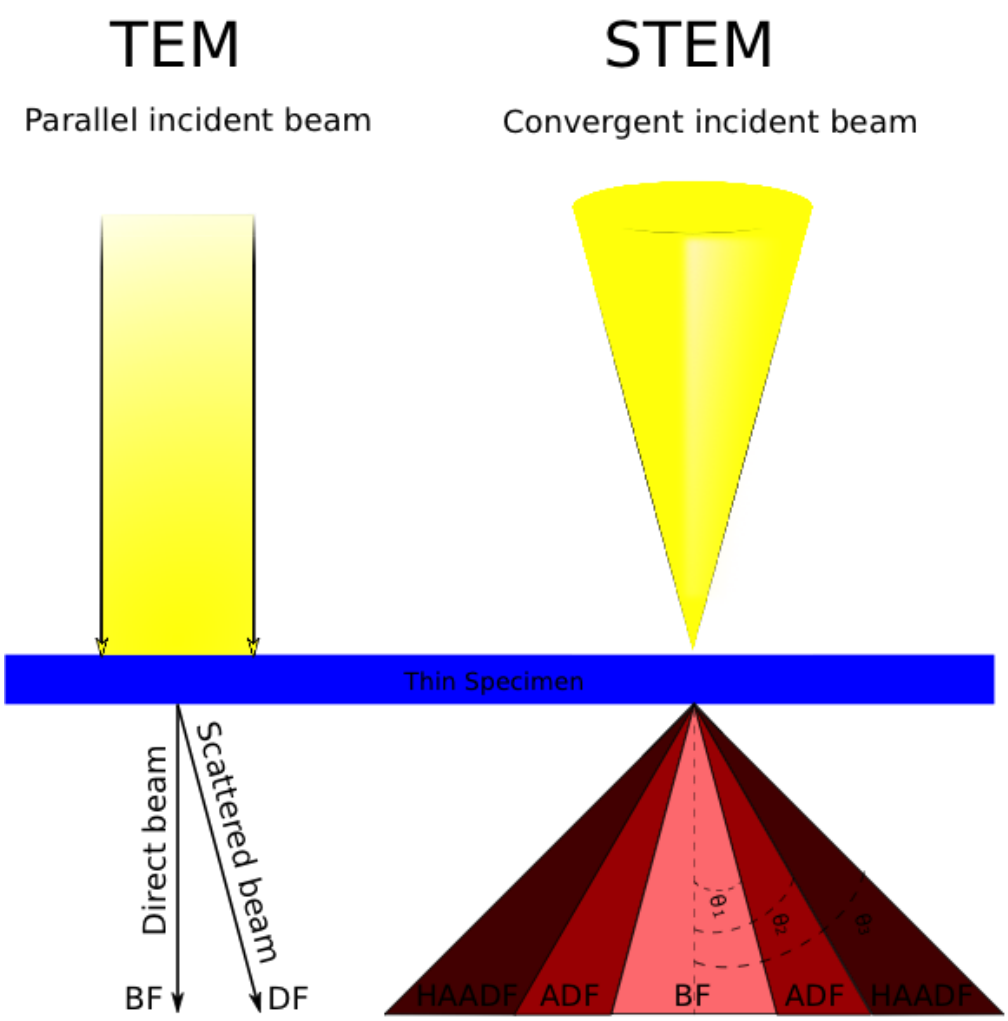


Figure 2.10: Illustration of conventional TEM and STEM mode. In TEM mode the incident electron beam is adjusted to be parallel prior to the sample interaction. In STEM mode the incident electron beam is adjusted in to a convergent beam that illuminates the sample. Common observation techniques in TEM mode include bright field and dark field imaging, composed by the direct and scattered beam, respectively.

### Selected Area Diffraction (SAD)

*Selected area diffraction (SAD)* is a common technique when performing diffraction experiments on a TEM. An aperture is inserted in the first image plane and adjusted to surround the *area of interest*. The selected area apertures are selectable, and their confinement area is typically in the range of 1-10μm. The result is diffraction information that originates from the aperture area, exclusively. This information is passed on to the projection system, which is adjusted to image the BFP on to the viewing screen. Each of the diffraction spots on the viewing screen corresponds to a unique plane in the *real* crystal lattice.

Resultantly, by measuring distances and angles, the complete real crystal structure can be obtained. It is, however, important to acknowledge that the distances between two spots in the DP are the reciprocal representation of the interplanary distances in real space. One such distance can be obtained by

$$d = \frac{\lambda L}{R} \tag{2.10}$$

, where $L$ is the camera length, λ the wavelength of the incoming electrons and $R$ is the measured distance in the diffraction spot pattern.

**Bright field –and Dark field imaging**

Bright field (BF) imaging in a TEM is when the direct beam is selected by an aperture to produce the image at the viewing screen. Direct beam is blocked by the objective aperture, letting only the diffracted electrons to pass, one obtain a dark field (DF) image. A dark field image give information about the change in the electron energy and, thus, information such as planar defects and defects can be obtained. The ray diagrams is shown in figure 2.11 below.

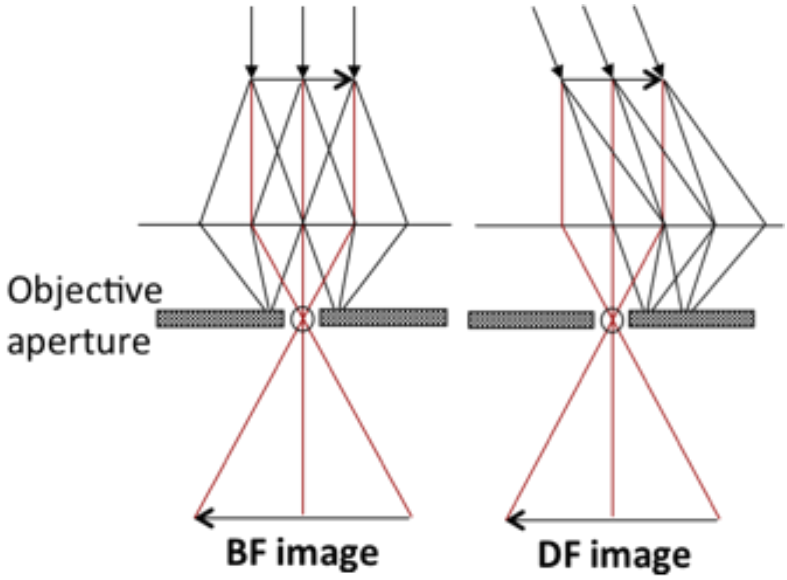


Figure 2.11: Illustration of how BF and DF-images is obtained by moving the objective aperture to block either the direct beam (DF) or the diffracted beams (BF).

## 2.6 Jet-polishing

The heart of the jet-polisher is sample chamber, in which two jets of a proper electrolyte is flushed onto the sample until a hole is made. The sample itself is locked in a sample holder that fits a 3mm disc of a thin metallic current conducting sample. The sample holder is electrically connected to a power source and makes the sample act as an anode. The polishing, i.e. the flushing, stops when a photodiode detects a hole. The sample is then quickly removed from the holder and rinsed.

There are a few parameters that will have to be adjusted to achieve a good TEM sample, these parameters are *voltage, current, flowrate, sensitivity and time*. These parameters can be adjusted by the control-unit. The control-unit is first of all the power source of the jet-polisher setup. It controls the voltage and current to the sample, through the holder, and to the pump that feeds the two jets. Furthermore, it also detects the signal from the photodiode when the hole is successfully made. It will then cut the power to both the sample-holder and to the jets.

Because this is an electrolytic reaction, the voltage and current is of great importance. The two parameters controls how fast the sample surface is etched and also how evenly it is done.

The flowrate is an important parameter of the jet-polisher and controls how much electrolyte that is flushed through the jets. It is important because it controls how fast the hole is made, and by experience it also contributes to the control of the size of the hole. This parameter should also be tested beforehand, to make sure that the two jets hit each other as close to the center of the sample as possible. If this is not done properly the sample could end up being bent, which will make the TEM analysis harder.

The sensitivity is the parameter that controls how much light that has to be detected by the photodiode in order to cut off the polishing process. This parameter will defiantly be of great importance to control the size of the hole as well as the general thinning of the surface.

Depending on the sample characteristics, the time parameter is often not the most important, but it could be useful. If the process is cut off by the photodiode

instantaneously after start, the sample could be porous. By setting a time for the polishing one can avoid the cut off by light, and rather polish the sample for å given time in order to gain a proper hole for TEM analysis. Avoiding the photodiode could also be a good idea if one wants to thin the sample further to accomplish thinner areas, although there is already a hole.

There is one last parameter that is not set by the control-unit and that is the temperature of the electrolyte. The temperature is important because the viscosity of the electrolyte changes with temperature. To obtain a stable, cold electrolyte, liquid nitrogen was circulated through the jet-polishers heat sink.

## 2.7 Focused Ion Beam

Another, more advanced, way to make a TEM sample is with a *focused ion beam* (FIB). A FIB is often equipped with a two-beam system. One beam is an electron beam and the other an ion beam. The electron beam makes the FIB act as an SEM. The reason for this is first of all to get a better image of what is being worked at. The other, main, reason is that the ions from the ion beam will damage the sample more because ions are a lot larger and heavier than electrons. For thin brittle samples the ion beam can destroy the sample completely just by viewing the same area for a long time. The way it works, briefly, is that a sample is mounted in to a sample chamber, similar to as in a normal SEM. The sample surface is then investigated to find an area that is of interest. The area of interest is marked out with a tool in the software, which normally is in the shape of a rectangle. This marked area is what will be the finished TEM-sample. In order to get the sample out of the matrix, the FIB utilizes the damaging effect of the ion beam. A much focused ion beam is set to irradiate along the edge of the marked area. This process is best compared to as very confined digging, because the ions damage the area that is in focus by the beam. When the digging is finished, the sample remains in the form of a wall fastened in the bottom and at one of the ends.

The last part of the FIB-process is to cut the lamella loose from the fastened ends and lift the sample off the surface and on to a TEM-sample grid. The great advantage with preparing samples with a FIB is that one can, with very high accuracy pick out a sample

from a larger piece of material. That is, one get a TEM sample from the exact region of highest interest.

# 3 Experimental Methods

## 3.1 Sample Production

A one-axis robotic welder, called a “tracer”, equipped with a cold metal transfer (CMT) device, was used to produce the first sample AA4020_S1. The parameters for material deposition are shown in table 3.1 and were equal for all deposited layers. The parameters were: Current: 85A, Voltage: 12.6V, wire feed rate: 5m/min and travel speed 7.6mm/s. 12 layers were deposited on an AA5754 substrate of thickness 5mm and 60mm width. The wire diameter was 1.2mm and the shielding gas was argon (Ar).

A three-axis robotic welder equipped with a (CMT) device was used to deposit 22 layers of each alloy in to the wall structures of the samples AA402_S2 and AA5083_S3. The wire diameter, substrate and shielding gas remained the same for both. The working distance (distance from the nozzle to the base material) was approximately 12mm. The welding parameters were the same for both samples, where the first layer was deposited with 177A and 15.3V and a wire feed rate of 8m/min. The travel speed was 6mm/s. The subsequent layers were deposited with 115A, 18V and a wire feed rate of 6.5m/min, which was reduced to 5m/min three layers. The travel speed was 6mm/s. The parameters are given in table 3.1.

The three samples AA4020_S1, AA4020_S2 and AA5083_S3 were deposited in the form of a wall with a single weld bead width.

**Table 3.1 – Deposition parameters:**

| Sample no: | Deposition layer no: | Current [A]: | Voltage [V]: | Wire feed rate [m/min]: | Travel speed [mm/s]: |
|---|---|---|---|---|---|
| AA4020_S1 | 1-12 | 85 | 12.6 | 5 | 7.6 |

| | | | | | |
|---|---|---|---|---|---|
| AA4020_S2 | First | 177 | 15.3 | 8 | 6 |
| AA5083_S3 | Subsequent | 115 | 18 | $6.5 \Rightarrow 5$ | 6 |

## 3.2 SEM Sample Preparation

When preparing samples for an SEM, one will have to consider what the goal of the microscopy is. That is, if simple imaging is the goal, one type of preparation could be necessary, whilst if the goal is to perform a chemical analysis of the sample, another type of preparation will be beneficial. However, in many cases a combination of methods is executed almost simultaneously. The latter, is of greatest interest in this project and thus, several methods of sample preparation have been tested to achieve the best results.

### 3.2.1 Cutting, Grinding and Polishing

In general, grinding and polishing is by itself not an advanced method of sample preparation, but it is of great importance. In many cases grinding and polishing is seen as preparatory work, but even the most advanced preparation methods and analysis could be completely ruined by bad grinding and polishing, which is why great care should be taken before finishing this step. However, in many cases, grinding and polishing is sufficient as a preparation method for the SEM. This is of course completely dependent on the nature of the sample and the method of analysis.

In the case of aluminium, one will have to acknowledge that it is very ductile, and thus hard to prepare perfectly by grinding and polishing. This is especially true, when the aluminium is not pure, but alloyed with elements that behave differently then the aluminium itself.

Depending on the surface of the sample, the grinding is usually started out with a coarse grit grinding paper. A common range of grit sizes is #80-#4000, where #80 is the coarsest. #80 to #220 is used to really remove material, usually to make the sample flatter or to remove sharp edges. The mid-range grit paper #320-#800 is used to even out the scratches of the coarser paper, but depending on the sample surface, they can also be used for the thinning of the sample is a similar manner as the coarser paper. At

last, the finer range, #1000-#4000, is used to further even out scratches from the previous grinding-step and to perform the final thinning with higher precision.

If the sample is being polished after the grinding step, one often stops at #1200 grit paper, because the finer grinding paper have got a particle roughness similar to the size of the diamond-particles that are used for polishing. It is important to mention that the grit-number is of two different standards, one European- and one US-standard. All references to grit sizes have been, and will be of the European standard.

**Table 3.2 – Relation between grit number and grain size:** [30]

| EU grit no. | #80 | #120 | #180 | #220 | #320 | #500 | #800 | #1000 | #1200 | #2000 | #4000 |
|---|---|---|---|---|---|---|---|---|---|---|---|
| US grit no. | #80 | #120 | #180 | #220 | #280 | #360 | #400 | #500 | #600 | #1000 | #1200 |
| Grain Size [μm] | 200 | 125 | 82 | 68 | 48 | 30 | 22 | 18 | 15 | 10 | 5 |

## 3.3 General Preparation of the AA4020 - and AA5083 Alloy samples

A few precautions were taken before preparing the two alloys. Firstly, the ductility of aluminium, because aluminium is quite soft, the scratches that is made by grinding could deform the internal structure rather deep in to the material. To avoid this, several steps of grinding were applied, each step to cancel out the deformation of the former. The grinding steps were controlled in a light microscope to observe the change in direction of the scratched made by the different grinding papers. By doing this observation, one can with relatively high accuracy be sure that the scratches made by the previous grinding step have been removed. The second precaution that was made was due to agglomeration of intermetallic particles of different sizes and compositions, during solidification. Such intermetallic particles can loosen from the surface during grinding, and later polishing, and scratch the surface in the same manner as a coarser grinding paper. Therefore, the amount of force that is put on to the sample was reduced during grinding.

The next step after grinding is polishing of the samples. Based on the experience of supervisors and literature, such as Struers' application notes [31], a certain order should be followed in order to get the best results. In general, this order contains which polishing cloths that should be used with which additive of certain particle sizes. The rule of thumb is to go from harder to softer cloths simultaneously as the particle size of the additive is decreased. The table below lists which cloths that have been used with which additive. The consumables used are all delivered by Struers.

**Table 3.3 – Preparation methods by polishing:**

| **AA4020 / AA5083** | | Cloth: | | | | | |
|---|---|---|---|---|---|---|---|
| Method: | Additive: | MD-Dur | MD-Mol | | MD-Nap | | MD-Chem |
| M1 | Diamond spray w. grain size: | 6μm | 3μm | 1μm | 1μm | 1/4μm | X |
| M2 | Diamond suspension w. grain size: | 6μm DP-susp. M | 3μm DP-susp. M | X | 1μm DP-susp. M | 1/4μm susp. P | OP-S |

The X's marks that the cloth have not been used with the suggested additive.

The additives that have been used in the preparation steps are as stated of two different kinds. The diamond spray is diamond grains suspended in an aerosol and the DP-suspension are diamonds suspended in a liquid consisting of mostly water (90-100%) and 1,3-Butandiol (5-10%) [32]. In addition to the choice of cloth and additive, there is the choice of lubricant. Struers provides several alternatives; the main difference is the water content and what the water is replaced with. Depending of the analysis method and material, the lubricant could be of great importance.

## 3.4 General Preparation of the AA4020 alloy

Grinding of the AA4020 alloy was performed with wet grinding paper of grit sizes in the following manner, #400, #800, #1000, #2000, #4000. The grinding process was lubricated and cooled with water and each step was controlled in a light microscope. Polishing was performed by the use of method M1 in table 3.2 above.

### 3.4.1 Chemical Etching of AA4020

Chemical etching of the AA4020 alloy was carried out by mixing of an acidic solution containing; 50mL $HNO_3$, 50mL HCl and 50mL water. The sample was lowered in to the solution, such that the surface was properly submerged. The sample was taken out of the solution after 1min and 34seconds and immediately rinsed in water to stop the etching process.

## 3.5 General Preparation of the AA5083 alloy

The bulk sample was cut in to smaller cross sectional pieces, approximately of 2cm thickness. One such piece was trimmed to remove unnecessary substrate material and grinded with a coarse grinding paper, #220, to get rid of deep scratches from the saw. The next steps of grinding was with the use of #400-, #800-, #1000-, #2000- and #4000-grit grinding paper, in the given order. Each step controlled in a light microscope.

For simple imaging and EDS analysis method M1 was performed with the use of Struers' green lubricant as the polishing step.

### 3.5.1 Electro-polishing

Several sample pieces have been electro-polished in order to reveal more of the microstructure in the SEM, simultaneously as the surface remains as flat as possible. That is, without too much topography produced by preferential etching. Another great benefit is that any oxide layer that might have been formed is easily removed by electro-polishing.

The equipment used was a Lectropol-5 from Struers. It consists of two parts. One, the largest, is the control unit, which controls the voltage, current, flowrate of the electrolyte and the time of polishing. The second part of the Lectropol-5 is the polishing unit. It has a chamber that holds the electrolyte container, and a heatsink that is lowered in to the electrolyte. The temperature is controlled by water flow through the heatsink. On top of the polishing unit there is a lever arm with a metal contact that constitutes the unit's positive lead. At last, there is the area that the polishing takes place. A jet flows the electrolyte towards the sample surface, which is limited by a selected mask to avoid spillage of electrolyte.


Figure 3.1: Image of the Struers Lectropol-5 electro-polisher. Adapted from [33]

The samples were prepared for electro-polishing by cutting the bulk sample in to thinner slices with an *Allied Techcut4* and a high concentration diamond cutting blade, selected by the recommendations from *Allied.* A slice was glued on to a stub and grinded with #800, #1000, #2000 and #4000 grit sanding paper.

A suitable mask was cut out by hand to expose as much of the sample surface as possible, the area was approximated to 3.1cm$^2$. The sample was taped to the mask, and mounted on to the polishing unit with the conductive lever in contact with the back of the sample. The parameters for the polishing were set on the control unit, and were as shown in table 3.4.

**Table 3.4 – Parameters for Electro-polishing:**

| Area: | Voltage: | Flowrate: | Time: | Temperature [°C]: |
|---|---|---|---|---|
| 2cm$^2$ | 39V | 10 | 20s | 22 |

Because of the lack of freedom of choice to set the exposure area, 2cm$^2$ were selected, as it was the closest to the approximated area. All the parameters were taken from Struers application notes on preparation of aluminium [31].

After the polishing stopped, the sample was quickly removed from the polisher and from the mask and thoroughly rinsed in water, and then isopropanol, to avoid etching and oxidation.

### 3.5.2 Electrochemical Etching

Electrochemical etching was performed on several samples to reveal more of the microstructure in the SEM, as well as improving the overview by VLM.

A solution of $HBF_4$ and water, called Barker's reagent, was made. The solute was pored in to a suitable conductive container, and connected to a power source via its negative lead. The power source was set to 15V. The sample was held with a clamp connected to the source through the positive lead. The etch begun as soon as the sample was in contact with the solute, and ended by lifting the sample away from the reagent.

The equipment used was predominantly Struers Lectropol-5 with its external power output. Another power source were also used, as the Lectropol has an upper voltage output of 15V. The second source could deliver up to 25V output.

Several different time spans was tested, in order to achieve the desired effect.

Figur 3.2: Image of the external etching equipment for the Lectropol-5.

### 3.5.3 SEM EBSD sample preparation

When preparing samples of the AA5083 alloy for EBSD analysis, the precautions that was mentioned in the general preparation section (3.2), becomes extra important. EBSD analysis is highly sensitive to deformation –and oxide layers. To deal with these challenges, parameters such as force, time and lubricant have been taken in to consideration. Several attempts on preparing a good sample for EBSD have been tried. On the first trial, preparation method M2 in table 3.2 was used with red lubricant from Struers. On the second trial preparation method M1 was used, because the OP-S treatment was thought of being too corrosive for the alloy, with green lubricant from Struers. Prior to the two first trials, the samples were grinded in a similar manner as those prepared for SEM/EDS analysis, that is, down to #4000 grit size. On the third trial the following method, M3, was used (see table 3.4 below). In addition the force was set to 10N, which was the lowest the polishing machine could provide. The number of repetitions (Rep.) denotes how many times the steps have been repeated, i.e. the number of times the grinding paper was swapped. A fourth preparation was performed and included method M3 and OP-S as the last step. [34]

**Table 3.5 – EBSD preparation method M3:**

| Step: | Rep. | Surface: | Lubricant: | Additive: | Time [min]: |
|---|---|---|---|---|---|
| 1 | 1 | #1200 w.gr. paper | Struers Blue | None | 10 |
| 2 | 5 | #1200 w.gr. paper | Struers Blue | none | 2 |
| 3 | 4 | #2000 w.gr. paper | Struers Blue | none | 2 |
| 4 | 3 | #4000 w.gr. paper | Struers Blue | none | 2 |
| 5 | 1 | Struers Md-Dur | Struers Blue | 6μm DP susp. M | 45 |
| 6 | 1 | Struers Md-Mol | Struers Blue | 3μm DP susp. M | 30 |
| 7 | 1 | Struers Md-Nap | Struers Blue | 1μm DP susp. M | 45 |
| 8 | 1 | Struers Md-Nap | Struers Blue | 1/4μm DP susp. P | 15 |

Struers blue lubricant was chosen because it does not contain water, which helps avoiding an oxide layer.

## 3.6 TEM sample preparation

In order to investigate the materials microstructure with a TEM, certain limitations will have to be met. The most important is the thickness of the sample; because it will have to be thin enough for electrons to be able to transmit the sample, this limit is about 100nm or less. The second limitation is the diameter of the sample, which is set by the specimen holder in the TEM. This diameter is typically 3mm.

Several different techniques of sample preparation exist, all depending on the samples characteristics. One method is jet-polishing, which is commonly used for different metals and alloys, and especially aluminium. Most of the samples made in this project are made by jet-polishing.

### 3.6.1 TEM sample preparation by jet-polishing

Preparing aluminium TEM-samples by jet polishing have got a few benefits. First of all, when the setup is ready, preparing samples goes fast. The making of 20-30 samples in an afternoon is absolutely possible. Another great benefit is that the samples are self-supported in the TEM holder. The jet-polishers sample holder requires that there is a good electric contact between the holder and the sample, and to make the etching process even it is connected all the way around the sample. The result of is this is that the part that is clamped in between the holder-pieces is not etched, which is great because this, un-etched, part is thick enough to be self-supported in the TEM sample holder. A self-supported sample means that mounting the sample is done more easily, another benefit is that the sample is self is tougher and will withstand rougher handling.

As mentioned, a vast majority of the TEM samples made in this project was made by jet-polishing. The reason for this was that it was easy to find background material on procedures, as well as it being the recommended preparation method. The following procedure was performed.

An *Allied Techcut4* with a high concentration diamond cutting blade was used to cut thin slices of the cross section of the sample wall. The cutting process was lubricated with lubricant from *Allied: 60-20110*. After cutting, the slices were cut in to three pieces and glued on to stubs, to make the grinding easier. The glue used was *Crystal Bond 509.* The pieces were grinded with grinding paper in the following grit-order #500, #1000 and #1200. The grinding was lubricated with water. Based on the article by (Necip Ünlü, 2007), the optimum thickness of the sample before jet-polishing was ≈0.15mm. Because the grinding was performed manually, the possibility of having an unlevel sample after grinding is relatively high. The following table lists the measured thicknesses of the different sample pieces after grinding.

**Table 3.6 – Measured thicknesses after grinding**

| Piece of slice: | Top: | Middle: | Bottom: |
|---|---|---|---|
| Upperm. measure: | 0.11 mm | 0.20 mm | 0.18 mm |
| Middle measure: | 0.12 mm | (Bent[2]) | 0.17 mm |
| Lowerm. measure: | 0.15 mm | 0.25 mm | (Substrate) |

After grinding, the pieces were shaped in to 3mm discs by punching.

The choice of electrolyte was based on experience from supervisors and the article from Necip Ünlü [35], which consists of 30%$HNO_3$ in methanol. The temperature was controlled by liquid nitrogen circulating through a heatsink, and held at several different temperatures to test the effect on the sample. With temperatures ranging from 243-263K, a seemingly optimum was found to be ≈248K ± 2K. The table below reveals the rest of the parameters used for sample preparation. The parameters are based on trial and error with numerous samples. That is, the parameters in table 3.7 are those who gave the best result with the available equipment.

[2] Because of a bump in this area, no accurate reading could be performed.

**Table 3.7 – Preferential parameters of the Tenupol-2 jet-polisher for TEM sample preparation of the 5083 Al-alloy**

| Temperature [°C] | Voltage [V] | Current [A] | Sensitivity: | Flowrate: |
|---|---|---|---|---|
| -20 ± 2 | 30 | 5 | 3.5 | 7.5 |

When the polishing was finished, the samples were quickly taken out of the jet-polisher holder and rinsed twenty times in three different beakers containing isopropanol, to stop any leftovers of the electrolyte to continue the etching. The finished samples were left for drying.

### 3.6.2 TEM sample preparation by Focused Ion Beam (FIB)

Based on observations from an SEM and literature, regions of high interest were found to be across grain boundaries of the aluminium or across arms of different dendrites. Because aluminium is ductile, such boundaries are difficult to observe on a polished sample. However, on a chemically treated sample these boundaries become a lot more visible and selected areas easier to extract.

An electro-polished sample-piece was inserted in to the FIB. Several visible dendritic arm crossings were observed. An area of higher interest, an arm-crossing containing intermetallic particles, was selected for the extraction of a sample. The selected area was marked out by the software, dug out by the ion beam, and carefully fastened to a TEM grid.

## 3.8 Mechanical Testing

The mechanical tests included tensile testing, Vickers hardness tests and porosity measurements on all the sample-walls that have been examined in this thesis. All the mechanical tests have been performed by SINTEF. The Porosity measurements were done by post image processing with use of *imageJ*. The tensile test samples were extracted in both the horizontal –and vertical direction on the wall. And the Vickers hardness tests performed on a Zwick-Roell ZHV 30A hardness tester. The initial tensile test properties are shown in table 3.8 below.

**Table 3.8 – Initial mechanical properties of the wrought alloys of AA4020 and AA5083:**

| **Alloy:** | **Yield strength $R_{p0.2}$ [MPa]:** | **Tensile strength $R_m$ [MPa]:** | **A100 [%]:** | **Test temperature [°C]:** |
|---|---|---|---|---|
| **AA4020:** | ≥50 | ≥120 | ≥25 | 20 |
| **AA5083:** | ≥125 | ≥300 | ≥25 | 20 |

## 3.9 Homogenisation of the AA5083 alloy

A heat-treatment was performed on a sample piece of the AA5083 alloy. This was done in order to homogenise any irregularities with regards to the microstructure and to improve hardness and tensile properties. The homogenisation temperature was thermodynamically calculated by SINTEF with the use of JMatPro software. The sample (AA5083_S3) was heat treated for 4 hours and 8 minutes at 400°C.

### 3.10 Analytical Scanning Electron Microscopy

Close to all of the samples have been examined with the use of a Hitatchi tabletop TM3000 SEM with a tungsten cartridge filament and a BSE- and EDS-detector, the only exception was the FIB sample. The polished, etched and electro-polished samples was fastened to an aluminium stub with carbon tape. The TEM samples that were examined were placed in a holder designed for the task. The SEM was operated with 15keV acceleration voltage.

### 3.11 Analytical Transmission Electron Microscopy

The TEM analysis was performed on a JEOL *JEM-2100F*, operated at 200keV acceleration voltage. The microscope has an Schottky FEG and along with an ultra-high resolution pole piece, a point resolution of 1.9Å is achievable. The energy dispersive spectrometry (EDS) spectrums were acquired with an Oxford Instruments *X-Max$^N$ 80T* with a silicon drift detector (SDD). All of the experiments were performed using a *JEOL EM-31640* double tilt holder, for a large range of tilting angles, and an Orius CCD camera collected the images. The STEM experiments were executed with the use of a *JEOL EM-24541SI0D* observation device and a *JEOL EM-271021AU* image acquisition unit. Post image processing was performed with Gatan's *Digital Micrograph* and post processing of EDS spectrums and collected STEM maps with the use of Oxford Instruments' *AZTec*.

# 4 Results

The final walls were deposited as described in section 3.1, is shown in figure 4.2. The first wall (AA4020_S1), were produced with relatively high travel speed, but low current, voltage and wire feed, compared to the two other walls (AA4020_S2 and AA5083_S3) is shown in figure 4.2a). The resulting walls of AA4020_S2 and AA5083_S3 produced with the same deposition parameters (table 3.1), are shown in figure 4.1b) and c), respectively. In the following, the results of mechanical and microstructural investigations will be presented for each sample, including the results of the homogenization of the wall of AA5083_S3 (AA5083_S4).

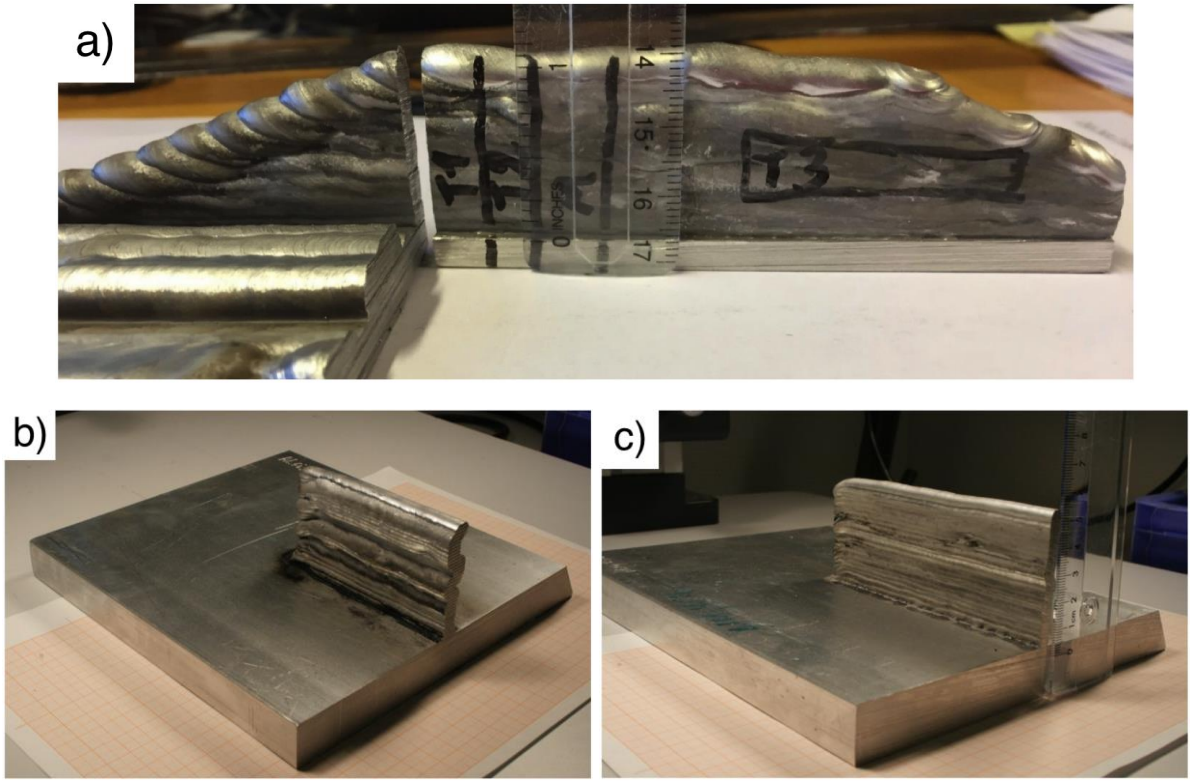


Figure 4.1: Images of the three deposited wall structures. a) the first AA4020 wall, b) the second AA4020 wall and c) the first AA5083 wall.

### 4.1 Sample AA4020_S1

The wall AA4020_S1 was produced with 12 deposited layers. The measured height of the wall is H≈2.7cm and the approximate width is W ≈0.7cm. However, the width varies from ≈0.5cm to ≈0.9cm, because of the bumps along the edges (figure 4.2). From figure 4.2b) and c) the twelve deposited layers can be distinguished by matching the surface bumps to the strong contrast features. In general, the observed dark- and bright regions in figure 4.2c) coincide with the twelve deposited layers in an pair-wise manner. The bright regions are named heat affected zones (HAZ) and are regions where sufficient amount of heat from the subsequent layer has altered the material properties and microstructure. Control over the HAZ is a very important factor to welding, because many of the initial material properties are changed.

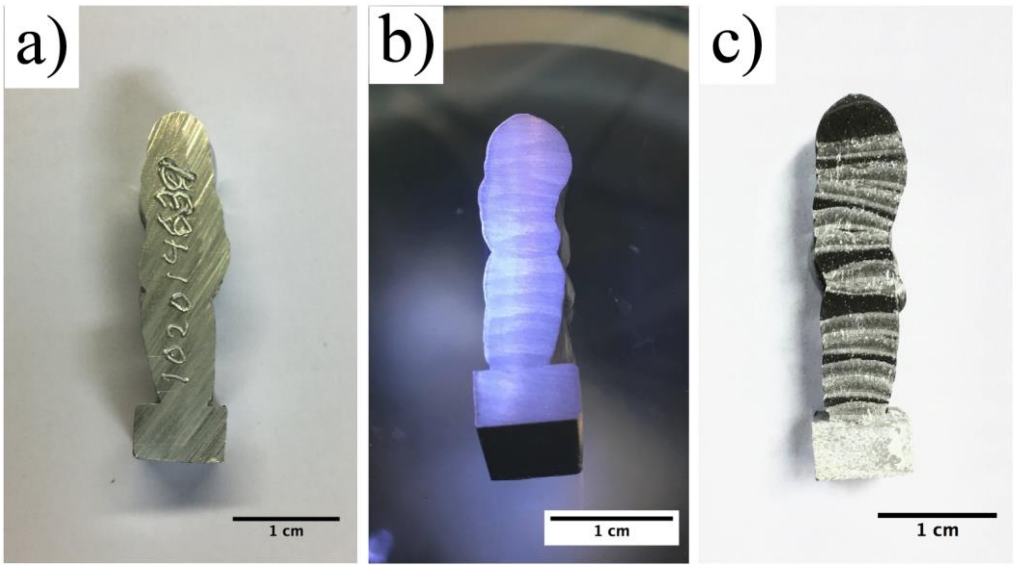


Figure 4.2: AA4020 cross section images of, a) untreated sample, b) polished sample showing contrast changes in reflection with light and c) etched sample, further enhancing the contrast changes that were observed in b).

### 4.1.1 Mechanical properties of AA4020_S1

#### Tensile tests

The tensile tests were performed as described in section 3.8 and the result is reproduced below. The three samples were extracted in the areas indicated in figure 4.1. Here, a marker pen has been used to label the samples T1, T2 and T3, which corresponds to the sample names S1_V1, S1_V2 and S1_H1 in this presentation. Figure 4.3 shows nominal stress-strain curves for the three tensile samples that were tested. The curve shows the typical behaviour of a relatively ductile material. The vertical tensile test samples, named S1_V1 and S1_V2, are represented by the red- and green curve, respectively. The result of the horizontal test sample, named S1_H1, is represented by the blue curve. The two vertical sample tests have a measured maximum tensile strength of ≈161MPa (red) and ≈153Mpa (green) for the test samples S1_V1 and S1_V2, respectively. The horizontal test sample has a slightly higher maximum value of ≈166MPa. The elongation of the three samples differs only slightly. The two vertical samples have a measured maximum strain%-value of ≈16.6% and ≈15.6% for the S1_V1- (red) and S2_V2 (green) samples, respectively. The horizontal tensile sample, S1_H1 (blue), had a maximum strain%-value of ≈14.2%. The calculated yield strength values were 61MPa (S1_V1), 54MPa (S1_V2) and 61MPa (S1_H1). In general there are only minor differences between the samples, which is a sign of good fusion between the weld beads. The measured values are listed in table 4.1 below.

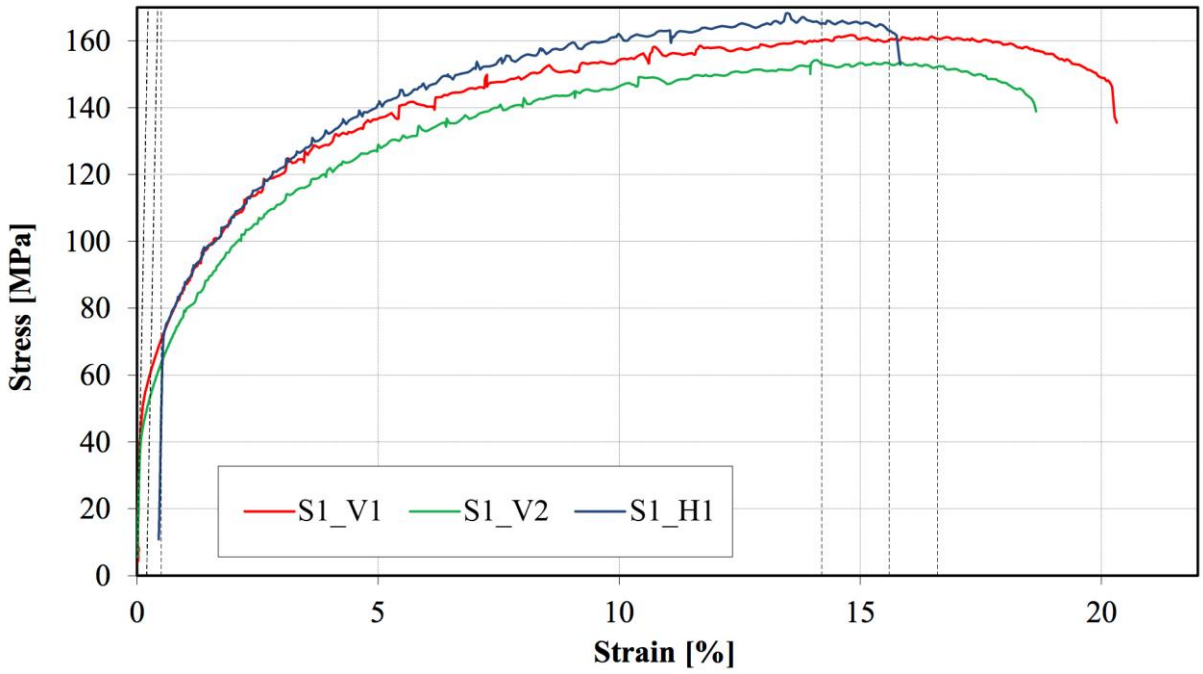


Figure 4.3: Tensile stress-strain curves of the first AA4020 sample (S1). S1_V1 (red) and S1_V2 (green) are extracted from the vertical direction and S1_H1 (blue) is from the horizontal direction.

**Table 4.1 – Tensile test results of sample AA4020_S1:**

| **Specimen ID:** | **Diameter [mm]:** | **Yield strength $R_{p0.2}$ [MPa]:** | **Tensile strength $R_m$ [MPa]:** | **Strain at max. load $A_{gt}$* [%]:** |
|---|---|---|---|---|
| S1_V1 | 2.80 | 61 | 161 | 16.6 |
| S1_V2 | 2.78 | 54 | 153 | 15.6 |
| S1_H1 | 2.77 | 61 | 166 | 14.2 |

**$A_{gt}$**: percentage of total strain at maximum force.

**Hardness Tests**

The hardness tests were performed with the equipment described in section 3.8. The VLM image below (figure 4.4) shows the cross section of the sample piece, where the individual weld beads can be distinguished. The indentations are visible as the small black squares with corresponding measured hardness (HV). A total of 26 indentations were made. Two of these indentations were performed on the uppermost layer, named the "cap layer". The measured values in this area were 49- and 47HV, which are the highest (i.e. hardest) values of them all. Another deviating area is at the interface between two weld beads. In this area one indentation were made, and it yielded 41HV, which is slightly below the average of ≈43.5HV. The rest (23) of the indentations were performed in the primary deposited material (DM) and in the reheated DM. These two areas corresponds to the dark- and bright contrast areas in figure 4.2c) and figure 4.4a, respectively. The average value of the nine indentations performed in the primary DM is ≈33.7HV. The maximum value is 47HV and the minimum is 17HV. In the reheated DM the average value of the twelve indentations is ≈41.75HV and the corresponding maximum and minimum, 46 and 28, respectively. The overall hardness decreases in the build direction (i.e towards the cap layer) with ≈-0.23HV per indentation. However, The hardness of the primary DM increases with ≈4.1HV per primary indentation in the build direction, whilst the reheated DM decreases by ≈-0.54HV similarly. The linear regressions made for these observations can be seen in appendix as figure A.2, A.3 and A.4, the measured hardness values are presented in table 4.2 below.

The results is presented in table 4.2 below are also indicated in figure 4.4a). The red squares in the image describe the positions of the VLM images. These images show the heat-affected zones (HAZ) at three different positions on the sample. The sample was etched with Keller's etchant prior to the image acquisition. The images show that the main phae is $\alpha$-aluminium with a eutectic structure. Figure 4.4a) show the uppermost HAZ i.e. the boundary between the last layer (cap layer) and the second to last layer. Figure 4.4b) and c) show the lowermost HAZ that occur between the substrate and the first layer, which is easily observed by the different aluminium structure.

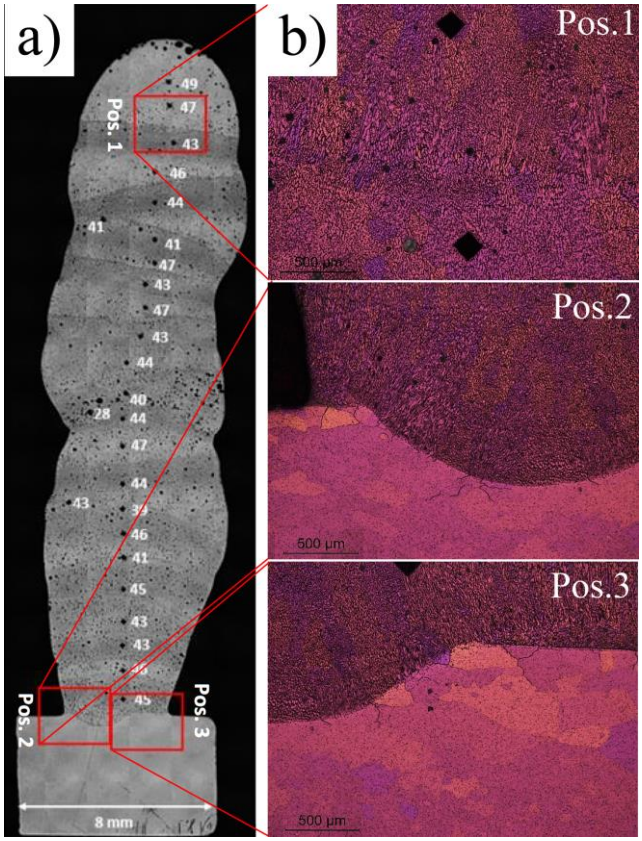


Figure 4.4: Cross section image of the AA4020 sample 1 (S1) with notation of the measured Vickers hardness (HV) at the respective indentation. The red squares indicate the positions of which the three VLM images in b) (see markings), that reveal an α-aluminium main phase with a eutectic structure.

**Table 4.2 – Hardness test results (HV) of the deposited AA4020 S1 sample.**

| **Indentation no:** | **Hardness [HV]:** | **Comment:** | **Indentation no:** | **Hardness [HV]:** | **Comment:** |
|---|---|---|---|---|---|
| **1** | 49 | Cap layer | **14** | 47 | Primary DM |
| **2** | 47 | Cap layer | **15** | 44 | Reheated DM |
| **3** | 43 | Reheated DM | **16** | 39 | Primary DM |
| **4** | 46 | Primary DM | **17** | 46 | Reheated DM |
| **5** | 44 | Reheated DM | **18** | 41 | Interface |
| **6** | 41 | Reheated DM | **19** | 45 | Reheated DM |
| **7** | 47 | Primary DM | **20** | 43 | Primary DM |
| **8** | 43 | Reheated DM | **21** | 43 | Reheated DM |
| **9** | 47 | Primary DM | **22** | 46 | Primary DM |
| **10** | 43 | Reheated DM | **23** | 45 | Primary DM |
| **11** | 44 | Primary DM | **24** | 41 | Reheated DM |
| **12** | 40 | Reheated DM | **25** | 28 | Reheated DM |
| **13** | 44 | Reheated DM | **26** | 43 | Reheated DM |

### 4.1.2 Microstructure of the AA4020 sample S1

The microstructure of the specimen has been investigated at various positions, from the top of the specimen, with special focus on the last two weld beads, to the bottom of the specimen, with focus on the wall-to-substrate interface. In the following, the features at the different positions will be presented.

#### Wall-substrate interface

At the lowermost boundary between the substrate and the first deposited layer, seen in figure 4.5, an SEM-EDS acquisition showed that the deposited material penetrated approximately ≈550µm into the substrate. The penetration is observed by the EDS maps in figure 4.5, where the brightest yellow represents the deposited silicon rich AA4020 alloy into the less yellow, silicon poor AA5754 substrate alloy. No significant pore formation at the interface is observed. However, there is an increased concentration of a silicon at the edge of the deposited area close to the interface, which could be an effect caused by rapid cooling of the weld when the molten material hits the cold base material.

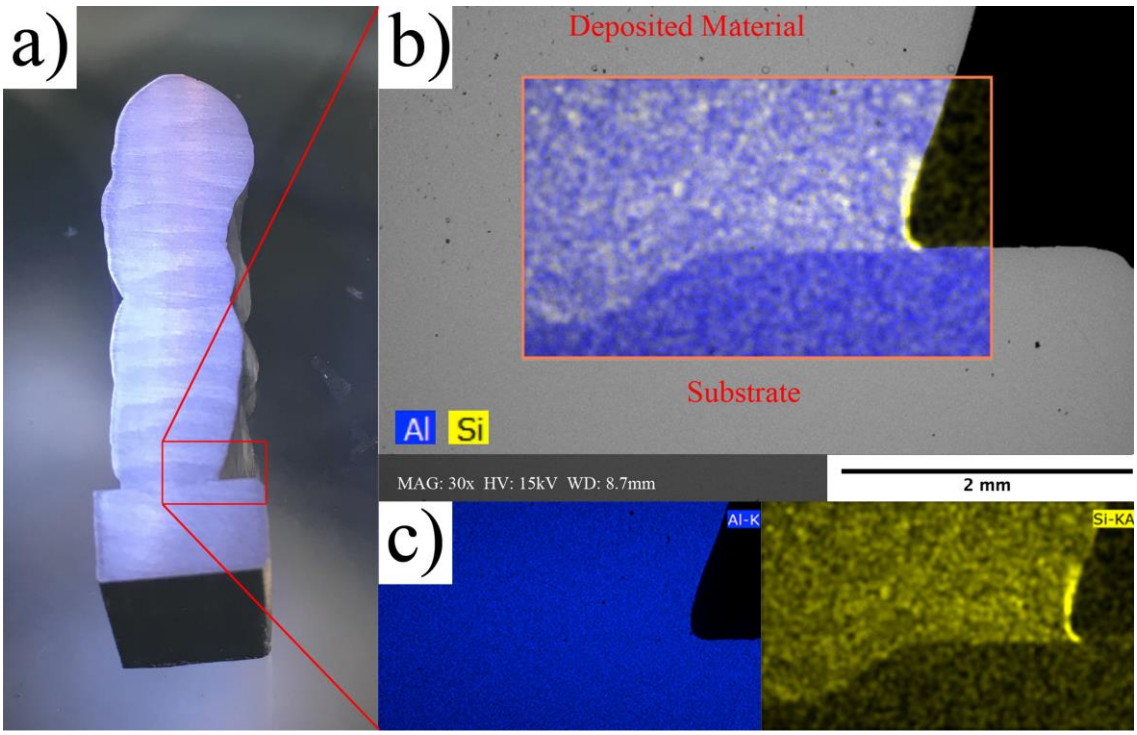


Figure 4.5: a) polished sample with indication of the area that is analysed, b) layered image of Aluminium and Silicon, c) Elemental aluminium- and silicon map. The images reveal how well the deposited material has fused in to the substrate. The fusion is determined by the silicon rich AA4020 weld-wire and how it penetrates into the silicon-poor AA5754 substrate.

**Interfaces**

Apart from the wall-substrate interface, two types of interfaces are commonly encountered and investigated in this sample. One is the interface between the weld beads, e.g. figure 4.6. The second is the interface between the deposited material and the reheated material, i.e the HAZ.

The microstructure at the interface between two weld beads mid-way up the wall is shown in figure 4.6, where the bump is clearly seen in both the optical- and electron BSE image. From the BSE image a high concentration of intermetallic particles is observed and EDS elemental mapping revealed that these particles consist of mainly manganese and silicon. The silicon is not observed in the BSE image due to the very similar atomic numbers of aluminium ($Z_{Al}$=13) and silicon ($Z_{Si}$=14). The Si and the Si-and-Mn particles are found to be connected to each other.

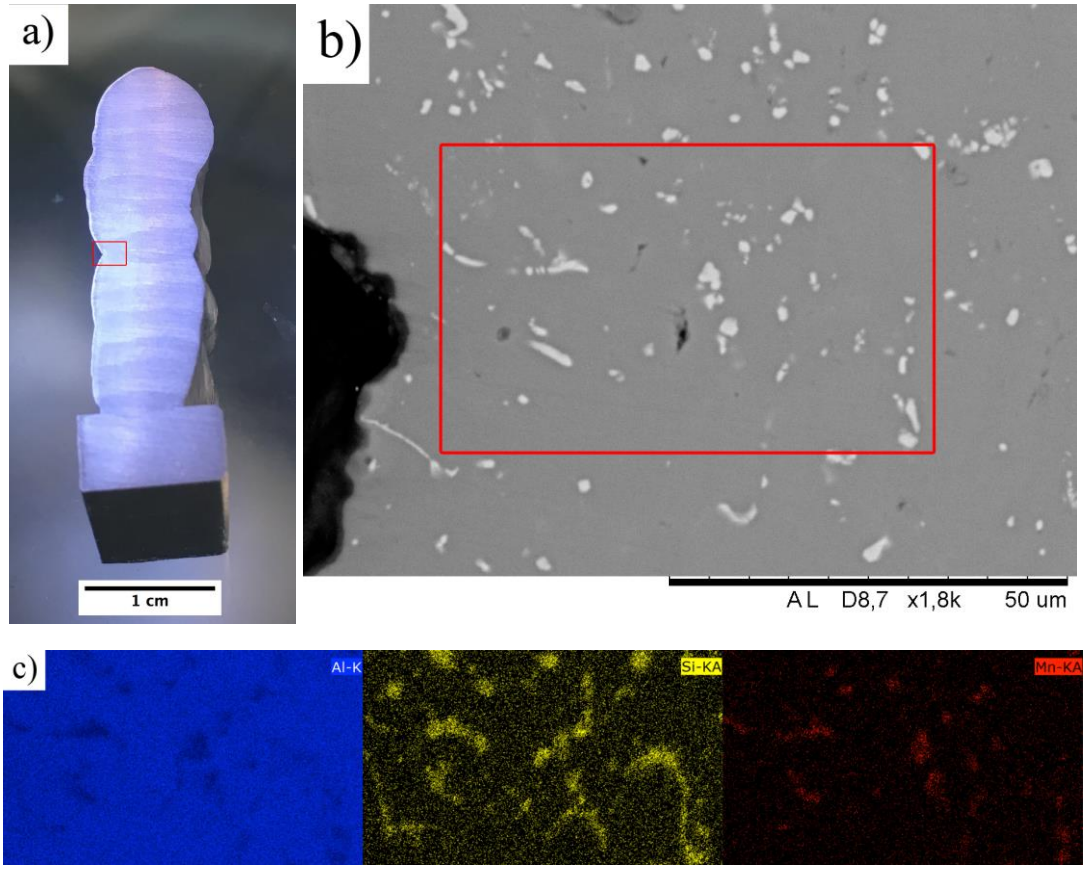


Figure 4.6: a) The wall structure with an indication (red square) of the analysed area. b) BSE image of the interface. The area shows a lot of precipitation. EDS analysis were performed within the red square. c) Individual elemental maps of the detected elements, where the blue map is aluminium, the yellow is silicon and the red is manganese.

A TEM analysis by both diffraction and EDS were performed on the Mn and Si rich particles. An example is shown in figure 4.7, where a particle with a diameter of ≈300nm is imaged. The collected EDS data presented in figure 4.8 (spectrum) and table 4.3 (quantification) showed that the acquisition area had a chemical composition of 74.56at% Al, 8.31at% Si, 6.30at% Mn and 10.83at% Fe. Based on the composition the particle is consistent with the Al(Mn,Fe)Si-phase. This phase is cubic with the space group Pm3 and lattice parameter a≈12.4Å. This is also consistent with a d-value of 8.8Å (110) as found for the particle in 4.7. [36]

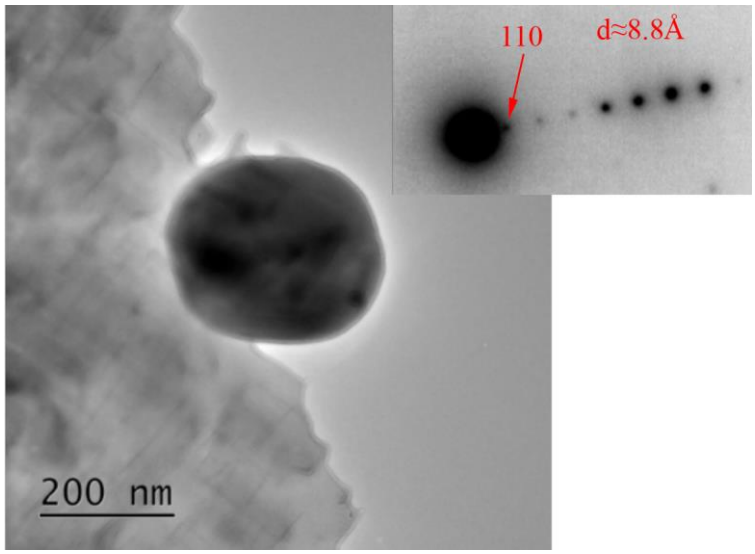


Figure 4.7: A BF image of a particle. The particle is very likely a Al(Mn,Fe)Si phase, based on diffraction (inset image) and EDS. It is approximately 300nm in diameter.

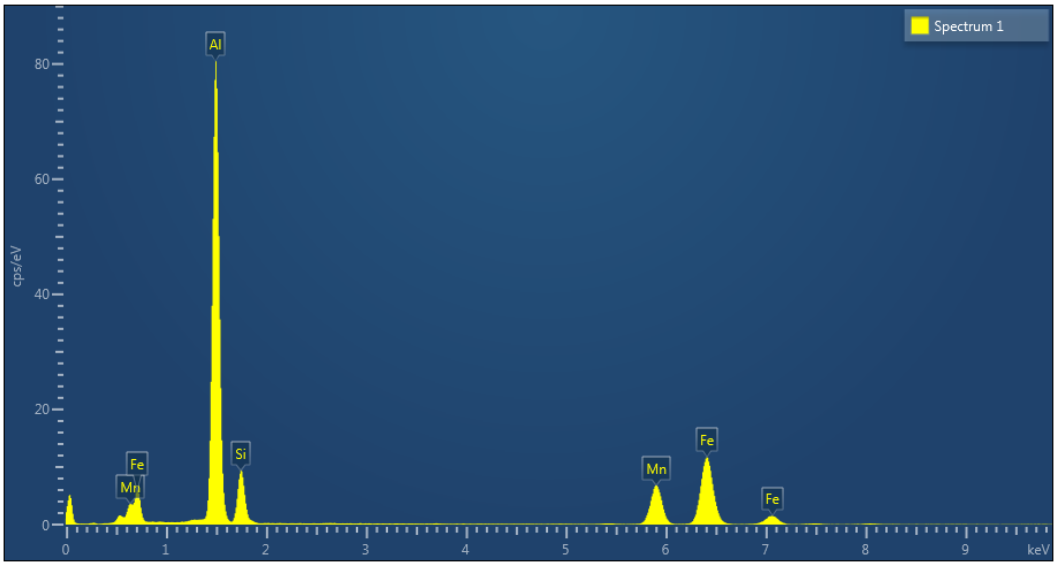


Figure 4.8: EDS spectrum of the particle in figure 4.7. The particle consists of aluminium, silicon, manganese and iron.

**Table 4.3 – Quantification of the particle in figure 4.7**

| Element: | Wt%: | Wt% sigma: | At% |
|---|---|---|---|
| Al | 63 | 0.11 | 75 |
| Si | 7 | 0.06 | 8 |
| Mn | 11 | 0.07 | 6 |
| Fe | 19 | 0.09 | 11 |

An analysis was performed on an interface between the two last weld beads. The interface was found between the cap layer (the last deposited and uppermost layer) and the HAZ. Below this interface is a weld bead interface, which observed as an interface between a deposited layer and the subsequent HAZ. The cap layer is a representation of the least heat-affected layer, and reveal how the deposited material would have been if only one weld bead were deposited.

Etching the sample made the surface attain a topography change, when crossing the observed contrast areas as seen in figure 4.9 below. The figures below show the etched sample with an indication of where the two other images are acquired. The two images display, a) a compositional contrast, and b) a topography view of the selected area. The compositional-contrast image does not show any significant change in contrast, which is a sign of either a single main phase of different height, or different phases with elements of very similar atomic number. The latter effect was observed in the results presented in figure 4.6. The topographical image in c) clarifies the other cause, which is a topography change when such a contrast-changing interface is crossed. Because one weld bead consists of the pair of one dark- and one grey layer, the last weld bead interface is situated right below the grey area (in figure a), in other words at the boundary where the topography is raised after being depressed. This observation makes it better to recognize the weld bead interfaces, when the common analytical mode, i.e. compositional-contrast, fails to do so.

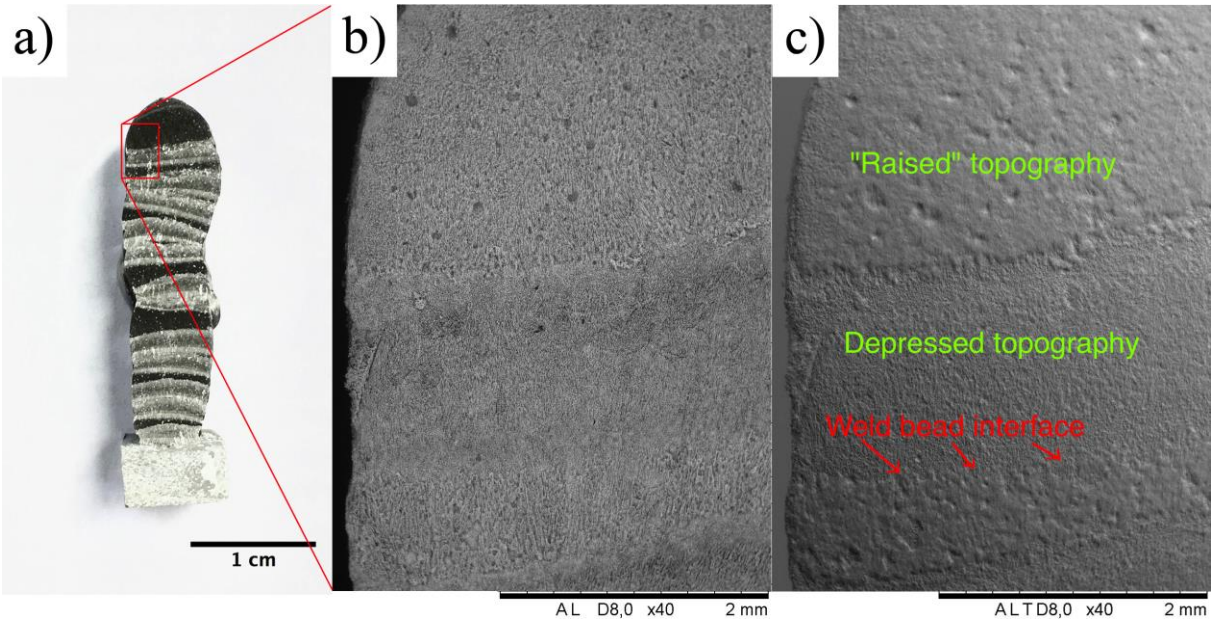


Figure 4.9: Images of the topography change when the contrast areas in a) is crossed. The compositional-contrast image in b) exhibits minor changes, due to the neighbouring atomic numbers of aluminium and silicon. The image in c) show the resultant topography after chemical etching

Analysis of the uppermost interface between the cap layer and the HAZ revealed a similar topography change. Figure 4.10 below shows what both the contrast changes in figure 4.2, and the topography in figure 4.9, were due to. The EDS maps reveal that the observed changes are indirectly caused by an elemental difference. The dark area is richer in silicon than the bright area. Again; this explains the minor compositional contrast in figure 4.9 above. Another observation of figure 4.10 is oxygen, which is connected to the silicon rather than the aluminium. The two circles in the image indicate the areas of which two quantitative spot analysis were performed. These results are presented in table 4.4 and 4.5.

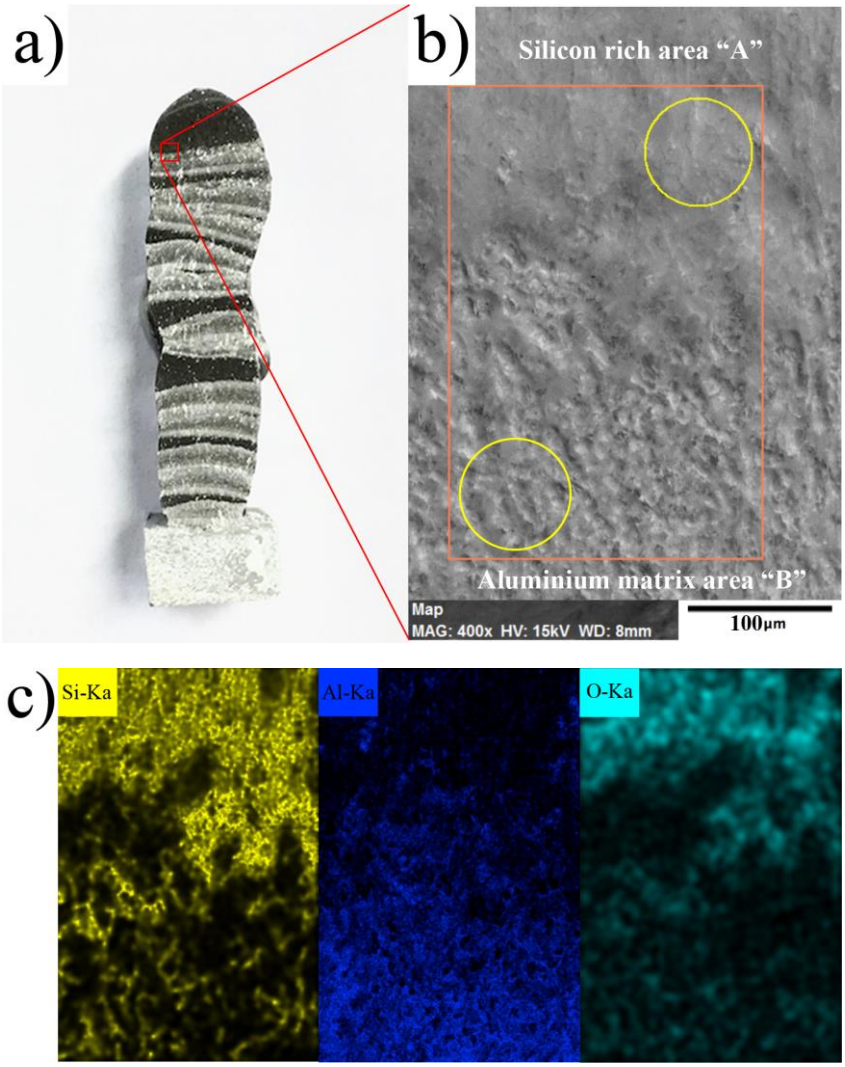


Figure 4.10: a) approximate area of acquisition of b). b) Boundary between dark –and bright area (area A and B) with an indicated area of EDS mapping (orange square) and spot analysis (yellow circles). c) Elemental maps of the area within the orange square in b). The images show that both the topography and contrast changes is mainly caused by a change in silicon content. The silicon also seem to have been oxidised by the elemental map of oxygen.

From figure 4.10 there is an apparent change in silicon –and aluminium content when crossing this boundary. Because the maps in figure 4.10c are not quantitative, two spot areas were selected to reveal this effect in numbers. The tables below show the result of the quantification at the two areas. The quantification of spot area A yields higher silicon content (48at%) than aluminium (29at%) as well as oxygen (23at%). However the oxidation is caused by the preparation method. The resulting quantification of the spot in area B yielded, silicon (24at%), aluminium (71at%) and oxygen (5at%). The results of the quantification show that the silicon content decreases dramatically in the crossing from the dark cap layer and into the bright region below.

The relatively low aluminium content in the upper cap layer suggests that the silicon has been enriched in this region.

**Table 4.4: Quantification of the dark area in figure 4.10a)**

| Element: | Normalised C. [wt%]: | Atomic C. [at%]: | Error [%]: |
|---|---|---|---|
| Silicon: | 54 | 48 | 3 |
| Aluminium: | 31 | 29 | 2 |
| Oxygen: | 15 | 23 | 3 |

**Table 4.5: Quantification of the bright area in figure 4.10b)**

| Element: | Normalised C. [wt%]: | Atomic C. [at%]: | Error [%]: |
|---|---|---|---|
| Silicon: | 25 | 24 | 1 |
| Aluminium: | 72 | 71 | 5 |
| Oxygen: | 3 | 5 | 1 |

Figure 4.11 shows a magnified image of the interface between the first and second weld bead as illustrated in a). On the etched surface, where the Al-matrix has been removed, dendrites like Si-structure can be seen. Figure 4.11, shows the boundary along with a layered image made out of the BSE together with the elemental maps of silicon and aluminium. Figure 4.11 reveal that the silicon changes that were observed in figure 4.10 is in fact high purity silicon dendrites. This is further proved by TEM analysis, which is presented later. The elemental EDS maps of the area (figure 4.11d) also show that the detected oxygen follows the silicon dendrites, similar to the observation in figure 4.10c this is an effect of etching. An interesting observation of figure 4.11b) is how the silicon dendrites have grown into the aluminium matrix.

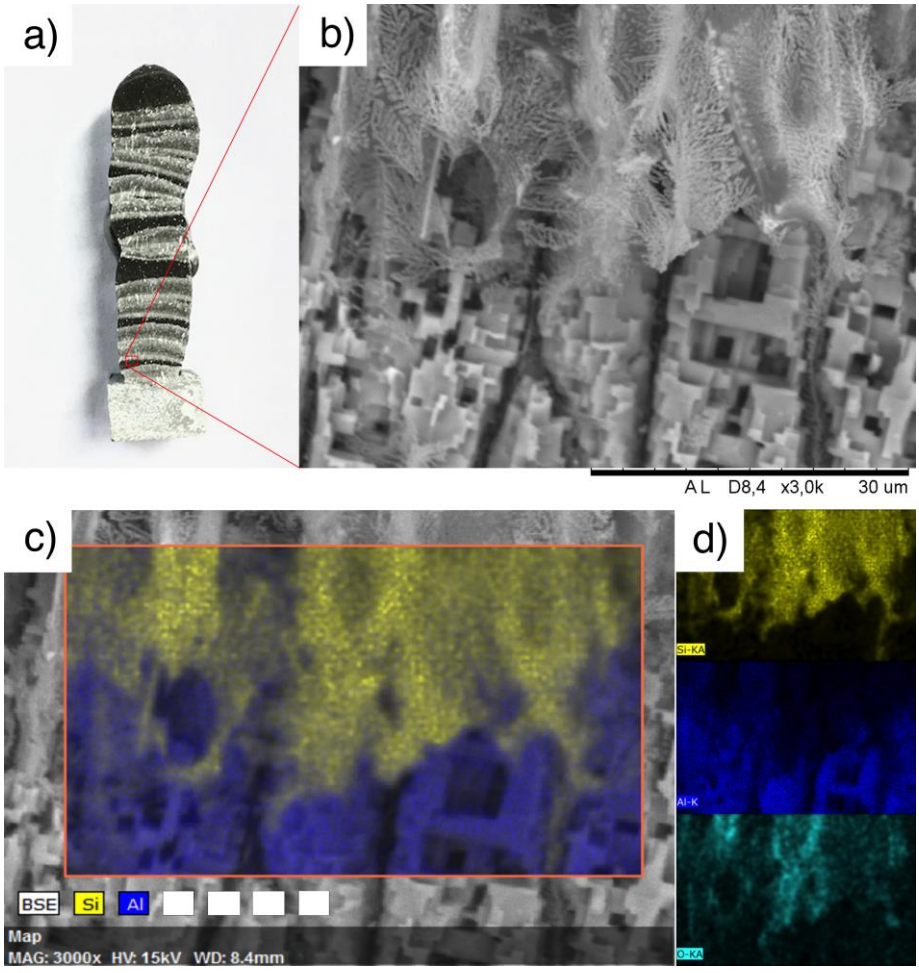


Figure 4.11: a) image of the etched sample with indication of the analysed area. b) BSE image of the analysed area, revealing a distinct interface with a complex dendritc network. c) Layered image of BSE, aluminium and silicon, displaying the interface of the aluminium matrix and silicon dendrites. c) Elemental EDS maps of silicon, aluminium and oxygen.

TEM samples were prepared in order to analyse the microstructure closer, especially the observed silicon dendrites. The TEM samples were prepared as described in section 3.6.1. Before the TEM analysis was performed, the samples were examined with an SEM to ease the task of finding areas of higher interest. An SEM image of a sample is shown in figure 4.12 below, and clearly, there is a large hole, more in the shape of a “bay”, at the edge of the sample. Along the edge of this “bay” is where the sample is sufficiently thin for electron transmission. The etching caused by the electrolyte also has brought silicon dendrites to the surface, as can be seen in the magnified image of the area marked in figure 4.13a). The dotted line marks the boundary of where the silicon dendrites starts to stick out from the surface

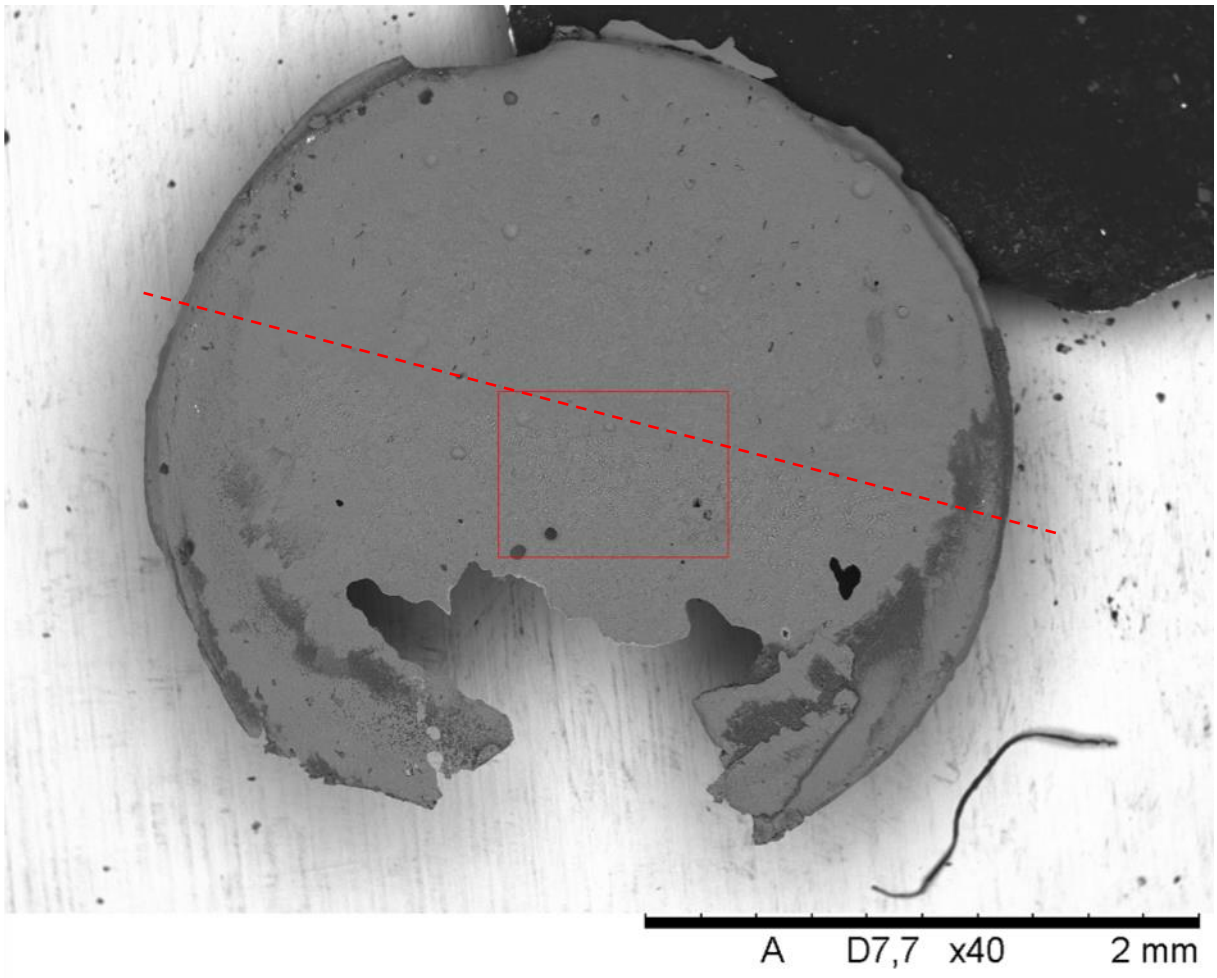


Figure 4.12: TEM sample of the wall AA4020_S1. The dashed line indicates the boundary of which the silicon dendrites are brought to the surface and the square indicates the area of figure 4.12a. Along the “bay” in the circular sample is where the sample is thin enough for electron transmission.

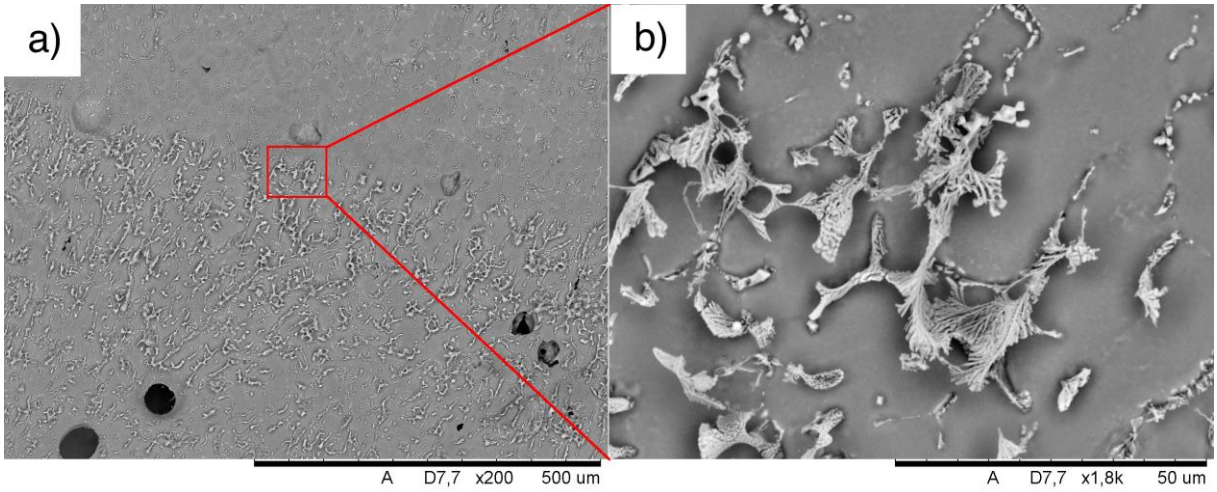


Figure 4.13: a) Boundary of where the silicon dendrites become protrusive. The red square indicates area of image b), which is a closer view of the dendrites sticking out of the aluminium surface.

The TEM analysis of the sample was carried out on the instrumentation described in section 3.11. The analysis, containing both imaging and EDS, enabled quantitative EDS results from local areas on and around the silicon dendrites. The images revealed that, although the dendrites had grown in to more than one aluminium grain, they often stuck out, i.e. in to vacuum, from in between the grain boundaries. Figure 4.14 shows a silicon dendrite sticking out from a grain boundary and figure 4.15 shows how it has grown in to the aluminium grains. Figure 4.15b also shows a small particle, marked by the red circle, situated within the indicated grain G2. The approximate diameter of the seemingly round particle is 260nm, which is very similar to the one observed in figure 4.7.

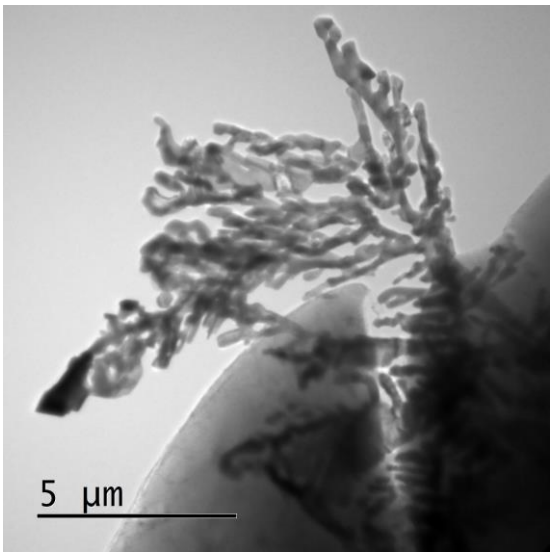

Figure 4.14: A silicon dendrite sticking out from an aluminium grain boundary into vacuum.

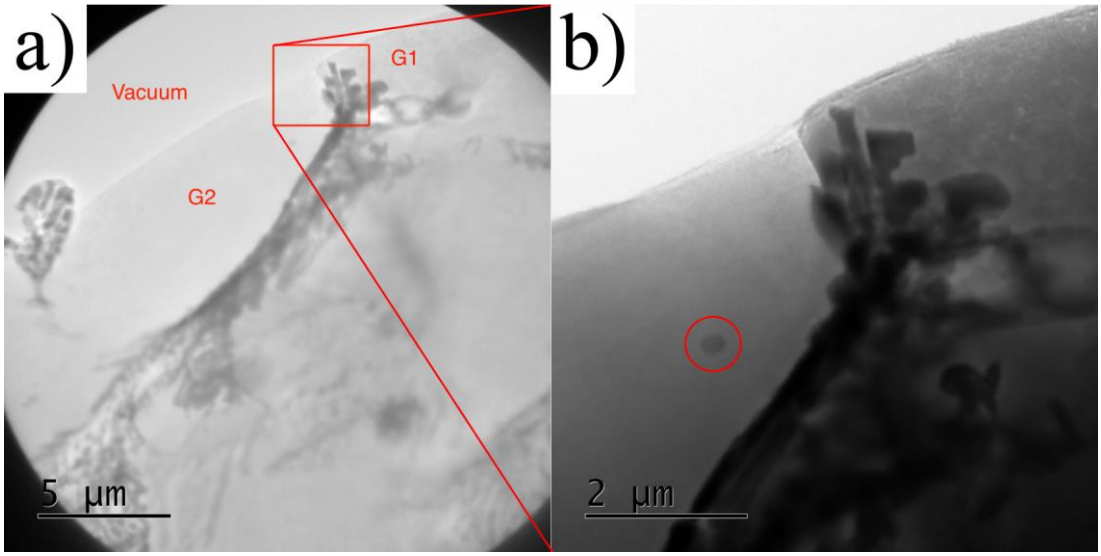


Figure 4.15: Silicon dendrites that have grown in to the grains G1 and G2 of aluminium. The image in b) also shows a small particle within the grain G2, indicated by the red circle.

A STEM mapping acquisition and quantification was performed on a few selected dendrite arms. The result is presented below by the images in figure 4.16, 4.17 and table 4.6. The image in figure 4.16a is a STEM image of the selected dendrite arms. A square indicates the area of EDS mapping and a second square indication the region of spectrum acquisition. Figure 4.16b shows the elemental EDS maps of silicon, aluminium and oxygen. The maps do not reflect the true silicon-aluminium-oxygen ratio, because the maps have a linear intensity distribution. However, one can get an idea of where the different elements are situated. If the spectrum (figure 4.17) and quantification is taken into consideration, one can observe that the dendrites consist of mainly silicon (87 at%), small amounts of aluminium 10 at% and even smaller amounts of oxygen 3 at%.

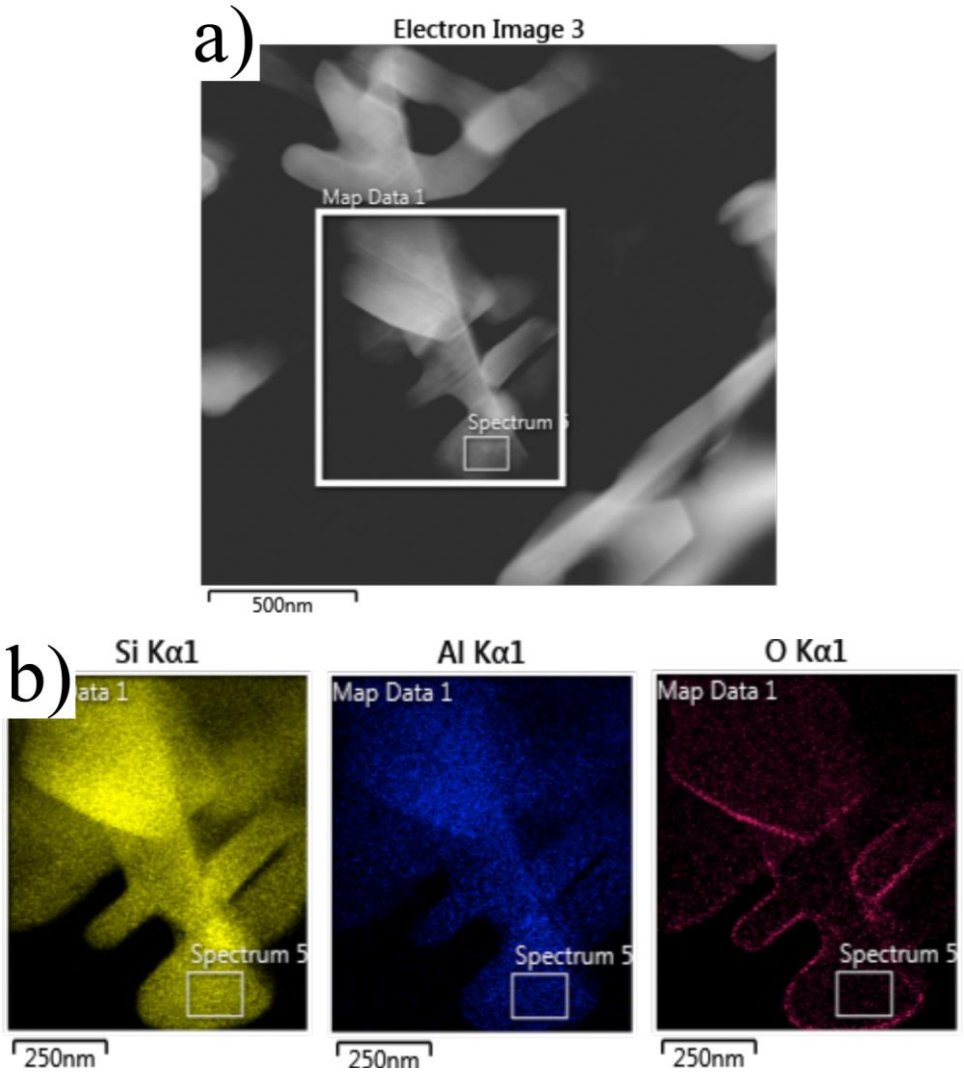


Figure 4.16: a) STEM image of the selected dendrite arms for examination. b) Elemental maps of silicon, aluminium and oxygen. The images show that the dendrites are of high purity and that the oxygen is situated at the edges of the dendrite arms.

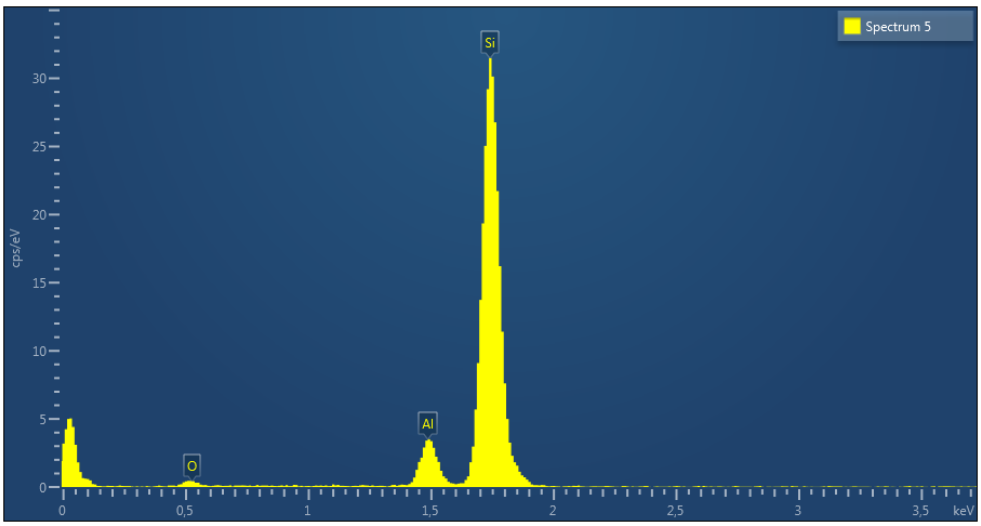


Figure 4.17: EDS spectrum of the area marked in figure 4.16a. A large silicon peak dominates the spectrum. The smaller aluminium peak is observed to the left of the Si-peak. Oxygen is present, but the detected signal from it is very low.

**Table 4.6 – Quantification from the Si dendrite region marked in figure 4.16:**

| Element: | Wt%: | At% |
|---|---|---|
| O | 1.5 | 3 |
| Al | 9.5 | 10 |
| Si | 89 | 87 |

Further investigation of the silicon dendrites was performed by BF- and DF-imaging and selected area diffraction. The BF image is an example of a dendrite consistent with the [001] zone axis pattern of Si. The contrast in figure 4.18a) may indicate several different crystal orientations within the dendrite. However, SAD pattern in figure 4.18b) is a single crystal pattern.

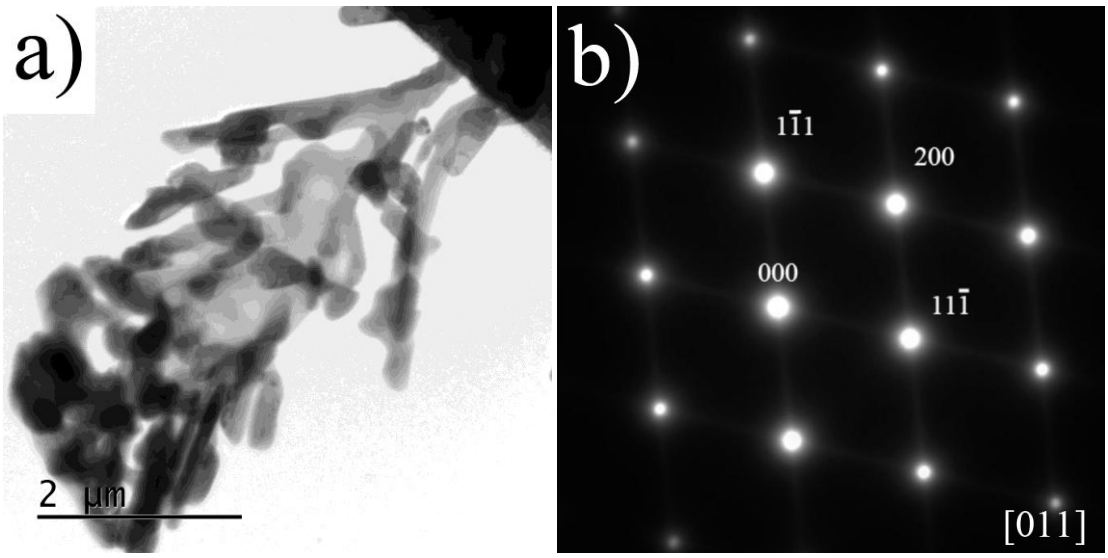


Figure 4.18: A BF image of a silicon dendrite with the corresponding DP along the [001] zone axis.

The DF images of the same dendrite as in figure 4.18, is presented in figure 4.19. The contrast is changing within the dendrite and reveals different crystal orientations. The diffraction patterns, where smaller SAD apertures were used, showed streaking along the ⟨111⟩-directions as seen in figure 4.19d). Streaks in the diffraction pattern are consistent with scattering from thin plate-shaped regions in the specimen. As seen in c), DF images having contribution from the streaks along the 11$\bar{1}$ row is seen in fig 4.19a) and b).

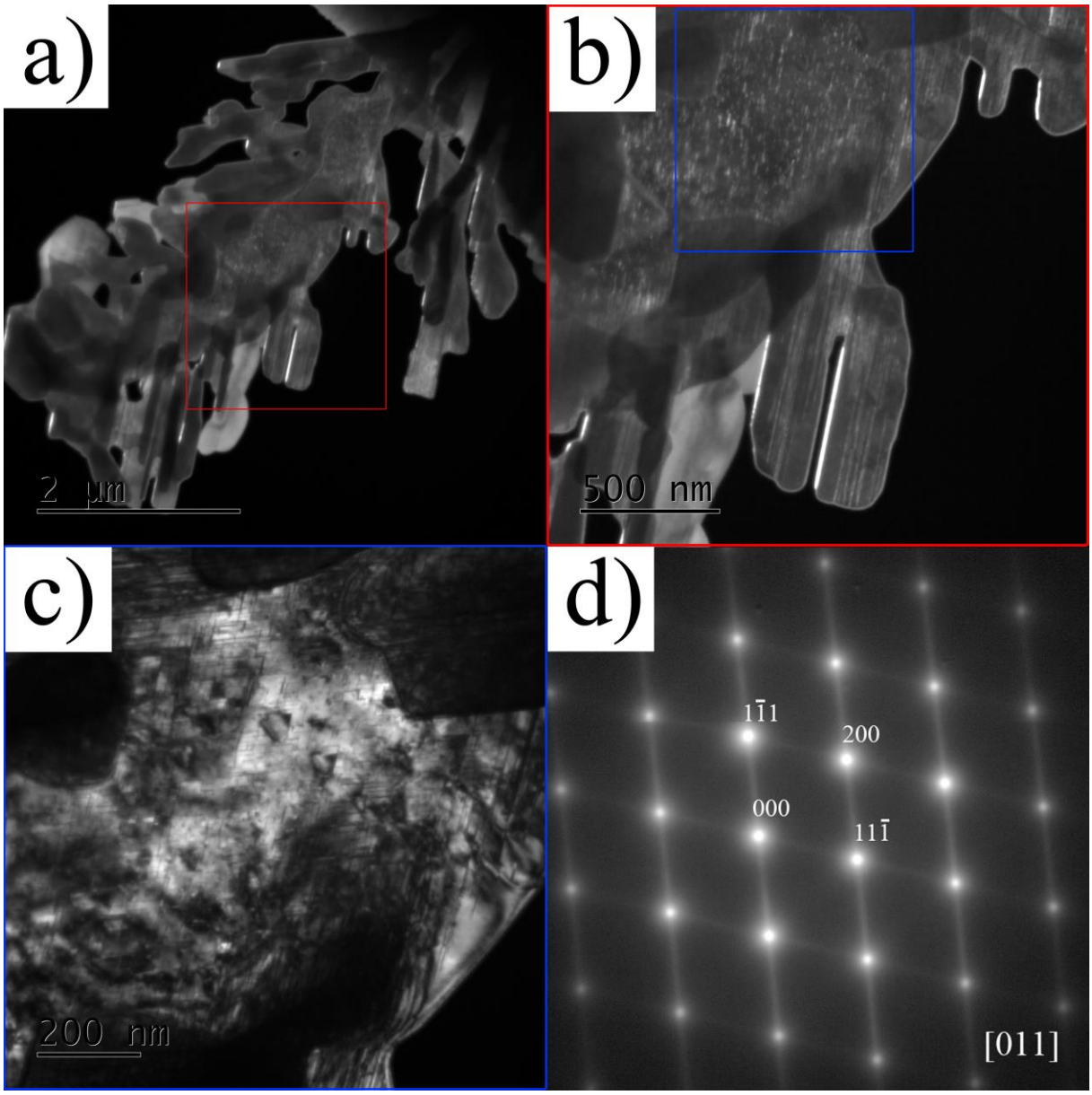


Figure 4.19: a)-c) DF images revealing thin plate shaped regions in a Si-dendrite with corresponding SAD pattern showing diffuse streaks along the ⟨111⟩-direction.

The bright lines inside the dendrite, seen in the DF image are consistent with planar faults or precipitation of plate like particles.

The DP in figure 4.20 is acquired at the root of which dendrite arms grow in separate directions. The DP has a separate set of diffraction spots. These appear to the left of the primary diffraction spots of silicon, and are called twins. Twinning in DP's occur as a result of two or more crystals sharing a common crystal plane, even though they grow in different spatial directions. In the DP, the primary diffraction spots are indicated by blue indices, whilst the twins have red colour and a lowercase "T".

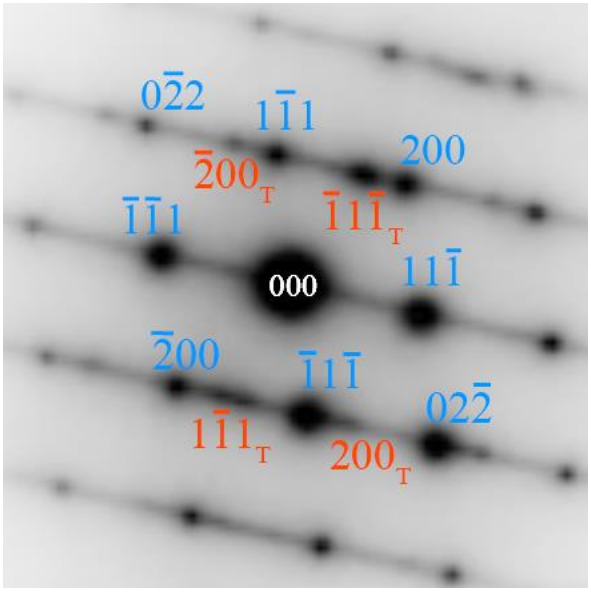


Figure 4.20: A DP exhibiting crystal twinning. Crystals sharing a common crystal plane cause the "extra" diffraction spots. The twin diffraction spot is indicated with red colour indices and a lowercase "T".

A high resolution TEM (HRTEM) image was acquired from an area on the silicon dendrite (figure 4.21). In some areas, as indicated in figure 4.21, a contrast variation can be seen. This can be associated with localised strain in the lattice. Dislocations are also seen in the same region as illustrated in figure 4.22. The presence of strain and dislocations can be due to the presence of intermetallic particles.

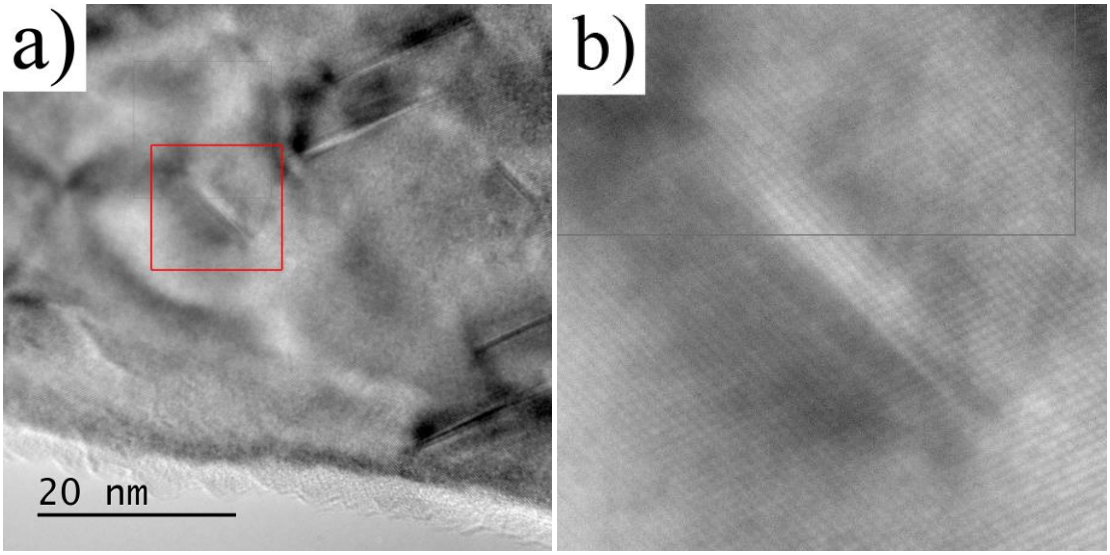


Figure 4.21: a) HRTEM image showing an irregular symmetry caused by dislocations. b) A magnified image of the selected area for image filtering.

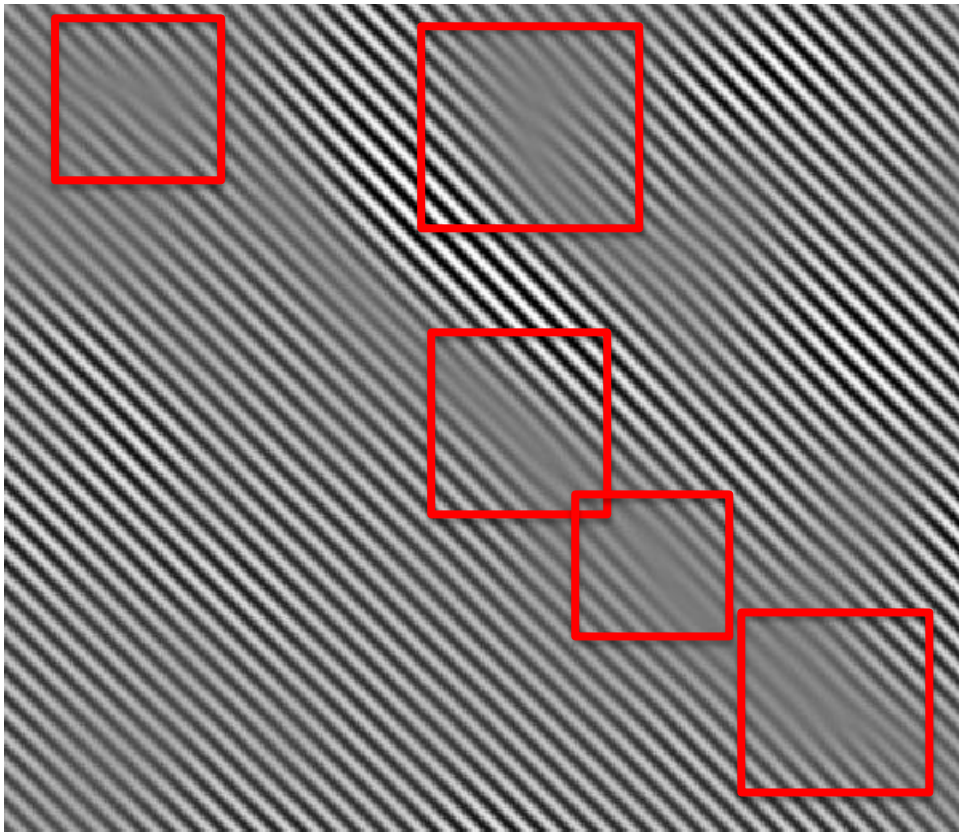

Figure 4.22: An intensity filtered image from the Si dendrite region in figure 4.21 b) where locations of dislocations are indicated.

### 4.2 Sample AA4020_S2

The second sample of the AA4020 alloy was deposited by the multiple-axis robotic welder equipped with the cold metal transfer (CMT) unit and consists of 22 layers. A corresponding cross section sample piece is displayed in the figure below, where a) is untreated and b) is the polished sample. The wall structure has a sinuous structure, suggesting too much heat input during deposition. In addition, the alloy is designed to have a great fluidity, which seems to be very pronounced on this deposited wall structure. The polished cross-section exhibit similar layers, related to the HAZ, as the first sample of the same alloy.

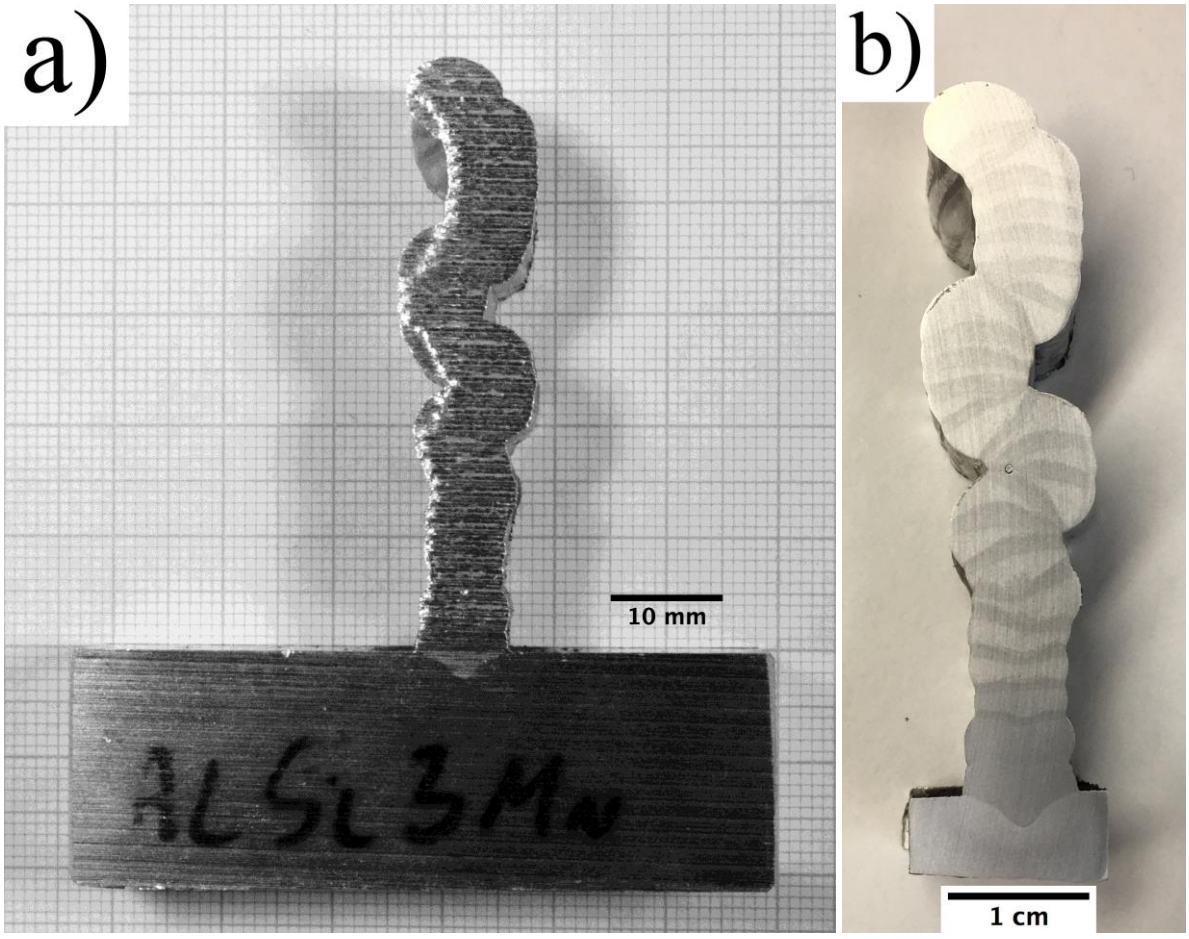


Figure 4.23: Cross-section images of the second deposited wall of the AA4020 alloy. a) Display the untreated sample and b) is the polished sample revealing the HAZ.

### 4.2.1 Mechanical properties of sample AA4020_S2

#### Tensile tests

A total of seven tensile samples were made of sample wall AA4020_S2. Three was extracted from the walls horizontal direction and four from the vertical direction. The tensile strengths in the horizontal direction were measured to 181.13-, 181.84- and 190.34MPa, for the test samples S2_H1, S2_H2 and S2_H3, respectively. In the vertical direction samples, the values were measured to 191.1-, 189.8-, 172.5- and 189.0MPa of the samples S1_V1, S1_V2, S1_V3 and S2_V4, respectively. The differences between the two directions are minor. The average of the tensile strength in the horizontal direction is ≈184.44MPa and the average value in the vertical direction is 185.6MPa. The difference is, thus, only ≈1.16MPa. The yield strengths were calculated to 82.7-, 82.7- and 97.2MPa for the test samples of S2_H1, S2_H2 and S2_H3 in the horizontal directions, respectively. In the vertical direction the yield strengths were measured to 119.5-, 88.3-, 80.7- and 97.5MPa for the samples S2_V1, S2_V2, S2_V3 and S2_V4, respectively. The average yield strength in the horizontal direction was ≈87.53MPa and in the vertical direction =96.5MPa. The difference is ≈8.97MPa, which means that the vertical direction shows higher yield strength. As with the sample AA4020_S1, these values are a sign of good fusion between the weld beads. The strain values were measured to an average value of 0.2196mm/mm in the horizontal direction and ≈0.1835mm/mm in the vertical, which means that the ductility in the horizontal direction is greater than in the vertical. This could be a sign of better fusion in the horizontal direction and is as expected, because horizontal direction mainly consists of a single weld bead. The nominal stress-strain curves in figure 4.24 show the result and table 4.7 show the calculated strength values.

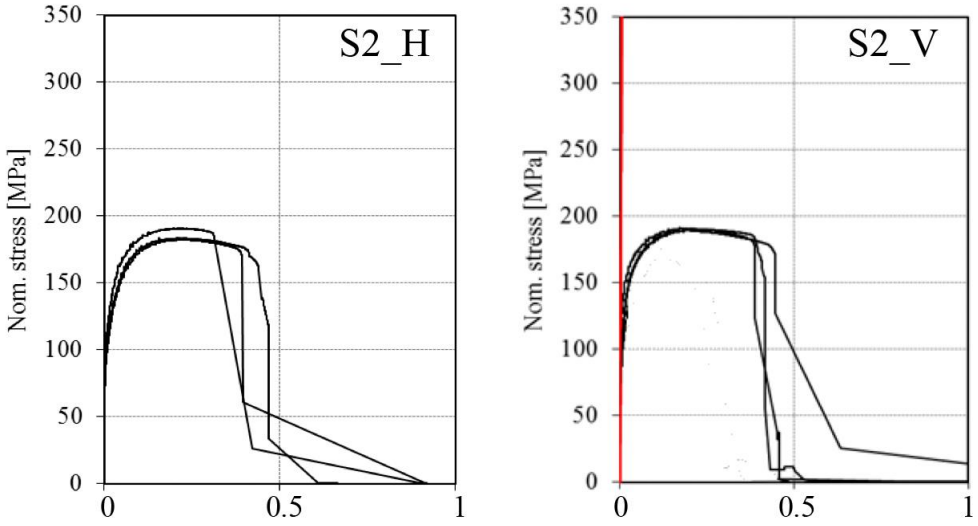


Figure 4.24: Stress-strain curves for tensile tests from the AA4020 alloy sample S2. The curve to the left shows the result from the test samples taken in the horizontal direction. The curve to the right shows the result from the samples extracted in the vertical direction.

**Table 4.7 – Tensile test results of sample AA4020_S2:**

| **Test specimen ID:** | **Diameter [mm]:** | **Yield strength $R_{p0.2}$ [MPa]:** | **Tensile strength $R_m$ [MPa]:** | **Strain at max. load $A_{gt}$ [mm/mm]:** |
|---|---|---|---|---|
| S2_H1 | 2.937 | 82.7 | 183.13 | 0.2199 |
| S2_H2 | 2.938 | 82.7 | 181.84 | 0.221 |
| S2_H3 | 2.926 | 97.2 | 190.35 | 0.2179 |
| S2_V1 | 2.953 | 119.5 | 191.1 | 0.17115 |
| S2_V2 | 2.943 | 88.3 | 189.8 | 0.2381 |
| S2_V3 | 2.929 | 80.7 | 172.5 | 0.127 |
| S2_V4 | 2.934 | 97.5 | 189.0 | 0.1979 |

**Hardness tests of the sample AA4020_S2:**

The Vickers hardness tests consisted of 54 indentations and were acquired from 4mm into the base material (AA5754 alloy) and to the top of the sample. The hardness decays as the indentations get closer to the deposited material (DM), from 73.8HV at the first indentation, to 56.9HV at the indentation acquired at the zero-position, i.e. at the interface between the first layer and the base material. The decay is likely an effect of the penetration of the DM into the base material, causing a HAZ with weaker hardness properties. In addition, the hardness of the DM decays in the build direction with a value of ≈-0.13HV per indentation, in average. The maximum hardness value on the DM was 58.6HV and the minimum 45.2HV. The average hardness value was 51.5HV. The plot of the hardness values as function of distance in y-direction is shown in figure 4.25 below and the linear regression plot used to estimate the values of the DM is shown in appendix figure A.5.

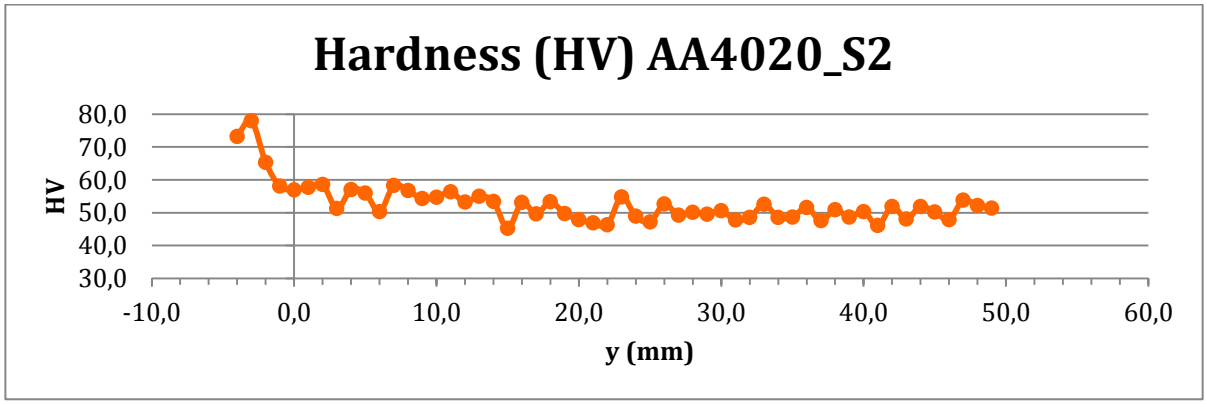


Figure 4.25: Plot of hardness (HV) as function of distance in the y-direction. The curve shows a decay towards the cap layer.

**Porosity measurements of the sample AA5083_S3:**

Figure 4.26 below is a plot of all the pore positions in the x- and y-directions on the sample. As seen in the figure the sample has many pores and they seem to accumulate at the edges and at the interfaces between the weld beads. Figure 4.27 is a plot of the pore area as function of distance. This plot show that the average pore area peaks in two areas. The first area is between ≈1cm up the wall, and past the first major bump at ≈2.7cm in the y-direction. The second is between ≈3.3cm up the wall and to the top. In both areas there are bumps where the edges seem to be very porous as seen from figure 4.26. However, the bump that points upwards in figure 4.26 does not seem to affect the average pore area and there are visibly less porosity there.

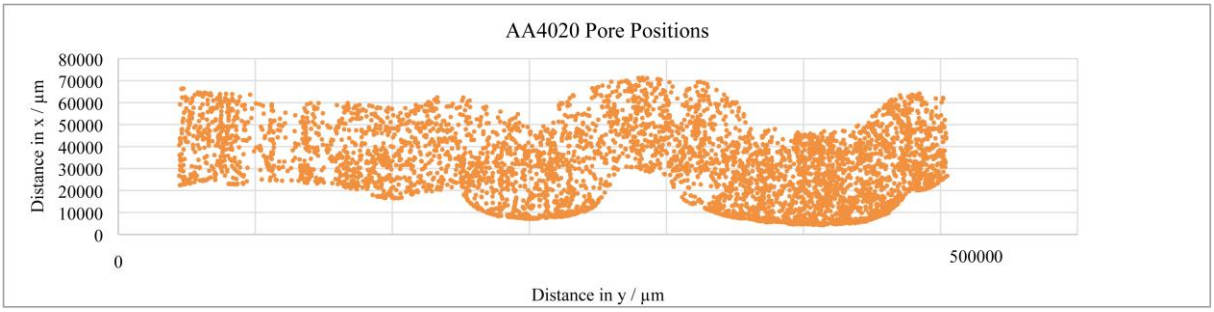


Figure 4.26: A plot of all the measured pores in the respective x- and y-directions on the sample. The pores seem to accumulate at the edges and at the interfaces between the beads.

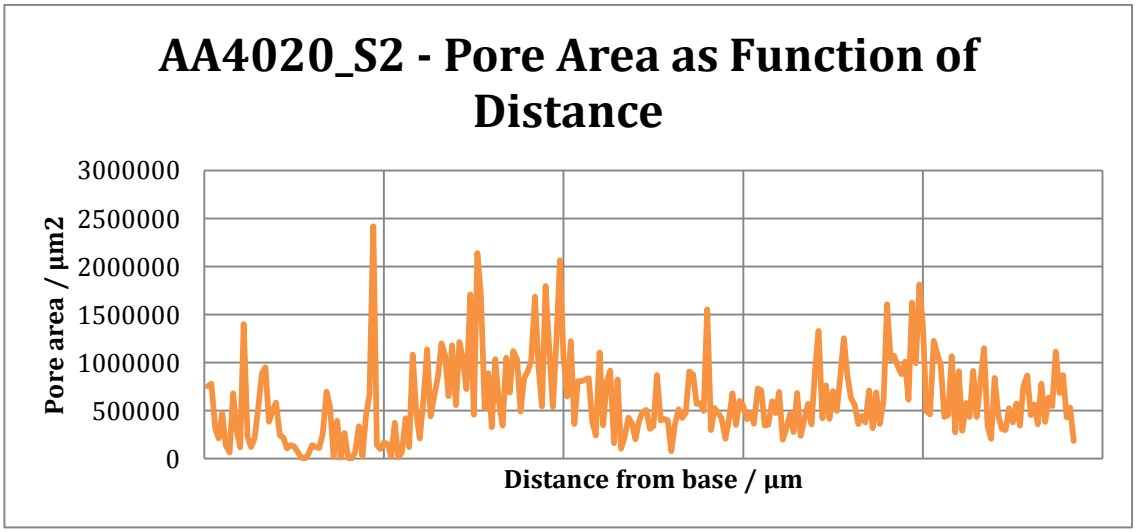


Figure 4.27: A graph showing the pore area as function of distance on the sample. It shows two major regions of higher average pore area. These areas are consistent with two of the bumps who points downwards in figure 4.26.

### 4.3 Sample AA5083_S3

The first sample of the AA5083 alloy consists of 22 deposited layers. The height of the sample wall was ≈5.4cm and the width ≈0.5cm. The image below, figure 4.28a, shows the untreated, polished, and electro-polished cross section of a piece of the deposited wall. It is quite straight, apart from one bump mid-way up the wall, which makes it the most similar to the 3D modelled structure of the produced wall structures. Simple polishing of the cross section made the surface very shiny, but without the reflection effects of the HAZ that was observed on the AA4020 alloy. However, the reflection effects were visible after grinding at certain grit sizes. The strongest effect was achieved after grinding with #1200 wet sanding papers, but the effect was too vague to be sufficiently captured by a simple camera. A few pores were observed and some scratches that did not seem to go away, no matter how long it were polished, which is a likely to be intermetallic particles that falls off during preparation. The image below, in figure 4.28b, shows the mirror-like polished surface. In order to reveal more of the microstructure, a piece of the cross section was electro-polished as described in section 3.5.1. Figure 4.28c shows an image of the sample piece after electro-polishing, where the HAZ has become highly visible. Another observation that can be made is that the HAZ are decreasing in size when studying it from bottom (substrate) to top. One can also see where the mask has been covering the sample and an area of which the electrolyte have not been sufficiently flushed off, leaving an etched, overexposed, area.

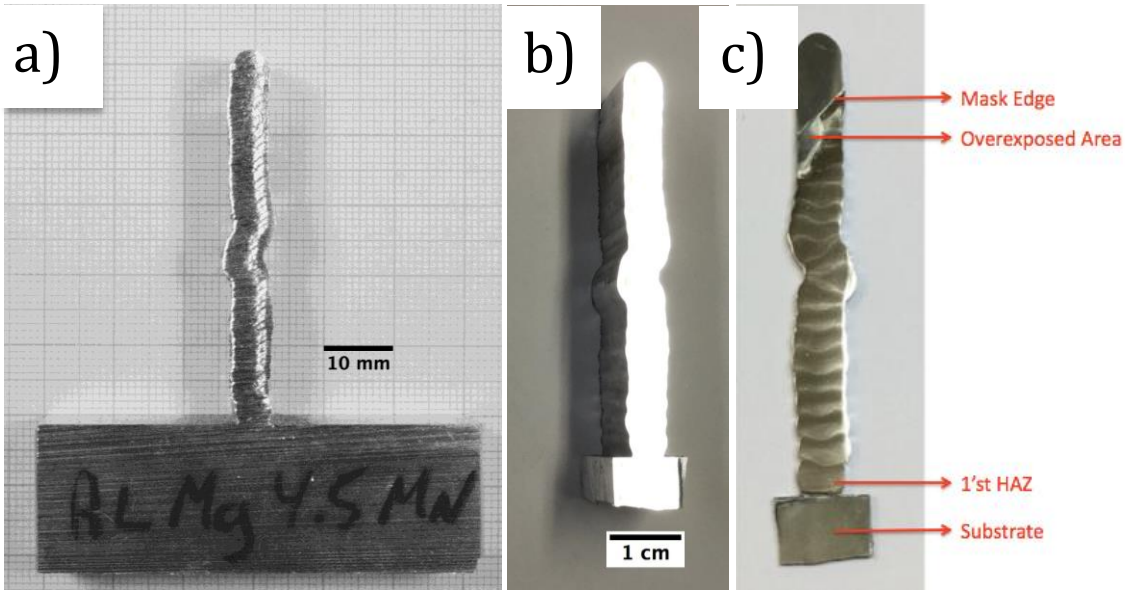


Figure 4.28: Cross section images of the AA5083 wall structure. a) shows the untreated cross section. b) Shows the mirror finish after polishing and c) shows the sample cross section after electro-polishing, where the HAZ has become visible. The size of the HAZ decays in the vertical direction and is an effect of reheating during deposition.

### 4.3.1 Mechanical properties of sample AA5083_S3

#### Tensile tests

Six tensile test samples were made from the AA5083 alloy, three in the horizontal direction and three in the vertical direction of the wall structure. Figure 4.29 show the measured nominal stress-strain curves. The measurements are collected in their respective directions of extraction from the wall structure. That is, the collection of curves in the figure to the left (below) is all of the horizontal test samples, whilst the figure to the right (below) is the collection of all the samples extracted from the vertical direction of the deposited wall structure. The horizontal test samples had an average Yield strength value of 144.3MPa and the vertical direction had an average yield strength value of 149.5MPa. The average tensile strength values were 310.1 in the horizontal direction, and 243.4MPa in the vertical direction. The substantial difference between the two directions can be observed in figure 4.29 below. The curves measured in the horizontal direction have the characteristic plastic stress-strain curve of a reasonably ductile material. However, the curves from the vertical test specimens shows

fracture after a very short elongation, which is reflected in the measured strain values. The average horizontal strain value was 0.2868mm/mm, whilst the average vertical strain was measured to 0.0612. This shows that, although the sample has high yield strength, it breaks abruptly after maximum force is applied. The calculated strengths and strain are shown in table 4.8 below.

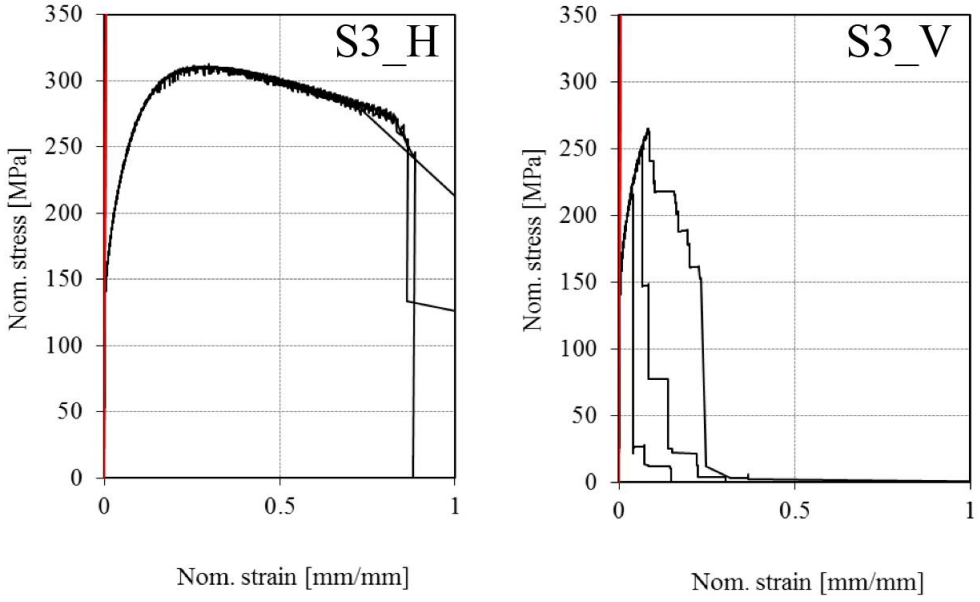


Figure 4.29: Stress-strain curves for tensile tests from the AA5083 alloy sample S3. The curve to the left shows the result from the test samples taken in the horizontal direction. The curve to the right shows the result from the samples extracted in the vertical direction.

**Table 4.8 – Tensile test results of sample AA5083_S3:**

| **Test specimen ID:** | **Diameter [mm]:** | **Yield strength $R_{p0.2}$ [MPa]:** | **Tensile strength $R_m$ [MPa]:** | **Strain at max. load $A_{gt}$ [mm/mm]:** |
|---|---|---|---|---|
| S3_H1 | 2.961 | 145.8 | 310 | 0.2901 |
| S3_H2 | 2.964 | 144 | 309.8 | 0.2853 |
| S3_H3 | 2.97 | 143 | 310.4 | 0.28505 |
| **S3_H_avg.**[1] | **2.965** | **144.3** | **310.1** | **0.2868** |
| S3_V1 | 2.967 | 149 | 264.5 | 0.0821 |
| S3_V2 | 2.972 | 152 | 216.3 | 0.037 |
| S3_V3 | 2.969 | 147.5 | 249.5 | 0.06439 |
| **S3_V_avg.**[1] | **2.969** | **149.5** | **243.4** | **0.0612** |

[1]avg=average value in respective direction.

### Hardness tests

The results of the Vickers hardness tests are presented by the graph in figure 4.30 below. The graph is made out of the plotted values of Vickers hardness (HV) and distance in mm on the sample. Some of the indentations were performed on the base material, because the deposited material had a section welded to it. The zero-point is therefore set at the beginning of the first weld bead. The graph shows that the hardness across the sample is lower than of the base material. One sees that the hardness drops at a point (≈-3mm) into the base material. This is likely to be an effect of the heat dissipation from the weld. The average hardness of the deposited material is 77.6HV and the maximum- and minimum values are 88.8HV and 73.2HV, respectively. A linear regression of the scattered points shows that the hardness has a small decay in the y direction. That is, the hardness gets lower towards the last deposited layer. The linear regression can be seen in appendix, figure A.2.

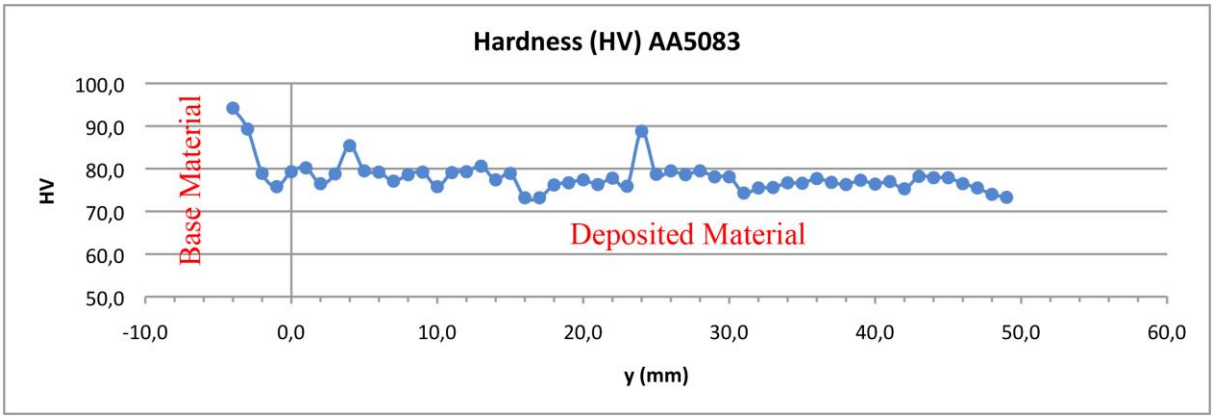


Figure 4.30: A graph showing the plotted Vickers hardness (HV) versus the position in y-direction in mm. The average hardness of the deposited material is 77.6HV and it is decaying a small amount in the y-direction.

**Porosity measurements of the sample AA5083_S3:**

The porosity measurements were performed as described in section 3.8. The result is plotted below in figure 4.31. The figure is composed by the pore positions relative to the sample dimensions in x- and y-direction. An image of the sample is inserted to make it easier to interpret where the pores are located at the sample wall. It seems, from the image, that the pore-concentration is higher towards the edges. In addition there is higher pore-concentration at the interface between the substrate and the first weld bead. The supplementary graph in figure 4.32 indicates that the pore-concentration is increasing slightly towards the top of the sample (in y-direction).

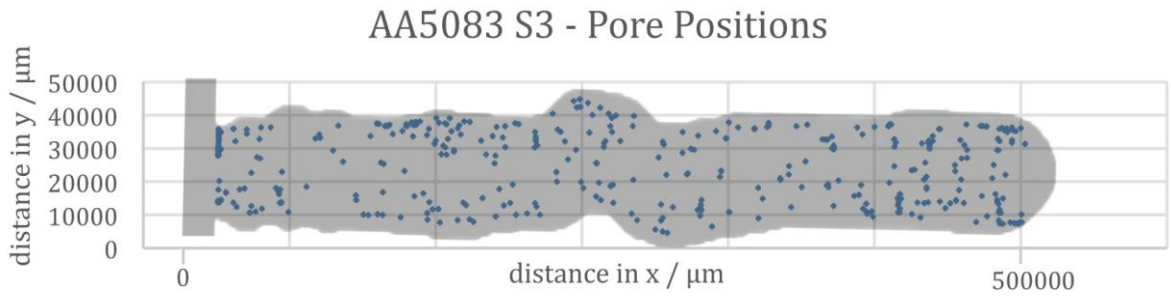


Figure 4.31: A plot of the pore-positions relative to the sample dimensions in x- and y-direction. The figure shows that there is a higher pore-concentration towards the edges of the sample.

The graph in figure 4.32 shows the pore area as a function of distance. The graph is therefore changed towards higher values if a higher number of pores are located in one area. It also changes towards higher values if larger pores are present, because the average pore area increases. As mentioned previously, the graph indicates that the number- or the size of the pores increases towards the top of the wall, i.e. in the y-direction. A large peak can be seen in the graph in figure 4.32. This most likely indicates a large pore, because figure 4.31 does not show any accumulation of pores at the center of the sample.

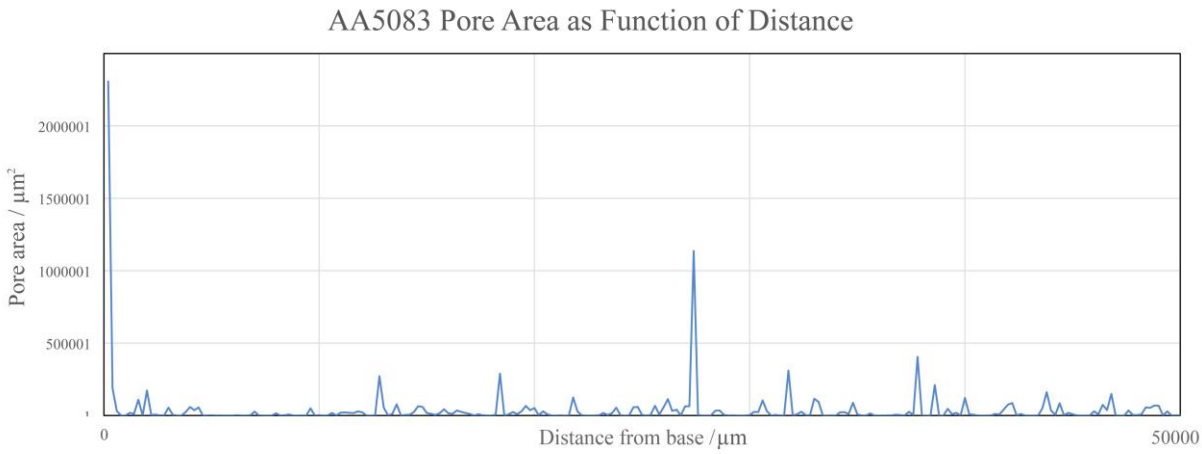


Figure 4.32: A graph displaying the pore area as function of distance in y-direction. The graph indicates that either the number of pores increases towards the top of the wall, or that the size of the pores does. The large peak most likely indicates a large pore close to the center in the y-direction of the sample

### 4.3.2 Microstructure of sample AA5083_S3

#### Wall-substrate interface

The border between the deposited material and the substrate were analysed with the polished sample wall. To get an idea of how well the weld had fused in to the base material. The image below (figure 4.33) shows accumulation of pores at the interface between the substrate and the deposited material, and the elemental maps show that the pores are rich in carbon. This could be an effect of the sample preparation, but it could also be from the deposition of the material. The accumulation of pores close to the substrate is consistent with the plot in figure 4.31. From the elemental map of magnesium, one can see that there is a lack of fusion of the magnesium rich AA5083 alloy in to the AA5754 substrate. It seems that the deposited material is somehow pushed back, rather than fusing the material, which could be an effect of when the molten material meets with the cold substrate. From the map one can also see that there are a few areas of higher magnesium content, appearing as branches growing up from the wall-to-substrate interface. In addition, where the magnesium branches grow, the aluminium concentration has decreased, indicating a second phase. A few silicon rich spots are also observed, which is a sign of precipitation. The circle in the image below indicates an area of where quantification was performed. The result of the quantification is reproduced in table 4.9 below, which is acquired from an area that reflects the composition of the deposited material.

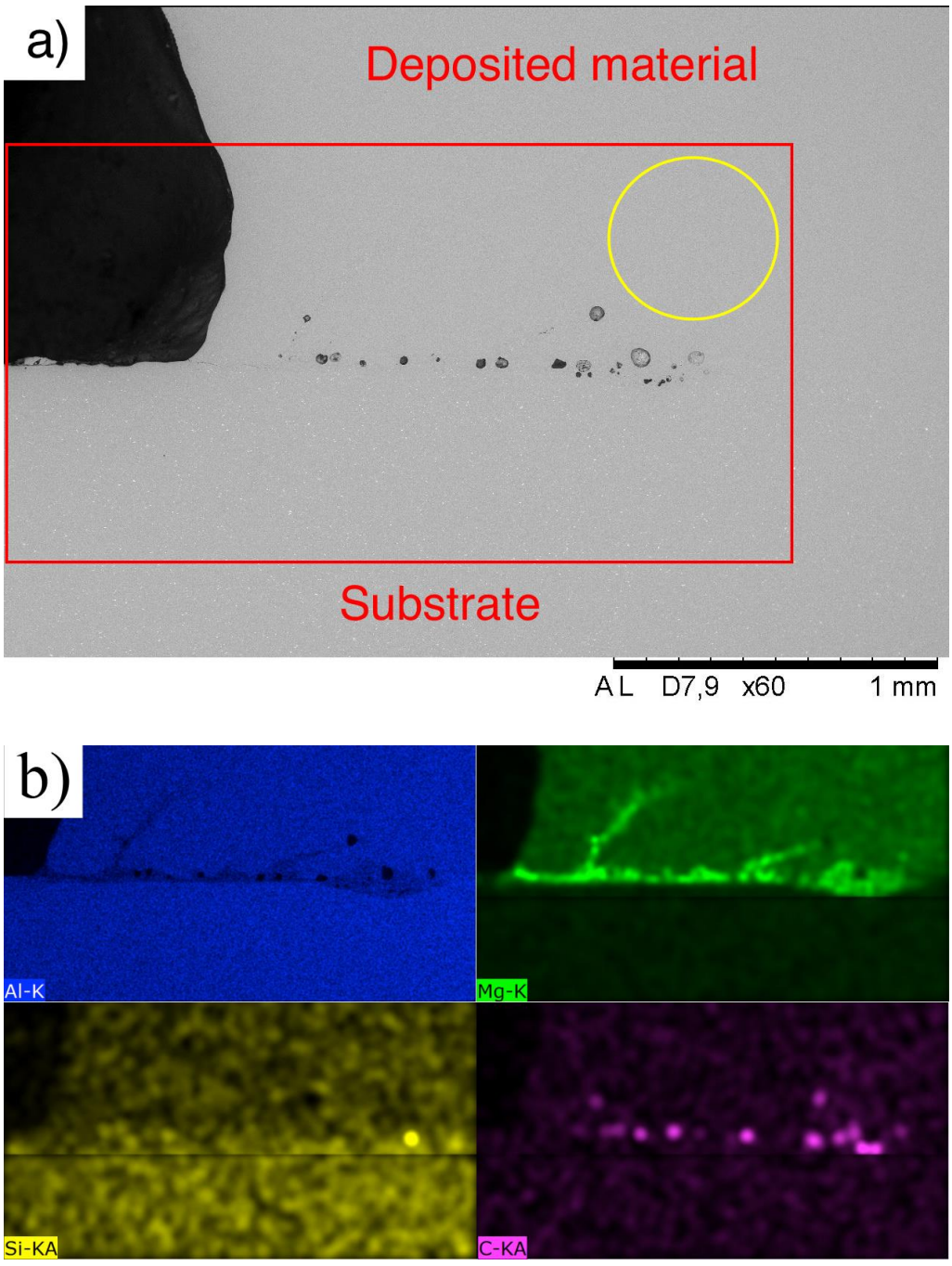


Figure 4.33: a) image of the boundary between the deposited material and the substrate with indications of the area (square) of where the EDS maps are acquired from, and the area (circle) of where the quantification were acquired. The image also shows several pores along the interface between the substrate and the deposited material. b) EDS elemental maps of aluminium (blue), magnesium (green), silicon (yellow) and carbon (purple). The maps reveal a change in magnesium content in certain areas, which consequently lack aluminium. A bright precipitate of silicon is observed. Carbon is connected to the pores, which could be from the sample preparation and also from the material deposition.

**Table 4.9 – Quantification of area in figure 4.33:**

| Element: | Normalised C. [wt%]: | Atomic C. [at%]: | Error [%]: |
|---|---|---|---|
| Aluminium: | 90 | 85 | 4 |
| Carbon: | 5 | 10 | 1 |
| Magnesium: | 4 | 4.6 | 0.2 |
| Manganese: | 0.7 | 0.30 | 0.0 |
| Iron: | 0.1 | 0.05 | 0.0 |
| Silicon: | 0.05 | 0.05 | 0.0 |

The quantification reflects the composition of the deposited material, without including abnormalities, such as the magnesium rich areas in figure 4.33. The results are in good agreement with the initial alloy composition (table 2.2). Slightly higher magnesium content was expected (4wt%), This could be an accumulation-effect of magnesium, similar to what the maps in figure 4.33 showed. It could also be that the initial weld wire had lower magnesium content, but it is less likely.

**Cap layer**

The uppermost part of the wall, which is made by the last weld bead, is called the cap layer. It is the least affected part of the structure and it represents a scenario similar to a single deposited weld bead. The image in figure 4.34 a) shows the lightly etched cap layer, in which the grain structure became enhanced. A closer view is presented in b), which was used to estimate the grain sizes. The lengths across the grains in the image ranged from ≈70μm to ≈140μm, with an average of ≈105μm. The image in c) reveal the aluminium dendrites, and a lot of intermetallic particles situated between the visible dendrite arms.

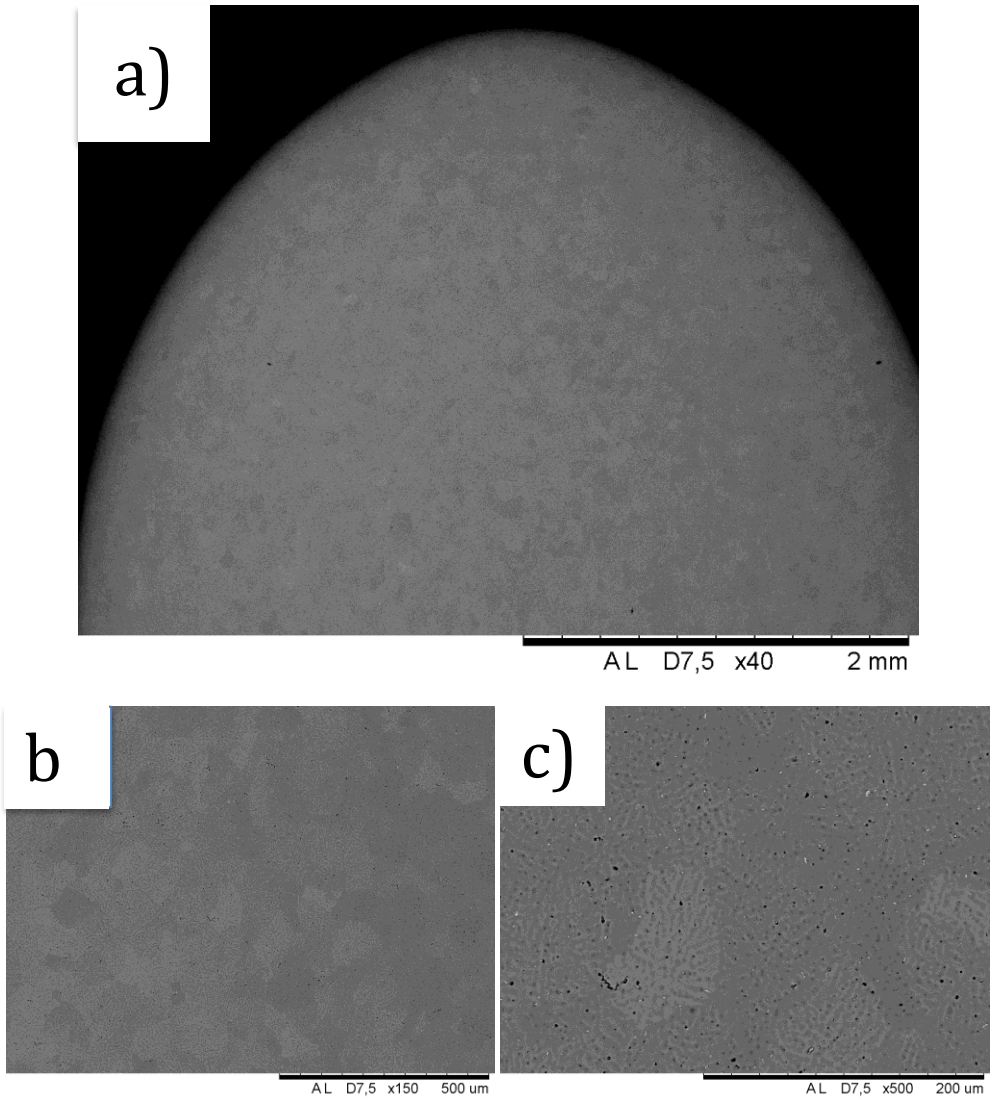


Figure 4.34: Image of the cap layer, lightly etched. The grain structure became enhanced, which made it possible to estimate the grain sizes. The image in a) shows the cap layer of the wall, where the visible grain structure is seen. B) shows a magnified image, which could be used for measuring the sizes of the grains. C) shows the dendritic structure within the grains and intermetallic particles in between the arms.

A similar area was selected for EDS analysis. The intent was to reveal how the intermetallic particles collected around the dendrites. Several holes are also observed, which is either pores or intermetallic particles that has fallen out during sample preparation. The result of the analysis is presented below and shows how the areas between the dendrites have higher magnesium content. Indicating two main phases within the material.

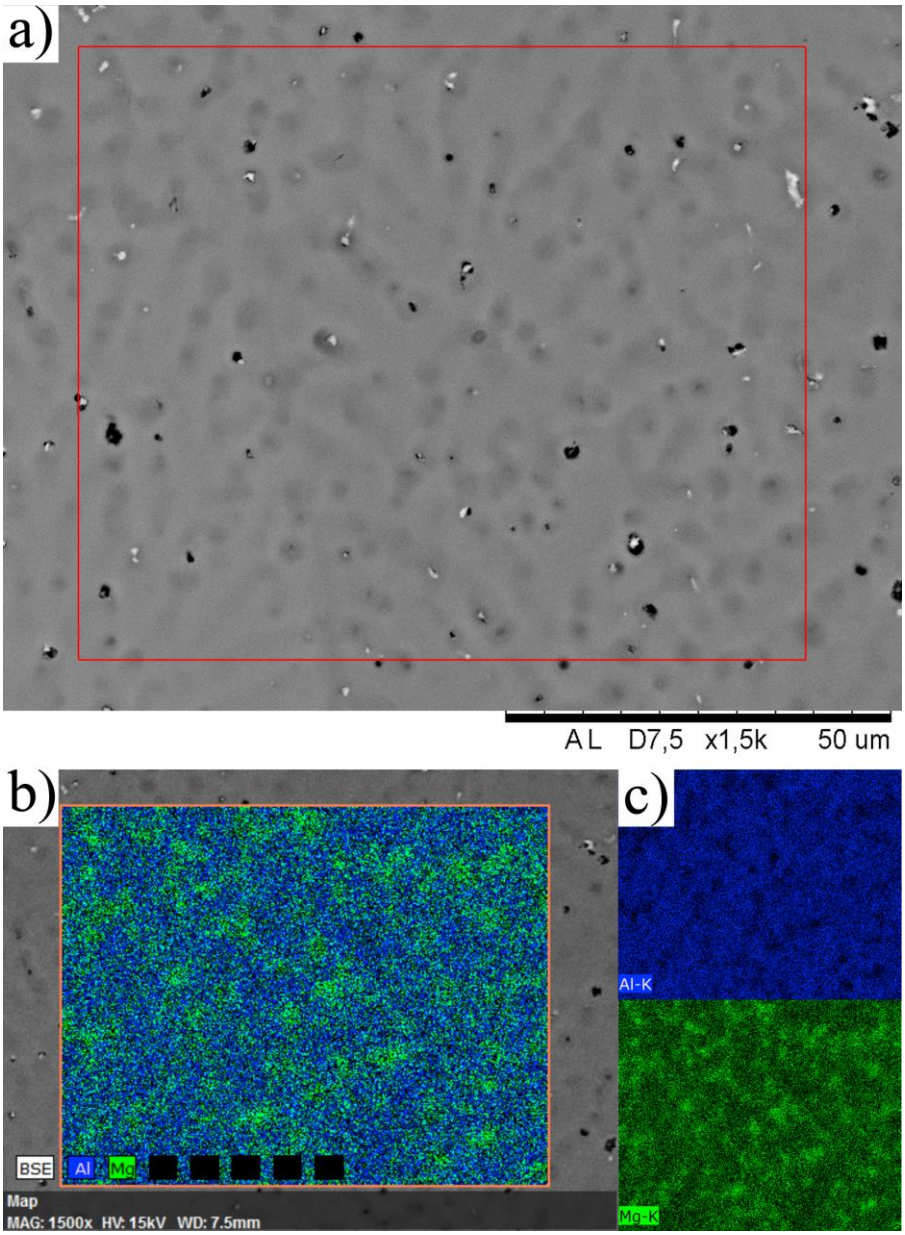


Figure 4.35: a) image of the area where the analysis was performed. The image shoe intermetallic particles in between dendrite arms. Holes are also present, indicating pores or intermetallic particles that has fallen out. b) Show a layered image, composed of BSE, Al and Mg. The image show how the magnesium is situated between the observed aluminium dendrite arms. c) Are the elemental EDS maps of Al (blue) and Mg (green), enhancing the variation.

**Center area**

The images below are acquired from an area close to center of the sample width, outside the HAZ on the polished wall. The area is assumed to be an average of the overall midsection of the wall, which means that it is representative for what is left after the final machining of a final product. Of course, the HAZ is also a part of the midsection and will be investigated further below. The image in figure 4.36b shows quite even distributed intermetallic particles. The orange square indicates the area of EDS acquisition, presented in figure 4.36c and d). Figure 4.36c displays a layered image of the collected aluminium (blue) –and magnesium (green) signal at the same intensity. It reveals a fairly uneven distribution of the magnesium, similar to the observation in figure 4.35, but more in the shape of "stripes", rather than "dots". This observation can also be viewed in the elemental maps in figure 4.36d, which gives a better view of how the local increase in magnesium content relates to a decrease in aluminium.

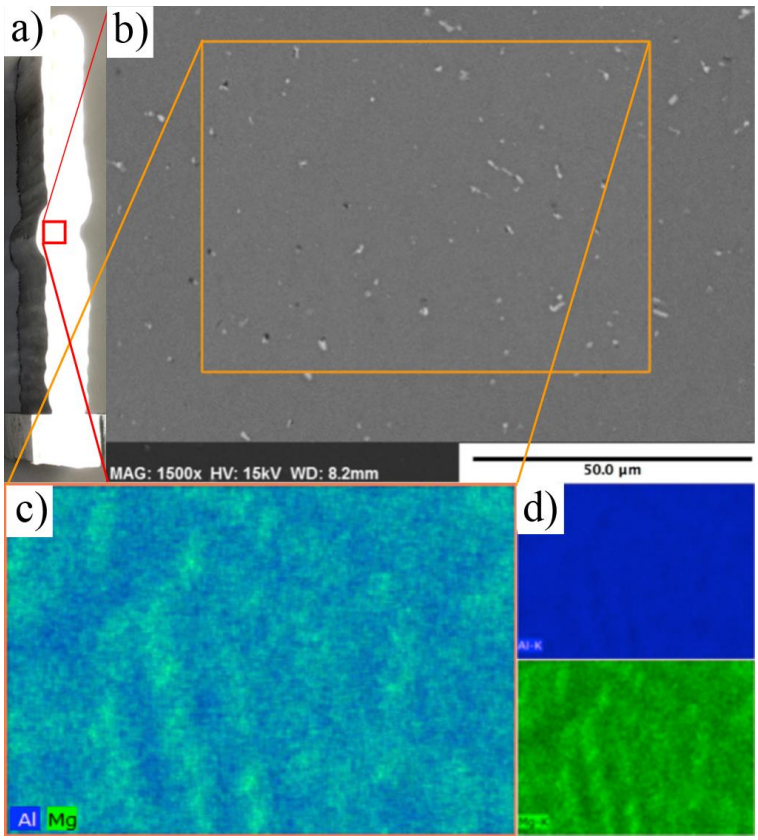


Figure 4.36: a) Indicates the area of analysis on the bulk sample. b) is the analysed area where a close to even distribution of intermetallic particles are observed. c) Is a layered image composed of the Mg- and Al-signal from the EDS-acquisition. The image shows a variation of magnesium. d) The elemental EDS maps of Al (blue) and Mg (green), which gives a better view of how the Al content decreases where the Mg content is increased.

The sample was electro-polished, in order to enhance the magnesium variation that was observed in figure 4.36. The selected area is outside of the HAZ, as with the previous area in figure 4.36. The result is presented below and shows an enhanced view of the magnesium variation. In addition to enhancing the contrast between Al and Mg, the aluminium dendrites became more visible in both the BSE image and the two others. This better seen in figure 4.37c, which are the elemental EDS maps of Al (blue) and Mg (green). Here, the aluminium map show how the dendrites are laying down with dark areas in between them. The magnesium fills these dark areas, which is better observed in the overlay image in figure 4.37d. It seems that the two elemental maps are the inverse of each other. Further improving the hypothesis of a two-main-phase material.

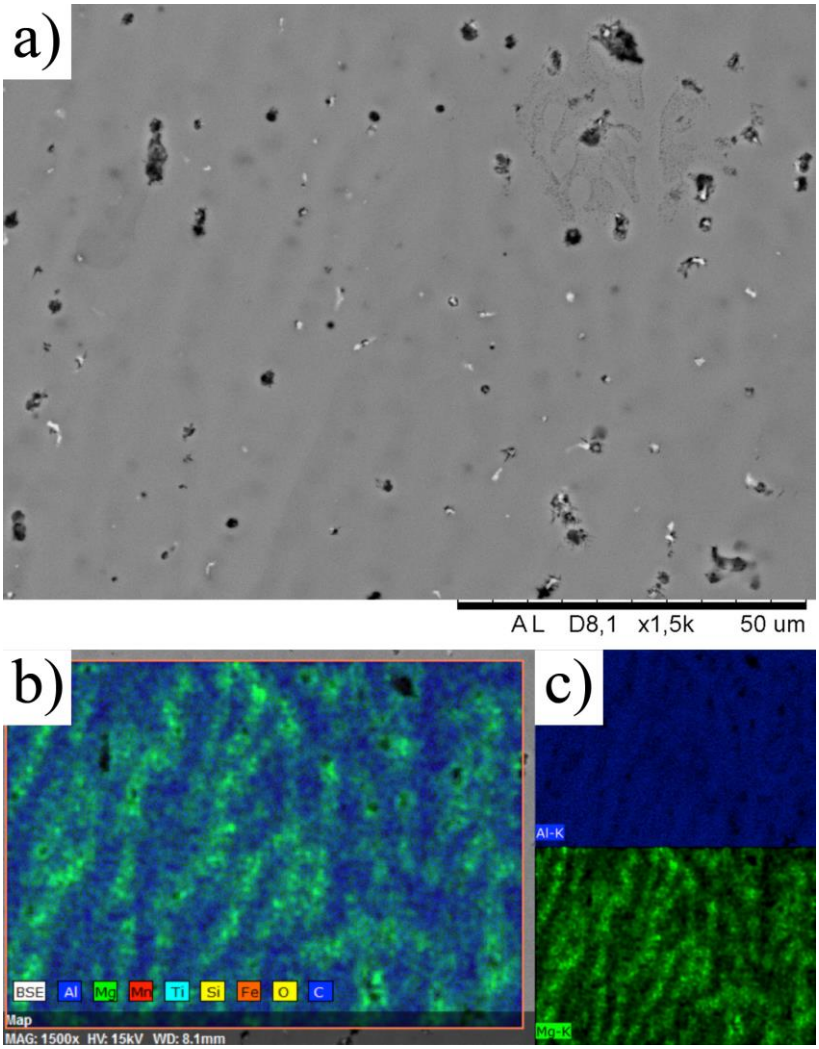


Figure 4.37: a) BSE image of an electro-polished area similar to the one in figure 4.36. The image shows a contrast difference between what looks like dendrites. Intermetallic particles are present here as well. b) layered image composed of BSE, Al and Mg showing a strong compositional variation. c) Elemental EDS maps of Al (blue) and Mg (green), revealing aluminium dendrites with darker areas in between the arms. A similar observation is seen in the map of Mg.

### Weld bead interfaces

A weld bead interface is observed right below the curvature on the sample cross-section edge. The interface is recognized by the fracture, which starts at the edge and continues approximately 200 μm towards the center, and by the accumulation of pores. The accumulation of pores is higher right above the fracture, i.e. at the start of the subsequent weld bead. The elemental maps show that there the magnesium content is higher at the beginning of a new weld bead, than at the end of the previous. As with the wall-to-substrate interface, the magnesium-aluminium ratio is connected. That is, where there is a higher magnesium concentration, there is less aluminium, and vice-versa. In addition, precipitation of secondary phases seems to be situated at very beginning of the subsequent weld bead. The observed intermetallic particles have needle-like shapes, and are rich in manganese and iron. A few independent intermetallic particles of silicon are also observed.

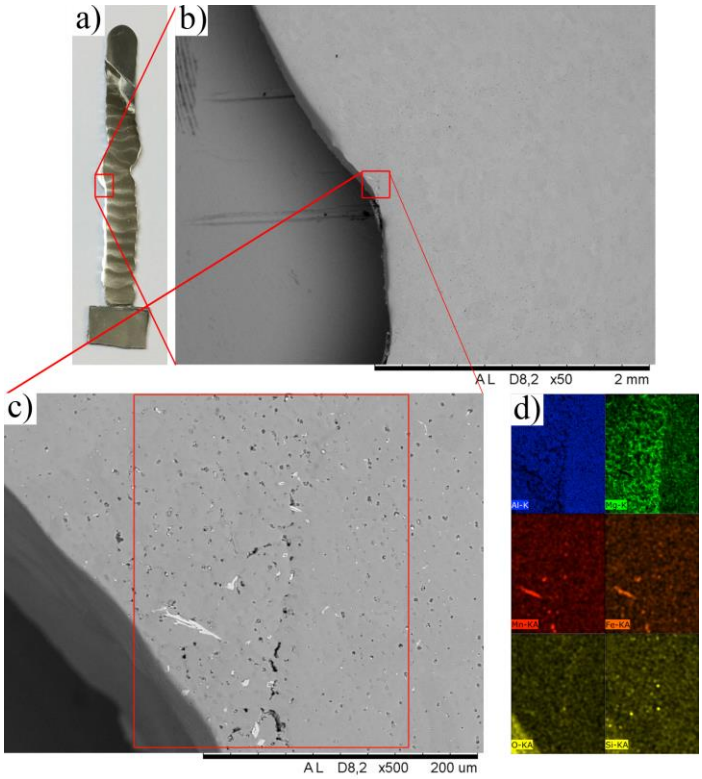


Figure 4.38: A weld bead interface. A) shows the area on the wall. B) show the bead interface below the bump, where a fracture is observed along with needle-shaped intermetallic particles. The image in d) are the elemental maps of Al (blue), Mg (green), Mn (red), Fe (orange), O (yellow) and Si (yellow). The maps suggests that the particles consists of Mn and Fe, mainly.

Another interface is found close to the overexposed area of the electro-polished sample. The interface is recognized by the small depression along the edge (figure 4.39a), and by the small fracture seen in figure 4.39b, which is approximately 600µm long and stretches ≈220µm into the samples lateral direction. The fracture is, therefore, very similar to the one observe in figure 4.38. Because of the overexposure to the electrolyte from the electro-polishing, the interface has been slightly etched. This revealed a network of dendrites. The dendrites above- and below the interface has differing structure. Above the interface, the dendrites have "tree"-like shapes, as if they were laying down on the surface. Below the surface, the dendrites have "rosette"-like structures, as if the "trees" were seen from above. These differences are best observed in figure 4.40 and is due to the direction the weld bead was deposited. Because the images are cross sections, the weld direction is towards and away from the reader. That is, where the rosettes are observed in figure 4.40, the weld bead has been deposited towards the reader. The laying "trees" is then occurring because of material deposition away from the reader. In between these two differing networks, i.e. at the very interface, the dendrites are slightly deformed and do not seem to have any fixed shape. Accumulation of intermetallic particles is also observed by the brighter contrast specs that appear on the surface. Although they are more randomly distributed than in the previous interface, they seem to be situated close to the interface.

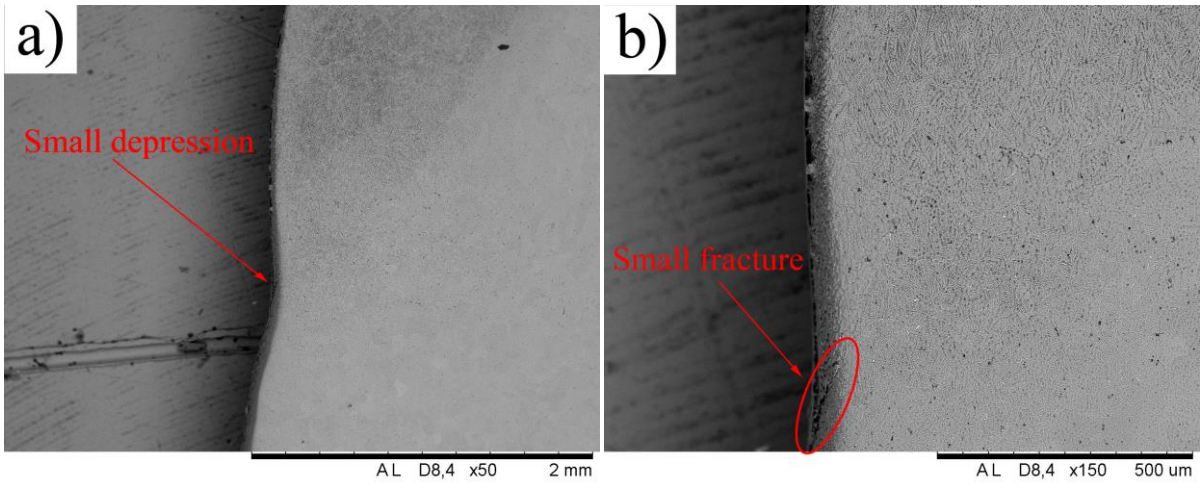


Figure 4.39: a) An image showing a small depression along the edge of the sample. This is an indication of a weld bead interface. b) An image of a small fracture at the edge. This is another indication of an interface.

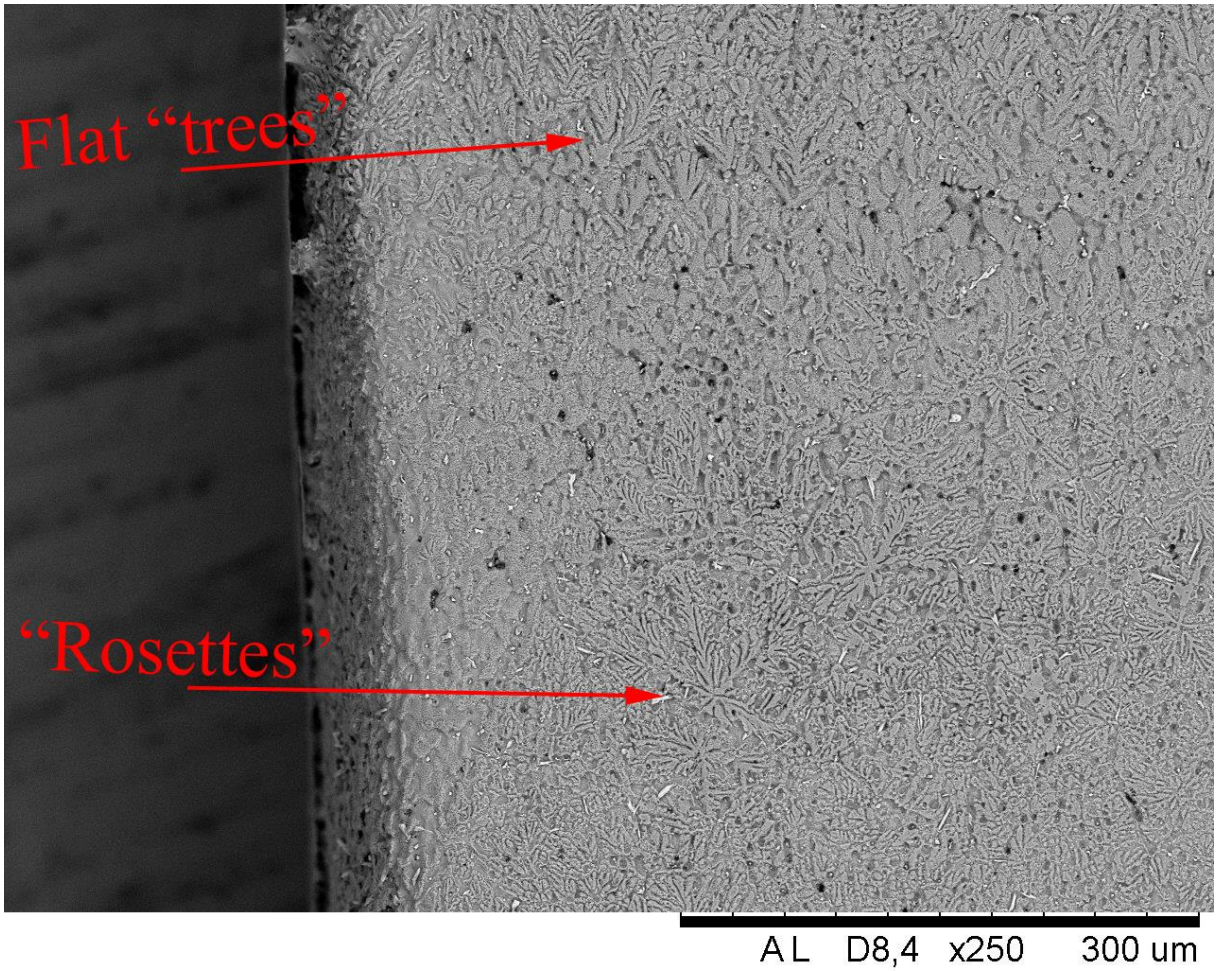


Figure 4.40: An image displaying the different dendrite structures above and below a weld bead boundary. The dendrites have rosette-like structures below the interface. Above the interface, the dendrites are seen as trees laying down flat. This is due to the deposition direction. The majority of the intermetallic particles are collected in between these different dendrite shapes, which is at the weld bead interface.

A third interface was investigated. Contrary to observing the cross section, this interface was examined seen from the side. That is, the sample wall was grinded from one of the sides, polished and investigated. The grinding and polishing was halted when a part of the former edge still was visible at the surface. Doing this was beneficial because it provided insights into the polished interface, and into the untreated surface. This is better understood by figure 4.41a, which shows the result of the side-polished sample with an indication (red square) of the investigated area. The notch in the sample revealed lots of needle-shaped intermetallic particles situated at the untreated surface, i.e. the edge of the sample. Similar intermetallic particles are continuously collected a good way in the lateral direction of the sample surface.

The needles get smaller in size in the same lateral direction. This could also be an effect of the polishing, where the sanding paper and polishing cloths cut off the needles. Another possibility is that the needles actually grow inwards and that the observed specs are the ends of the intermetallic particles.

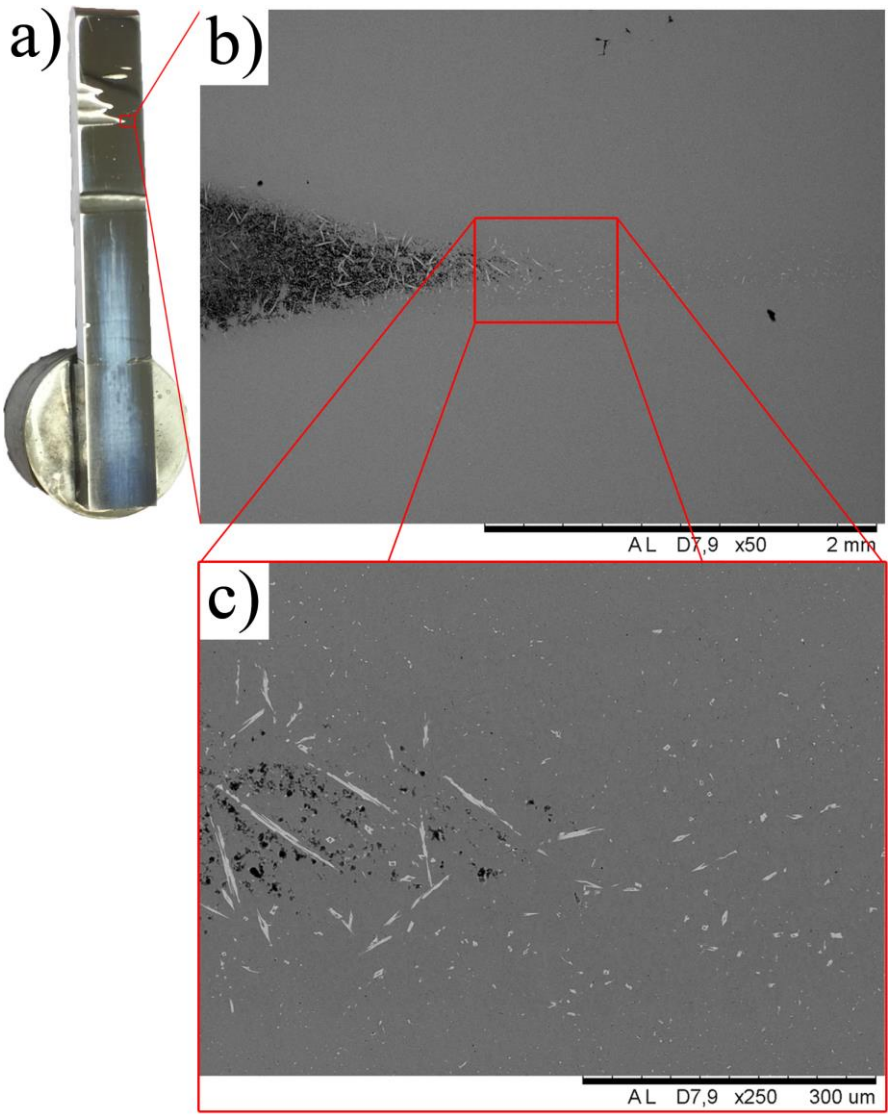


Figure 4.41: Images of: a) the wall grinded down from the side, rather than the cross section. b) The area at the end of a small notch on the wall, which shows a lot of intermetallic particles along the edge of the untreated sample. These intermetallic particles are collected as a layer far in to the samples lateral direction. c) An area at the edge of the untreated sample, which gives a better view of the needle-shaped intermetallic particles.

**Secondary phases**

Accumulation of intermetallic particles in certain areas has been observed all over the sample. Areas that seemed to always have a larger local density of such intermetallic particles, was along the edges of the deposited wall and at the weld bead interfaces. Examples of this were presented in figure: 4.35 (cap layer), 4.36 (center area) and 4.41 (edge). Etching of the sample enhanced the observation of such intermetallic particles, and made it possible to investigate them more thorough. The figure below (figure 4.42) shows the uppermost weld bead boundary between the cap layer and the former. The aluminium dendrites have become very pronounced and the intermetallic particles are nicely situated in between the dendrites and their arms. The images in figure 4.42a and b) shows such an area with large needle-shaped intermetallic particles. Figure 4.42 displays the elemental EDS maps. These show that the needles are composed of aluminium, manganese, iron and silicon. Small amounts of magnesium could also be included. The elemental map of titanium shows a few specs, which do not seem to have a close relation with the needles. From the literature such needle-shaped intermetallic particles in aluminium, composed by the mentioned elements, could be an $Al_6$(Mn,Fe)-phase. This phase is a common phase in many aluminium alloys with the alloying elements AA5083 has (table 2.2). [37, 38]

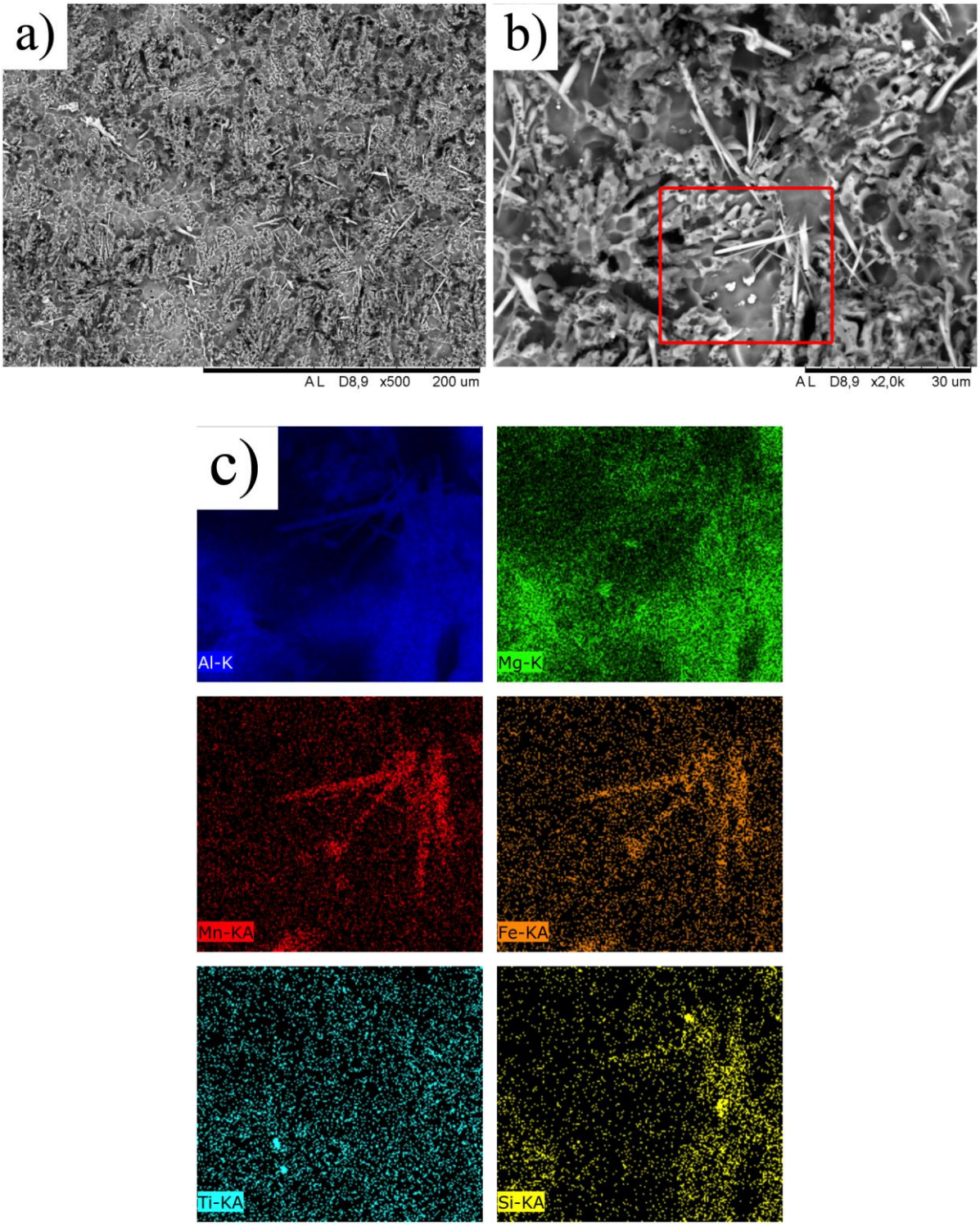


Figure 4.42: Images of accumulated intermetallic particles between the deposited weld beads. A) shows the interface in which many such particles can be seen. B) shows a magnified image of the needle-shaped particles and c) shows the elemental maps of Al (blue), Mg (green), Mn (red), Fe (orange), Ti (cyan) and Si (yellow). The maps show that the particles consists of aluminium, manganese, iron and small amounts of silicon and magnesium in certain areas.

A TEM analysis was performed on a few such intermetallic particles. The analysis included SAD, EDS and STEM-EDS. The result of the first investigated precipitate is presented in figure 4.43 below. Figure 4.43a show that the precipitate is made out of several crystals, which is determined from the changing contrast. The length across the complete precipitate was ≈850nm at the longest and ≈600 at the shortest. These crystals could be of the same composition, growing in different directions, or they could be of differing composition. Another observation is what looks like small particles surrounding the sample. These stems from the FIB sample preparation, proved by the STEM-EDS maps in figure 4.49. The red circle in the image indicates the area of both SAD- and EDS-acquisition. The DP in figure 4.43b is acquired with a [001] zone axis. The 90° angle between the 200- and 020-reflection, suggests a cubic crystal. Furthermore, the reflection positioned at 45° from the 002 is the 110-reflection. The 110-reflection is forbidden in the face-centered cubic (FCC) structure, which leaves the body-centered cubic (BCC) as the best option. The distance between the central spot (000) and 200 was measured in order to calculate the lattice parameter. This value was found to be a≈12.68Å. The EDS analysis showed that the precipitate consisted of 70.90at% aluminium, 17.46at% iron, 10.10at% manganese and 1.54at% silicon. These results are presented in figure 4.44 and table 4.10. A possible phase had a BCC structure with a lattice parameter of a≈12.68Å was a $Co_3Nb_4Si_7$-type structure. This led to an $Al_{19}Fe_4MnSi_2$-type phase. The ratio between the elements was not consistent with the quantification in table 4.10. On the basis of this, a diffraction pattern was simulated in order to create a unit cell similar to the experimental data. The best fit obtained is presented in figure 4.43c and the associated simulated unit cell in figure 4.43d. Both are oriented to be viewed down the [001] zone axis, similar to the DP in a) The $Al_{19}Fe_4MnSi_2$-type phase in aluminium alloys has previously been reported [39, 40].

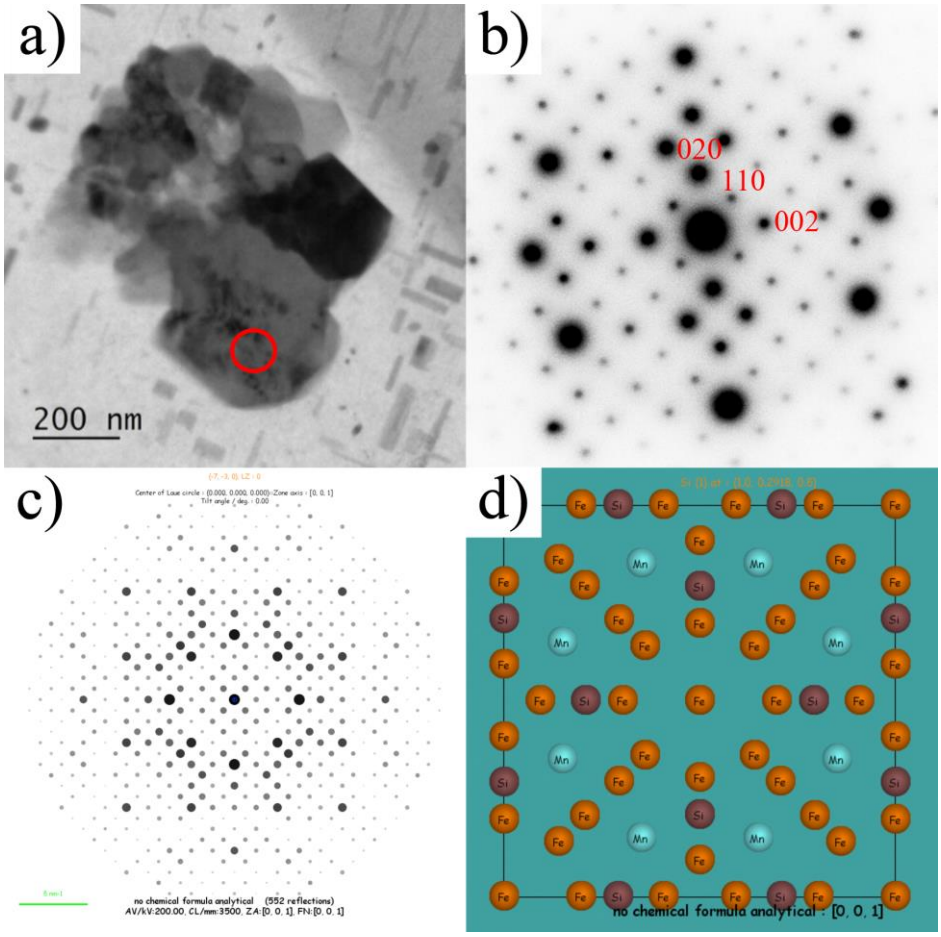


Figure 4.43: The $Al_{19}Fe_4MnSi_2$-type phase. a) Shows the precipitate, which consists of several crystals in different orientations. b) Shows the collected DP of the [001] zone axis. The lattice constant was estimated to a≈12.68Å. c) An image of the simulated DP after optimization. A lot of the symmetry is reproduced. d) An image of the simulated unit cell of the phase belonging to the DP in c).

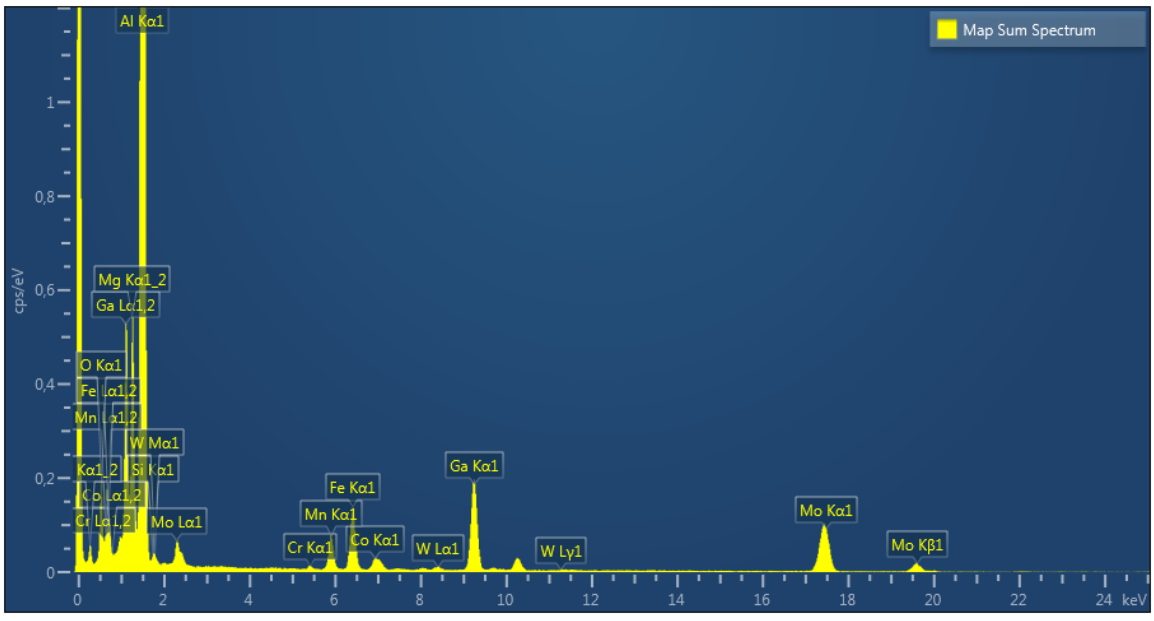


Figure 4.44: EDS spectrum collected at the precipitate. It shows a strong signal from Al, Mg, Si, Fe and Mn. The Ga peak stems from the FIB.

**Table 4.10 – Quantification of the spectrum in figure 4.44:**

| Element: | Wt% | At% |
|---|---|---|
| O | 2 | 5 |
| Mg | 5 | 6 |
| Al | 67 | 79 |
| Si | 0.1 | 0.1 |
| Cr | 0.1 | 0.1 |
| Mn | 2 | 1 |
| Fe | 2.5 | 1 |
| Co | 0.4 | 0.2 |
| Ga | 5.5 | 2.5 |
| Mo | 15 | 5 |
| W | 0.5 | 0.1 |

The second precipitate that was analysed is shown in figure 4.45a. It is larger than the previous shown in figure 4.43a. As with the previous precipitate, it is composed by several crystals. The uppermost part, which was analysed with SAD, had an area of ≈1.3μm$^2$ and the length across ≈1.5μm. The associated DP is displayed in figure 4.45b, where the measured lattice constant was ≈14.4Å. This lattice constant accompanied by the EDS results in figure 4.46 and the quantification in table 4.11, led to a good agreement with an $Al_{18}Mg_3Mn_2$-phase with a FCC-structure.

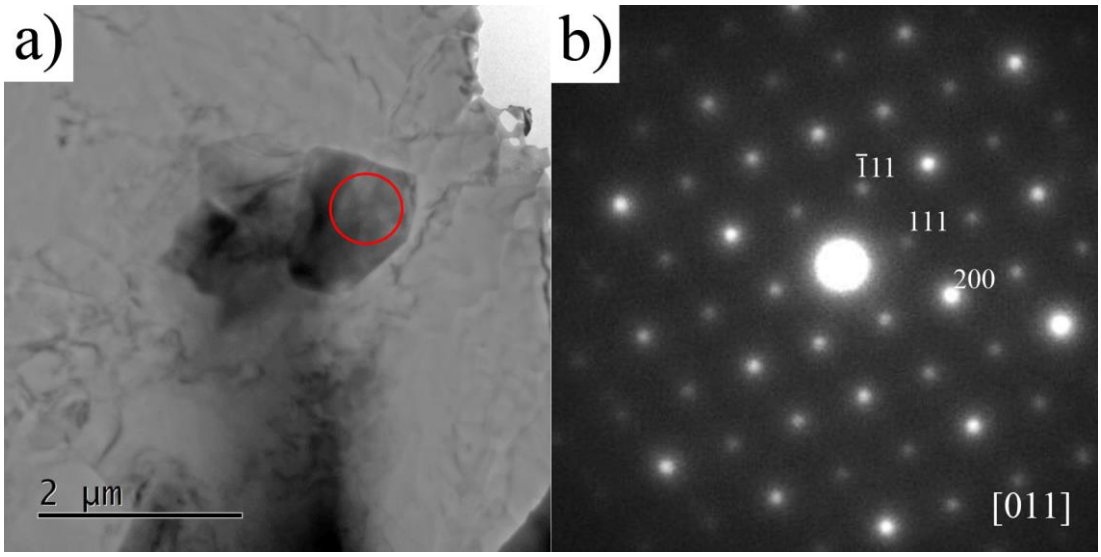


Figure 4.45: Image of: a) the precipitate under investigation. As with the former precipitate it is composed by several crystals that has grown in to one. b) The associated DP from the area indicated in a). It has a lattice constant a≈14.4Å, which is in good agreement with an $Al_{18}Mg_3Mn_2$-phase.

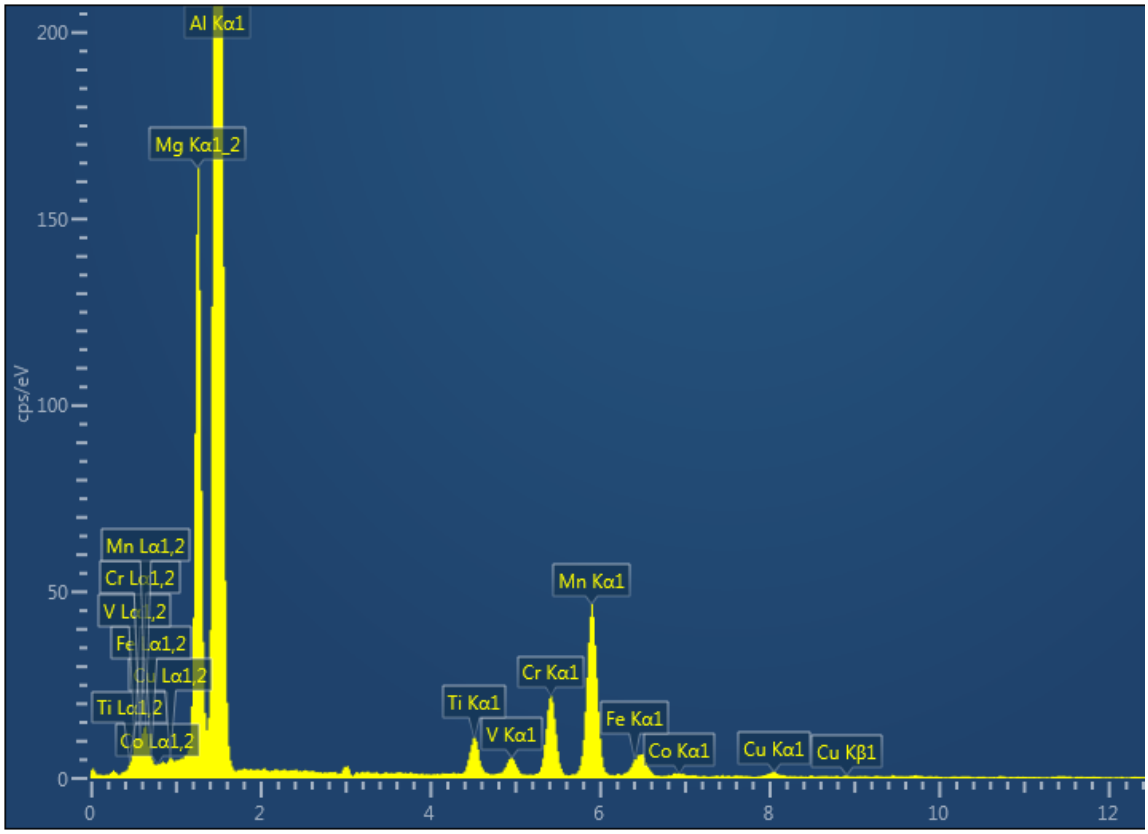


Figure 4.46: EDS spectrum of the selected area in figure 4.45.

**Table 4.11 – Quantification of the spectrum in figure 4.46:**

| Element: | Wt% | At% |
|---|---|---|
| Mg | 13 | 15 |
| Al | 74 | 78 |
| Ti | 1 | 0.5 |
| V | 0.5 | 0.1 |
| Cr | 3 | 2 |
| Mn | 7 | 4 |
| Fe | 0.5 | 0.2 |
| Co | 0.2 | 0.1 |
| Cu | 0.2 | 0.1 |

A STEM-EDS acquisition was performed on another intermetallic particle on the FIB sample and is shown in figure 4.47 below. It is larger than the other intermetallic particle on the same sample (figure 4.43). It measures just over 1µm at its longest point. The elemental EDS maps show that the particle is composed of the same elements as the first in figure 4.43. That is, mainly aluminium, iron, manganese and silicon. The particle is surrounded of what looks like a lot of crystals, as with the precipitate in figure 4.43. The elemental maps show that these crystal-like shapes are gallium, which is deposited by the FIB. Such gallium particles were not observed in the same amount any other places on the sample. They seemed to be heavily collected around the intermetallic particles on the sample. Gallium was also detected at the grain boundaries of aluminium, but not as much. Examples of this can be seen in appendix A-3, figure A.6.

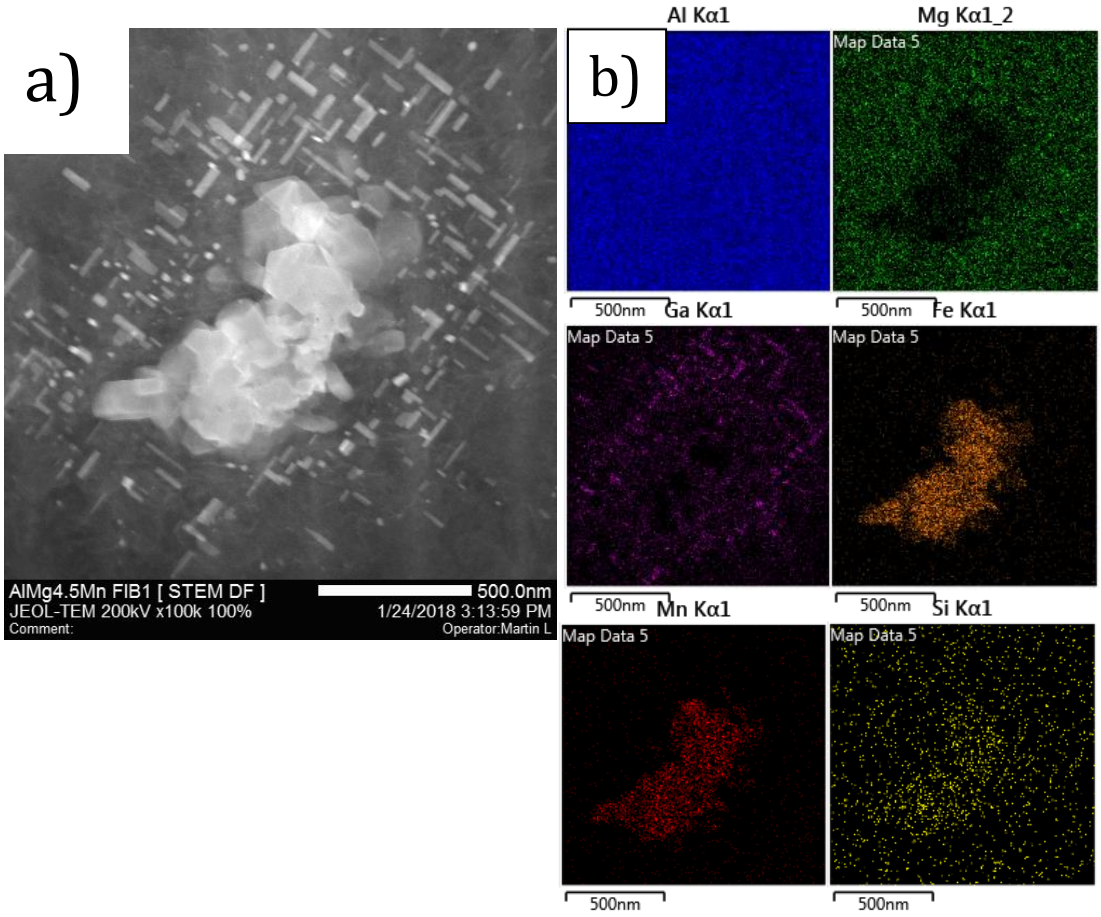


Figure 4.47: A STEM acquisition of a intermetallic particle. A) show the particle surrounded by Ga crystals. B) shows the elemental maps, which reveal that the particle consists of Al, Mn, Fe and small amounts of Si. The Ga-map shows that the crystals surrounding the particle is in fact Ga.

Another STEM-EDS acquisition was performed on a more remote particle, it is seen in figure 4.48. The EDS maps and quantification showed that this particle mainly consisted of silicon and oxygen. This is an observation that has been made in several of the SEM-EDS acquisitions, where silicon either is connected to the manganese- and iron constituent or aside from these and in connection with oxygen. The particle in figure 4.50 shows a nearly circular particle composed by silicon [5at%] and oxygen [12at%] in a ratio resemblant to silicon dioxide ($SiO_2$).

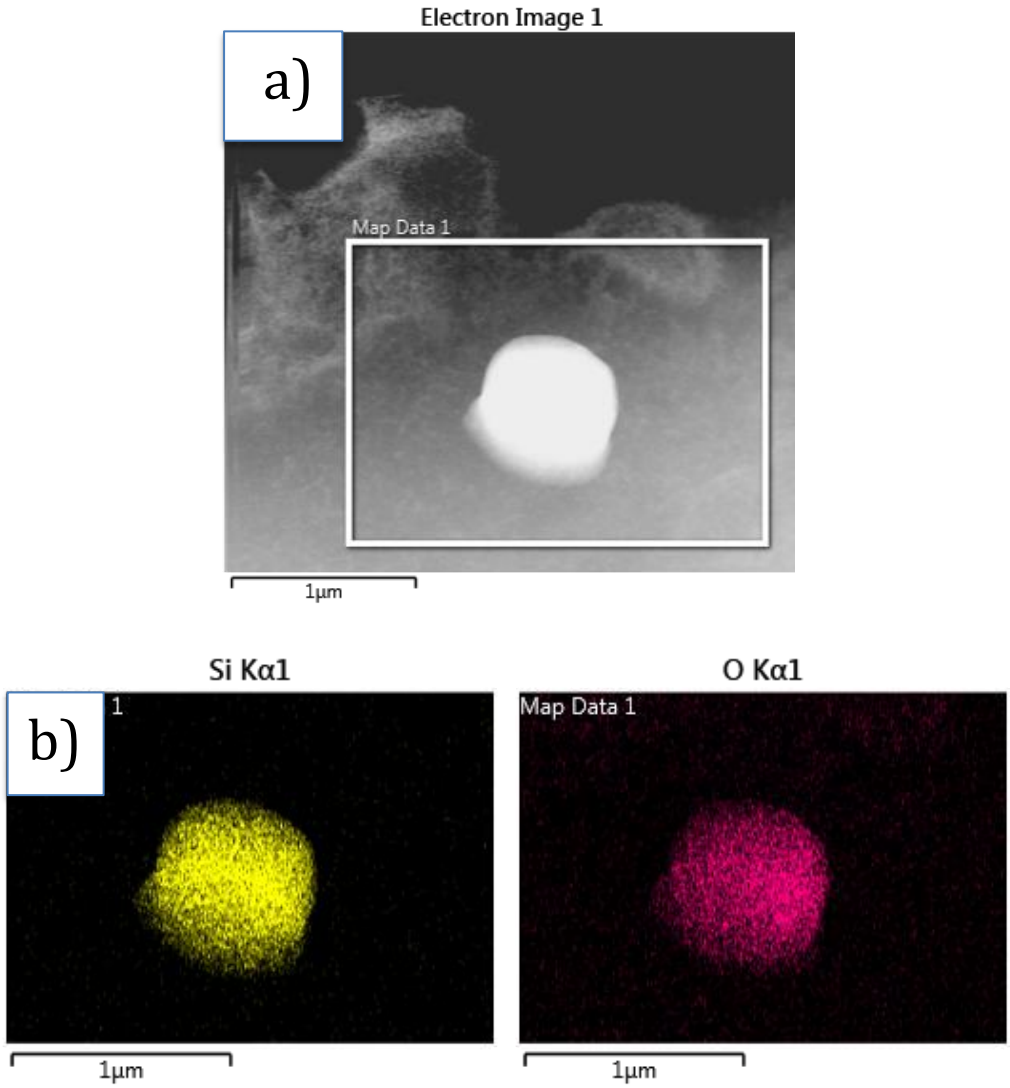


Figure 4.8: A STEM acquisition of a circular particle. A) show an image of the particle and b) shows the elemental maps of silicon (yellow) and oxygen (pink). The suggested phase based on a quantification is $SiO_2$

### 4.4 Homogenised sample AA5083_S4

After homogenisation the untreated sample surface changed to a golden colour and the HAZ became visible. The images in figure 4.49 shows the two samples right after the heat treatment. The image in a) shows how the colour of the surface changed to golden in reflection with light. The image in b) shows how the HAZ became visible after the heat treatment.

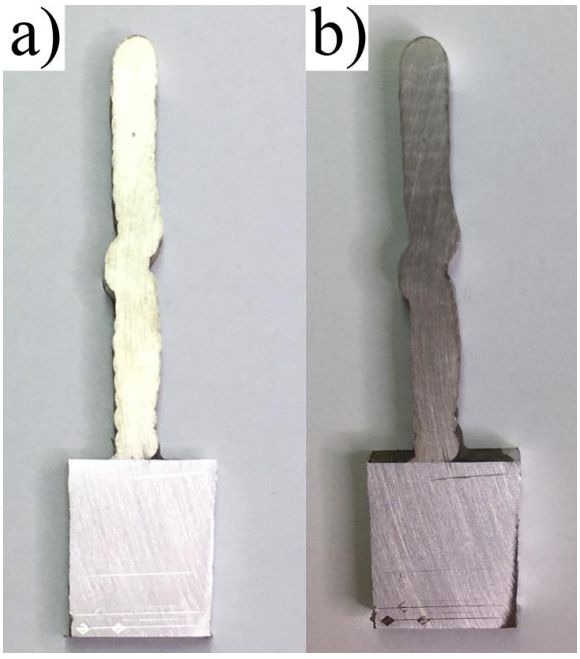


Figure 4.49: Images of the heat-treated sample wall. The image in a) shows the golden colour it got after the treatment. The image in b) shows how the HAZ became visible.

### 4.4.1 Microstructure of sample AA5083_S4

#### Center area

By intent, the sample was heat treated in order to even out the irregular magnesium distribution that were observed in figure 4.36 and figure 4.37. The result is seen in figure 4.50 below. They are acquired from a similar region on the sample cross-section surface as the ones in 4.36 and 4.37. And as the maps and the layered image shows, the magnesium content has been evened out. Intermetallic particles are still observed, and seem to be of the same size and spread as with the non-heat treated sample. That is, intermetallic particles of manganese, iron, manganese-and-iron, and the more independent silicon intermetallic particles.

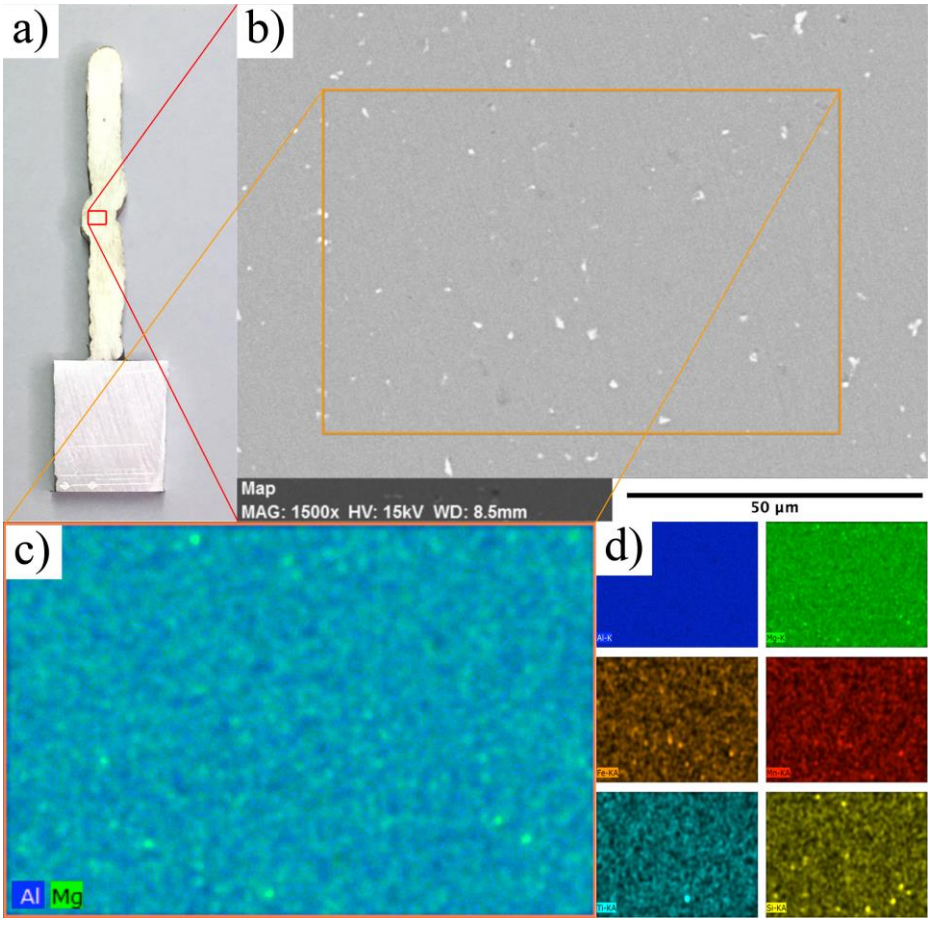


Figure 4.50: a) The heat-treated sample with an indication of the analysed area. b) The area selected for EDS-analysis with a similar amount of intermetallic particles as the area in figure 4.36 and 4.37. c) A layered image composed of Al and Mg. It shows how the former uneven magnesium distribution has been evened out. d) Elemental EDS-maps, which show the same effect as in c) by the Al and Mg maps. The maps of: Fe, Mn, O and Si shows precipitation.

Several quantitative analyses were performed in order to anticipate the effect of homogenisation in numbers. Two different oriented grains were selected for the analyses. Figure 4.51 below shows the circular areas that were selected for the quantification. The corresponding table of quantification is shown below (table 4.12). The result was almost an insignificant difference between the selected spots and the selected grains.

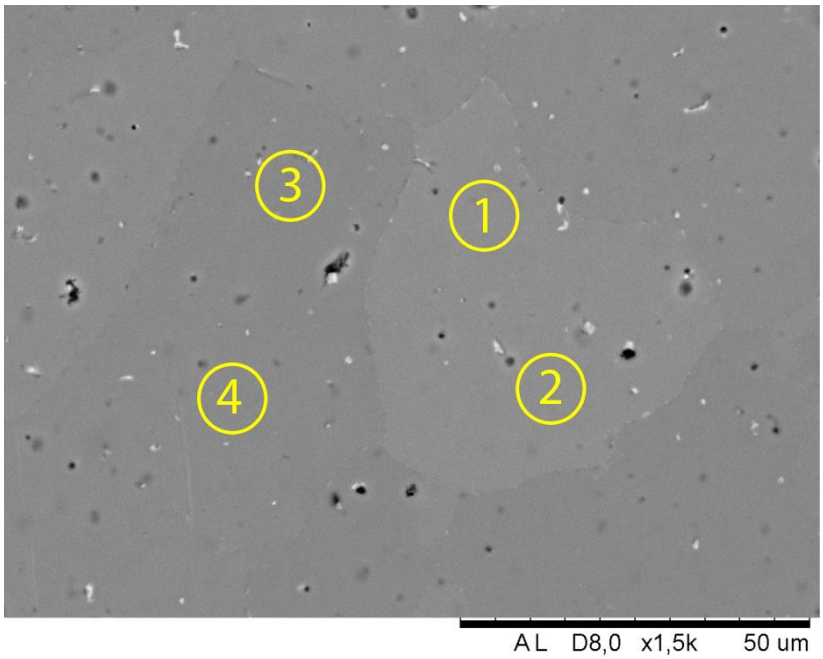


Figure 4.51: Image of the selected grains for quantitative spot analyses along with numbered, circular markings of the spots that were quantified.

**Table 4.12 – Table of quantification at the four spots divided on the two separate grains, G1 and G2:**

| **Element:** | **Al [at% ±4.7]** | **Mg [at% ± 0.3]** | **Mn[at% ± 0.1]** |
|---|---|---|---|
| **Spot 1_G1:** | 93 | 6 | 1 |
| **Spot 2_G1:** | 93 | 6 | 1 |
| **Spot 3_G2:** | 93 | 6 | 1 |
| **Spot 4_G2:** | 94 | 5 | 1 |

### Weld bead interfaces

Several of the same (same as the non-homogenised sample) weld bead interfaces were chosen for the investigation. The figure below shows the same area as figure 4.38. And as with the non-homogenised sample, similar needle-shaped intermetallic particles are observed. Contrary to the non-homogenised sample, the grain structure became more visible. This enabled observation of how the intermetallic particles are situated in relation to the grains. Figure 4.52 shows, many intermetallic particles are in close relation to the grain boundaries. The observed intermetallic particles have similar shapes and sizes as the former observations. It is therefore assumed, with some confident, that they are of the same phase as suggested by figure 4.42, i.e. $Al_6(Mn,Fe)$ One can also observe that there are a few holes at some of these boundaries, which is very likely to be a result of intermetallic particles that has fallen out during sample preparation.

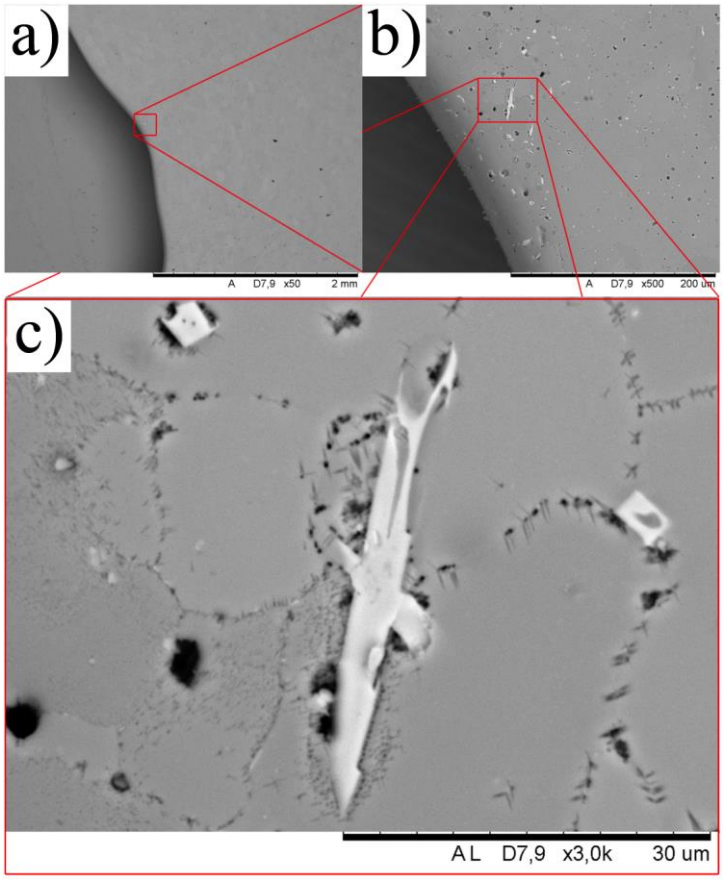


Figure 4.52: An area on the heat-treated sample, similar to the area in figure 4.38. The Grains has become more visible after heat-treatment and needle-shaped intermetallic particles are sticking out of the surface, positioned close to the grain boundaries of aluminium.

The same area as in figure 4.54 was investigated after etching. The surface showed dendritic aluminium structure with intermetallic particles situated in between the dendrite arms. The weld bead interface is recognized by the curved fracture that starts at the edge and ends ≈1000µm in to the sample and the shape of the dendrites. As seen in the images in figure 4.55a) and b), the dendrites looks like rosettes below -and as trees laying down above the weld bead boundary. The observations are similar to the observations on the non-heat-treated sample AA5083_S3 in figure 4.39 and 4.40, where both the fracture and the changing dendritic structure are observed. The images in figure 4.55a) shows the interface, where the fracture is indicated by the arrow and the red line. In between the two blue lines, there is a layer with higher concentration of intermetallic particles.

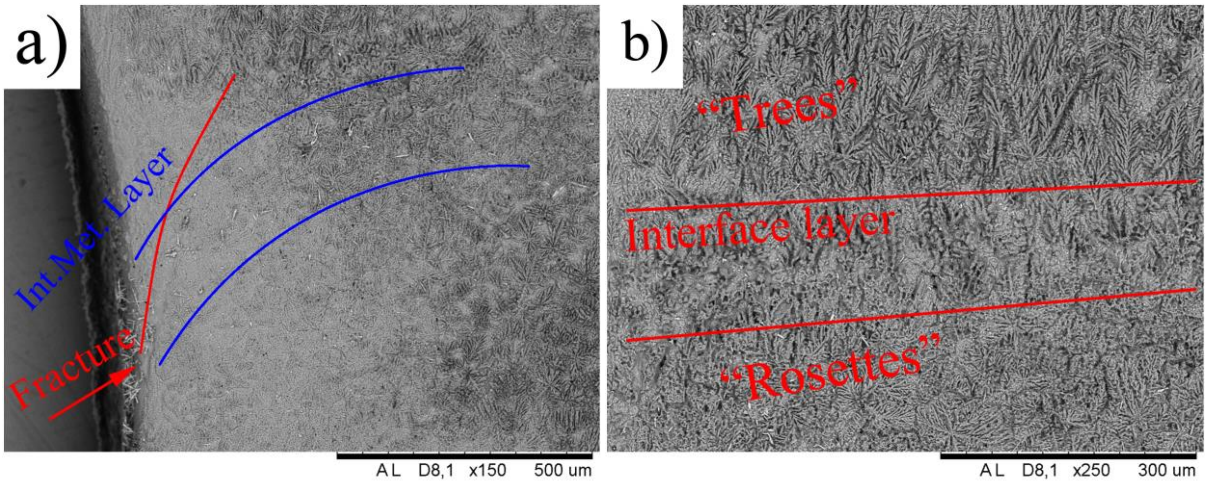


Figure 4.55: BSE images of the weld bead boundary indicated in figure 4.54. The image in a) shows the recognizable fracture and a layer with higher concentration of intermetallic particles in. And the image in b) shows the dendritic structure similar to trees laying down above- and to rosettes below the interface.

# 5 Discussion

## 5.1 Comparison of Shape, Size and Amount of Post-Processing Need

The first sample AA4020_S1 turned out relatively straight, with fairly even edges. As previously mentioned, the products made by this method of AM are near-net shape, which means that post-processing by e.g. CNC machining is necessary. With that in mind, the result of the product turned out within the limits of expectation. The second sample AA4020_S2 had a sinuous shape, with an average width over the sample of 1.283cm, however only a fraction of this is machinable in to a straight wall. It has been estimated that a finished wall section cut out of this deposited wall will at maximum have a width of 0.25cm, because of all the bends. The third sample AA5083_S3 had a much straighter shape and is by far the closest to the intended 3D model. It is ≈5.4cm tall and has an average width of ≈0.5cm, but the bend mid-way up the wall results in an approximate width of maximum 0.4cm after machining. The two latter samples, S2 and S3, are both made by the same equipment and with similar welding parameters. It is safe to say that the S2 sample has been supplied with too much heat, which has made it “sag” during deposition. However, the selected parameters for deposition of the two walls, AA4020_S2 and AA5083_S3, seem to be close to the optimum for the latter wall, with regards to the shape and amount of post-processing necessary.

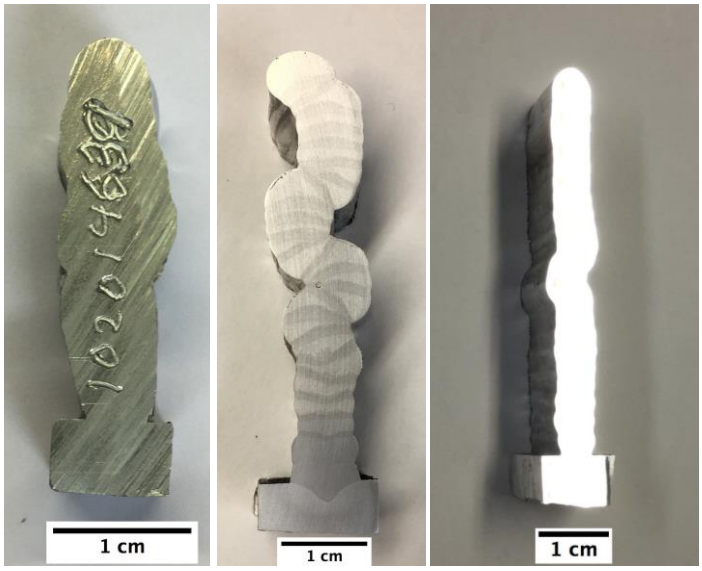


Figure 5.1: Cross section images of, a) the wall AA4020_S1, b) the wall AA4020_S2 and c) the wallAA5083_S3. Large differences with regards to shape are observed. The AA4020_S1- and AA5083_S3-wall has the best matching shape to the modelled structures.

## 5.2 Microstructure considerations

The sample AA4020_S1 showed a much layered structure with regards to the silicon rich and silicon poor, HAZ, areas. Fewer investigations were performed on the AA4020_S2 sample because of the bad build quality, with regards to the shape. However, the AA4020_S2 sample show similar contrast changes in reflection with light as the AA4020_S1 sample, which is seen in the figures 4.2b (AA4020_S1) and figure 5.1 (AA4020_S2) above. These reflections indicate that there are similarities at the microstructural level as well. The sample AA4020_S1 had areas with lot of dendrites which consisted of silicon. These layered areas were generally harder than those with less silicon

The sample AA5083_S3 showed promising results with regards to size and shape, but one of the first observations made at the microstructural level was that the weld bead interfaces were easily observed by fractures. The observable length of the curved fracture in figure 4.10 is approximately 600µm. Its length in the lateral direction of the sample is approximately 300µm. Such fractures are signs of poor fusion between the weld beads. One can imagine that the molten material of a subsequent layer runs down along the curved cap-layer and solidifies, rather than melting the former layer and

merge together with it. There could be several reasons for this behaviour, where the most obvious is too little heat transfer during deposition.

Another reason could be because of «slag», which consists of carbon deposits from the atmosphere. Slag-formation has a detrimental effect on weld seams because it deposits as a layer at the surface, which raises the melting temperature of the previous layer, and thus, causing a lack of fusion. The images of figure 4.33 show the interface between the first weld bead and the base material and from the elemental carbon map in figure 4.33b) one can observe pores that contain carbon. As mentioned, this observation could very well be due to the sample preparation, where diamond particles get trapped, but it could also be slag-formation. The suggestions of poor fusion are reflected in the tensile tests, where the difference between the horizontal and vertical direction test samples is tremendous. These observations can be reviewed in figure 5.4 below.

## 5.3 Mechanical properties

### 5.3.1 Tensile Test Properties

The tensile properties of the AA4020_S1 sample showed similar properties in both the horizontal- and vertical direction of the sample (ref. fig. 4.4). This is a sign of good fusion. The vertical direction tensile samples cross each of the weld beads and thus, they are the most prone to break if lack-of-fusion is present. If a comparison with the mechanical properties of the initial wrought alloy is made, the sample shows similar strength values. However, the samples that were prepared were 10mm long, whilst the provided reference values were for samples of 100mm length; therefore, they are not directly comparable. The reason for the length difference is due to the height of the sample, which was no more than ≈30-, ≈50- and 55mm at max for the three samples AA4020_S1, AA4020_S2 and A5083_S3, respectively. A supervisor consultation (A. S. Azar, 2018) explained that the result of the length difference is an expected decrease in the tensile- and yield strengths as well as the strain values, because of more material-contribution to even out the applied force. Also, the total elongation of the samples was not measured and only the strain at maximum force was reported. Nevertheless, the measured values provide an indication of the strength, which was within the range of the reference values. The yield strength of the three samples was 61-, 54- and 61MPa for V1, V2 and H1, respectively. The reference value is ≥50MPa. The Tensile strength values were 161-, 153- and 166Mpa, for the samples in the same order. The reference value is ≥120MPa. This makes the yield- and tensile strengths well above the minimum tolerance. The strain values at maximum load were measured to 16.6-, 15.6- and 14.2% for the three samples in the order V1, V2, H1, respectively. The reference value is ≥25%, which makes the strain quite a lot poorer than the reference. This could be an effect of the different testing conditions, i.e. the lengths of the samples, or because of macro- and/or microscopic effects, such as porosity or an uneven distribution of the intermetallic particles and phases. Table 5.1 shows the comparison of the tensile tests of the sample AA4020_S1 with the reference values of wrought AA4020.

**Table 5.1 – Comparison to reference of tensile test samples of wall AA4020_S1:**

| | **S1_V1:** | **S1_V2:** | **S1_H1:** | **Reference:** |
|---|---|---|---|---|
| Yield strength $R_{p0.2}$ [MPa]: | 61 | 54 | 61 | ≥50 |
| Tensile strength $R_m$ [MPa]: | 161 | 153 | 166 | ≥120 |
| Strain at max. load [%]: | 16.6 | 15.6 | 14.2 | ≥25 |

The tensile tests of the AA4020_S2 sample showed a slightly higher yield- and tensile strengths in the vertical direction of the sample. The measured yield strengths in the horizontal direction were 82.7-, 82.7- and 97.2MPa. In the vertical direction the yield strengths were 119.5-, 88.3-, 80.7- and 97.5MPa. Compared to the reference value (≥50), these strengths are well above the minimum-tolerance. The tensile strengths in the horizontal direction of the wall were measured to 183.13-, 181.84 and 190.35MPa and in the vertical direction 191.1-, 172.5-, 189.8 and 180.0MPa. The values in the two directions are also well above the reference value of ≥120MPa. The strain values show very close response to the reference values in both the horizontal- and the vertical direction. The measured values were 25.2-, 24.1-, 23.8-, 25.8-, 28.2- and 24.5% strain at maximum load and the reference value is ≥25% strain at maximum load. With all of the above taken in to account, the wall of AA4020_S2 shows a very good sign of fusion. Often is lack of fusion caused by too little heat transfer during deposition. Poor mechanical would reflect these properties, especially in the vertical direction, where the weld beads have been crossed in order to extract the tensile sample. As stated before the structure of AA4002_S2 does not seem to have been too cold during deposition, but rather the opposite.

The mechanical tensile properties reflect the statement of good fusion and more than sufficient amounts of heat transferred during deposition. The comparison of the measured values to the reference is listed in table 5.2 below.

**Table 5.2 – Comparison to reference of tensile test samples of wall AA4020_S2:**

| | **S2_H1:** | **S2_H2:** | **S2_H3:** | **S2_V1:** | **S2_V2:** | **S2_V3:** | **Reference:** |
|---|---|---|---|---|---|---|---|
| Yield strength | 82.7 | 82.7 | 97.2 | 119.5 | 88.3 | 97.5 | ≥50 |

| | | | | | | | |
|---|---|---|---|---|---|---|---|
| $R_{p0.2}$[MPa]: | | | | | | | |
| Tensile strength $R_m$ [MPa]: | 183.13 | 181.84 | 190.35 | 191.1 | 189.8 | 189 | ≥120 |
| Strain at max. load [%]: | 25.2 | 24.1 | 23.8 | 25.5 | 28.2 | 24.5 | ≥25 |
| Elongation compared to reference: | +1% | -4% | -5% | 3% | 11% | -2% | 0 |

The mechanical tensile tests of the wall AA5083_S3, showed promising results in the horizontal direction. However, the vertical direction did not have properties that reflected one of the main properties of the alloy, i.e. strength. The measured yield strength values of the horizontal direction were 145.8-, 144.0- and 143.0MPa and the vertical values were 149.0-, 152.0- and 147.5MPa. All of these values are above the reference value of ≥125MPa. The tensile strength also shows a promising trend, where the measured values were 310.0-, 309.8- and 310.4MPa in the horizontal direction, and 264.5-, 216.3- and 249.5MPa in the vertical direction. Compared to the reference value of ≥300, these values are not too bad. The vertical direction has a lower strength, which is very likely to be a consequence of poor fusion between the welds. It is when the strain values are evaluated that the major differences to the reference value are observed. The measured strain values were 38.2-, 36.8- and 44.9% in the horizontal direction, and in the vertical direction 10.1-, 2.1- and 2.1%. The reference value is ≥25%, which means that the horizontal test samples are sufficiently above the minimum limit, whilst the vertical samples are far below. There are several possibilities for this to occur. One is porosity; another is slag formation between the welds. It could also be due to precipitation of intermetallic phases between the welds during solidification.

It is, however, a great possibility that these values would have been different if the deposition parameters were optimized. The comparison of the measured values to the reference is listed in table 5.3 below, where the measured elongation compared to the reference value is included. These values show the deviation in percent and reflect the observations of the graphs in figure 4.29, where the vertical-direction samples showed high strength, but fracture after a very short elongation.

**Table 5.3 – Comparison to reference of tensile test samples of wall AA5083_S3:**

| | **S3_H1** | **S3_H2** | **S3_H3** | **S3_V1** | **S3_V2** | **S3_V3** | **Reference** |
|---|---|---|---|---|---|---|---|
| Yield strength $R_{p0.2}$[MPa]: | 145,8 | 144.0 | 143.0 | 149.0 | 152.0 | 147,5 | ≥125 |
| Tensile strength $R_m$ [MPa]: | 310.0 | 309,8 | 310,4 | 264,5 | 216,3 | 249,5 | ≥300 |
| Strain at max. load [%]: | 38.2 | 36.8 | 44.9 | 10.1 | 2.1 | 2.1 | ≥25 |
| Elongation compared to reference: | 35% | 32% | 44% | -148% | -1090% | -1090% | 0 |

### 5.2.2 Comparison of Tensile Test Properties

Initially, the AA5083 alloy provides more strength than the AA4020 alloy. That is, the sample AA5083_S3 should have a higher strength than the samples AA4020_S1 and AA4020_S2. The tensile tests prove that it does. However, the strain values make the wall structure of AA5083_S3 less attractive for AM, because it will fracture abruptly when the maximum force is reached. That is, the initial ductility of the material is almost completely lost after deposition of the layers. It is also interesting how the tensile tests of the sample AA4020_S2 have an improved strength over AA4020_S1, although they are of the same alloy. There could be several reasons for this, but the main difference between the two, with regards to manufacturing, is the multiple-axis robot and improved optimization with of the CMT-device.

**Table 5.4 – Comparison of tensile tests of the three samples AA4020_S1, AA4020_S2 and AA5083_S3**

| | S1_H_avg. | S1_V_avg. | S2_H_avg. | S2_V_avg. | S3_H_avg. | S3_V_avg. |
|---|---|---|---|---|---|---|
| Yield strength $R_{p0.2}$[MPa]: | 61 | 57.5 | 87.5 | 101.8 | 144.3 | 149.5 |
| Tensile strength $R_m$ [MPa]: | 166 | 157 | 185.1 | 190.0 | 310.1 | 243.4 |
| Strain at max. load [%]: | 14.2 | 16.1 | 24.4 | 26.1 | 40.0 | 4.8 |

Avg.=average value ±0.1

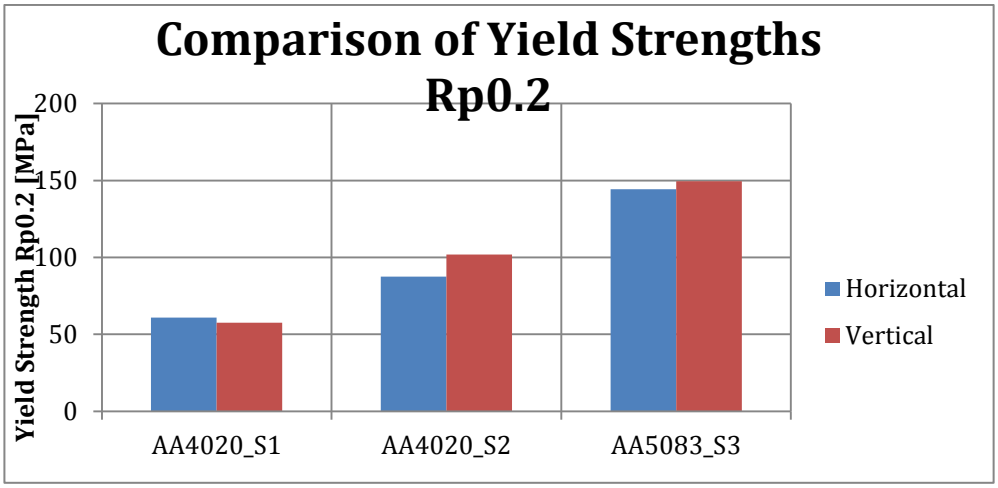


Figure 5.2: compared yield strengths of the three samples.

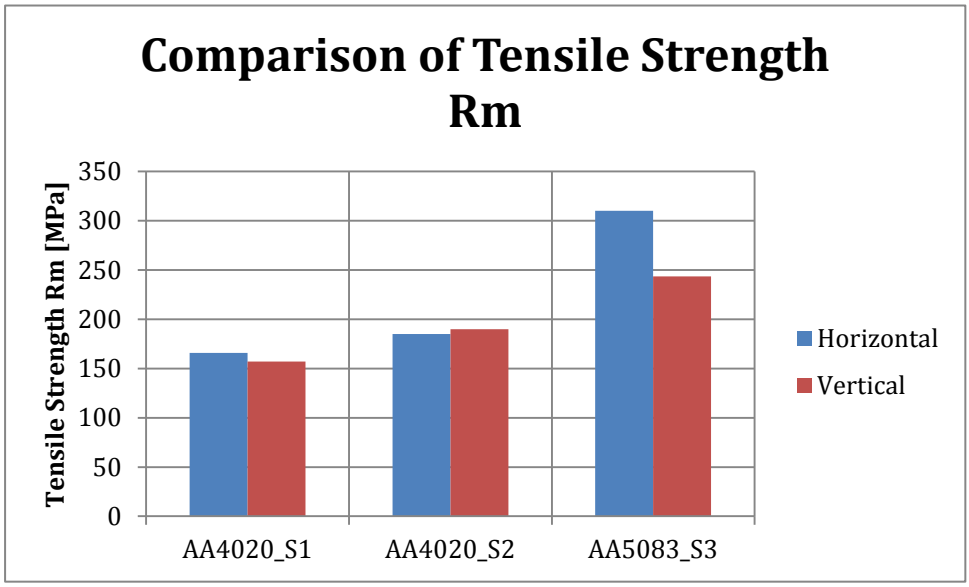


Figure 5.3: compared tensile strength of the three samples.

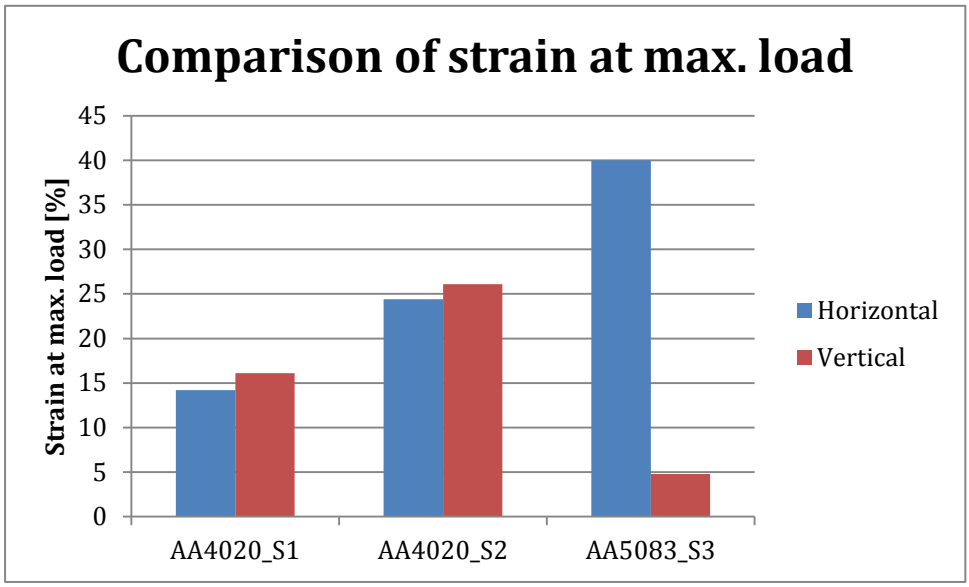


Figure 5.4: compared strain of the three samples.

## 5.3 Compared Hardness and Porosity

No porosity measurements were performed on the first wall, AA4020 S1, but figure 4.4 reveal that there is a lot of porosity.

The second wall AA4020_S2 was measured for porosity. The result was that it was very porous (see figure 4.26 and 4.27), at least compared to the sample AA5083_S3. The pore-density was higher along the edges and at the interfaces between the weld beads. However, this large amount of pores does not seem to be reflected in the tensile tests. One would think that a lot of pores would cause brittleness and fracture at a short elongation, but the tests show that the samples do not seem especially affected by this porosity. The hardness measurements of this sample (AA4020_S2) showed an average hardness of ≈34HVThe sample AA5083_S3 had small amounts of porosity. The measured pores were located mostly along the edges of the sample. In addition a collection of pores were observed at the wall-substrate interface, which could be due to the fast heat dissipation through the cold substrate when the first layer was deposited. These results are reflected in the

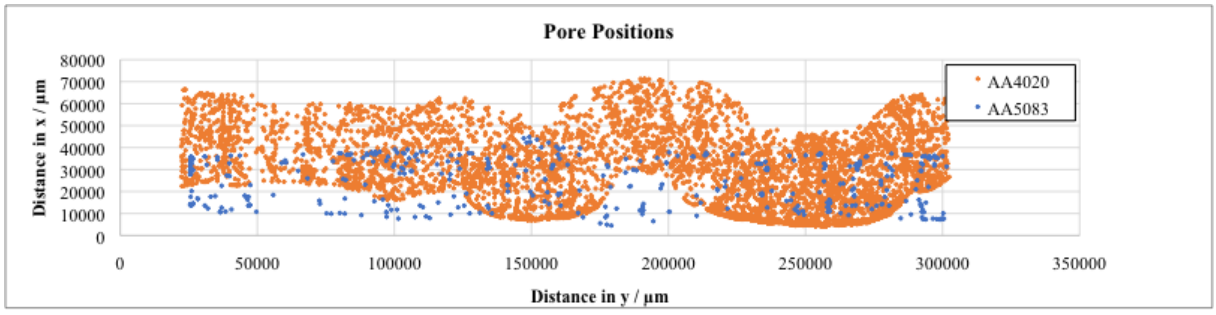


Figure 5.5: A plot of the pore positions in both the AA4020_S2 and the AA5083_S3 samples, which is represented by orange –and blue spots, respectively.

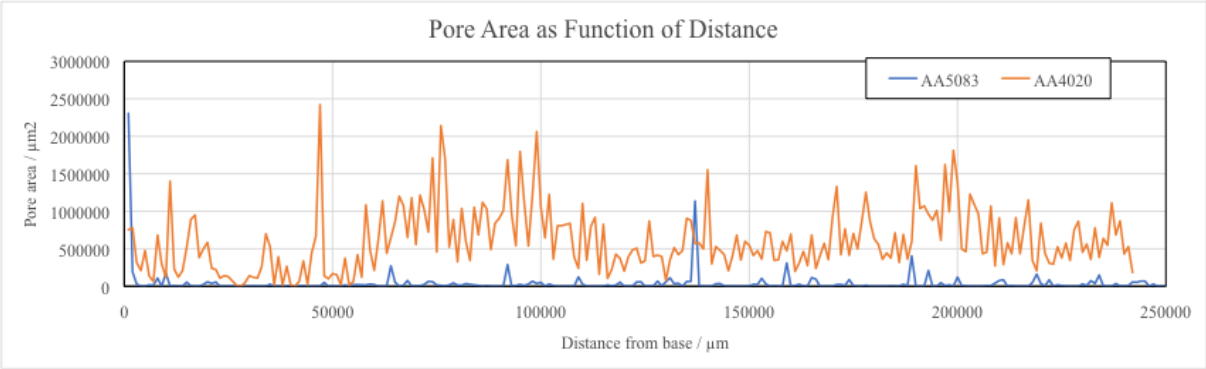


Figure 5.6: Pore area as function of distance from the base of both the AA4020 (S2) –and the AA5083 (S3) sample, denoted as orange and blue curves, respectively


Figure 5.7: Compared hardness measurement graphs, as function of the position, of the AA4020 alloy (blue) and AA5083 alloy (orange). The position of the base plate (of alloy AA5754), first, base, layer and last, cap, layer noted in the graph window, to ease the interpretation. The dashed vertical line indicates the border between the base material and the deposited material.

### 5.1 Compared hardness tests of the AA4020 (S2) and AA5083 (S3) alloys

The results of the hardness tests are easier comparable, because the two samples was produced by the same equipment. Thus, the main differences observed are due to the alloy characteristics. Minor differences could also occur due to the change of processing parameters, but this is as good as unavoidable because of the different weldability of the two alloys. The figure below, figure 5.7, show the compared result of the two alloys. The orange graph shows the result of the AA5083 (S3) alloy, whilst the blue graph shows the AA4020 (S2) alloy. The graph window also shows the border between the base plate of alloy AA5754 and the deposited material, which is indicated by the vertical dashed line at zero y-direction. In addition, the first, base layer, and the last, cap layer, are noted in the figure. The results reveal that the AA5083 alloy generally is harder than the AA4020 alloy.

### 5.2 Compared porosity measurements of the AA4020 and the AA5083 alloy

The porosity of the two alloys was measured as described in section 3.8. The positions of the pores were plotted as a function of the distance on the two cross sectional sample pieces. A very accurate position in both x –and y-direction could be determined, because the measurements were performed on VLM images. The result is shown in figure 5.5. From these position plots, two graphs were constructed, showing the pore area as a function of distance on the sample. This was done to ease the interpretation of the compared porosity. As Figure 5.5 shows, the AA4020 (S2) alloy has a lot more pores, than the AA5083 (S3) alloy, orange versus blue spots, respectively. In fact, there are so many more in the AA4020 that the pores of the AA5083 alloy nearly becomes invisible in the plot. And of course, this is confirmed by the graphs in figure 5.6.

## 5.4 Future work

If more time were granted this project, an attempt on the "Buthanol-method", proposed by C. J. Simonsen et. al. in [41] for analysis and identification of intermetallic particles by dissolution of the aluminium sample would have been peformed. It would be of great interest to identify more of the particles that is situated in the regions prone to break upon application of a load. The identification could then be performed by the use of X-ray Diffraction (XRD), which has not been successful on trials that were performed, but not included in this thesis.

Another great beneficial analysis method for this project would have been electron-backscatter diffraction (EBSD) in the SEM. Several trials of preparing the sample for EBSD have been performed without results. The amount of sample preparation time is reflected in the thesis, but unfortunately the results came too late. The analyses were halted several times due to formation of an amorphous oxide- and deformation layer caused by sample preparation. Aluminium is a soft metal, and every trial on EBSD resulted in lack of diffraction, meaning that no phase identification could be executed. EBSD would be greatly beneficial because the results show the crystallographic orientation of the grains within the structure. Diffraction at certain angles, as with the TEM, makes it possible to identify and locate the intermetallic particles relative to the aluminium matrix. Ideally, most of the phases would have been known from the dissolution (buthanol-method), and thus, making the identification with EBSD- and the location of the particles more accurate. It could also be interesting to examine the dislocations that were observed in figure 4.21 and 4.22 with high resolution STEM, in order to unveil what the origin of the dislocations were (i.e. stacking faults or precipitation).

Tensile tests from the homogenised sample wall AA5083_S4 would also have been beneficial for the project, because it would reveal if or how the mechanical properties are changed due to heat-treatment.

At last, optimizing the parameters for the welder would probably be of the most beneficial work from a shaping point view. The walls that were produced might have sufficient mechanical- and microstructural properties, although not perfect, but they lack the major property, which is the near-net shaping.

One way of optimizing the parameters is through simulations. Several such simulations have been performed to show how the heat is dissipated through the wall and into the base material, as it is build. Applying the findings from these simulations could very possibly improve the shaping- and the mechanical properties of the wall, which is greatly desired.

# 6 Conclusion

Three samples were produced of two different alloys, AA4020 and AA5083, namely. The AA4020 alloys were rich in silicon which was reflected in the mechanical properties, where the silicon rich areas of the sample were harder in average (≈42HV) than those areas of less silicon (≈34HV). The silicon rich areas were layers of crystalline silicon dendrites, which were not single crystals. In between the dendrites arms intermetallic phase occurred. Those who were identified were of $Al_6$(Mn,Fe) and Al(Mn,Fe)Si. The tensile tests showed similar values in both directions of extraction (i.e. vertical and horizontal). The second alloy was straighter in shape and taller ≈5.5cm, vs. ≈5cm of the AA4020-wall produced by the same equipment. The 5083 wall had small edge fractures and layers of intermetallic particles in between the weld bead boundary, causing the vertical tensile test to fail at short elongation. The AA5083 sample were the closest to the modelled shape. Homogenization of the AA5083 alloy made an uneven magnesium distribution to even out.

## List of references

[1] Kianian B. Wohlers Report 2017: 3D Printing and Additive Manufacturing State of the Industry, Annual Worldwide Progress Report: Chapters titles: The Middle East, and other countries. 22 ed. FORT COLLINS, COLORADO, USA: Wohlers Associates, Inc., 2017. 344 p.

[2] Ian D. Harris. May 2012. Additive Manufacturing: A Transformational Advanced Manufacturing Method. [Retrieved: 2017-02-28] Edison Welding Institute, Colobus, Ohio. Available from URL: http://www.asminternational.org/documents/10192/1900715/amp17005p25.pdf/489dfd7b-a9e6-4a92-8417-f5bd114f8eff/AMP17005P25

[3] "The printed world", The Economist, Feb. 10, 2011, Available from URL: https://www.economist.com/node/18114221

[4] Timothy J. Horn and Ola L. A. Harrysson. Overview of current additive manufacturing technologies and selected applications. Science in Progress (2012), 95(3), 255-282. Doi: 10.3184/003685012X13420984463047.

[5] Energy Efficiency and Renewable Energy;Advanced Manufacturing office. "Additve manufacturing: Pursuing the Promise". USA: U.S. Department of Energy. 2012-08. [Retrieved: 2018-05-13] Available from URL: https://www1.eere.energy.gov/manufacturing/pdfs/additive_manufacturing.pdf

[6] E. Herderick. Additive Manufacturing of Metals: A review. Colombus, Ohio, USA. Materials Science and Technology (MS&T); 16-20 oct. 2011. [Retrieved: 10.05.2018] Available from URL: https://www.asminternational.org/documents/10192/23826899/cp2011mstp1413.pdf/04f142d0-f1ca-44d4-8a10-891992e5529a

[7] Diego Manfredi, Flaviana Calignano, M. Krishnan, R. Canali, E. P. Ambrosio, S. Biamino, D. Ugues, M. Pavese and P. Fino. Additive Manufacturing of Al Alloys and Aluminium Matrix Composites (AMCs). 2014. [Retrieved 21.01.2017] DOI: 10.5772/58534.

[8] D. Herzog, V. Seyda, E. Wycisk, and C. Emmelmann. Additive manufacturing of metals. 07.07.2016. ; Acta Materialia 117 (2016) 371-392.

[9] W.J. Sames, F.A. List, S. Pannala, R.R Dehoff & S.S Babu (2016): The metallurgy and processing science of metal additive manufacturing, International Material reviews. Doi: https://doi.org/10.1080/09506608.2015.1116649

[10] ME Mecahnical. [Retrieved: 2017-03-22] Available from URL:https://me-mechanicalengineering.com/gas-metal-arc-welding-gmaw/

[11] Fronius International. Germany. [Retrieved 2018-05-15]. Available from URL: http://www.tps-i.com/en/cmt/

[12] Fronius International. Technologies. PDF: CMT – Cold Metal Transfer English. [Retrieved: 26.02.2017]. Available from URL: http://www.fronius.com/cps/rde/xbcr/SID-9E68A4AC-56F87E75/fronius_international/M_06_0001_EN_CMT_leaflet_44211_snapshot.pdf

[13] Evaluation of cold metal transfer (CMT) process for welding aluminium alloy. C. G. Pickin* and K. Young. Rapid Communication. 4/7/06 [Retrieved: 20.03.2017]; Institute of Materials, Minerals and Mining. Published by Maney. DOI: 10.1179/174329306X120886. Available from URL: https://weldconsultuk.files.wordpress.com/2013/01/cold-metal-transfer.pdf

[14] Fronius International. Germany. [Retrieved 2017-03-2017] Available from URL: http://www.fronius.com/cps/rde/xchg/SID-7620BF8C-F9FA885B/fronius_international/hs.xsl/79_23609_ENG_HTML.htm#.WNUo_xg0vVo

[15] K. Furukawa. New CMT arc welding process – welding of steel to aluminium dissimilar metals and welding of super-thin aluminium sheets. Weld Int. 2006-07; [Retrieved 2017-10-26]; vol. 30(6):440-445. Available from URL: https://www.tandfonline.com/doi/abs/10.1533/wint.2006.3598

[16] S. Selvi, A. Vishvaksenan, E. Rajasekar. Cold Metal Transfer (CMT) technology – A review. Defense Technology. 2017-08. [Retrieved 2018-04-10]; vol. 14: 28-44. Available from URL: https://www.sciencedirect.com/science/article/pii/S2214914717301022?via%3Dihub

[17]: A.S. Haselhuhn, M. W. Buhr, B. Wijnen, P. G Sanders, J. M. Pearce. Structure-property relationships of common aluminium weld alloys utilized as feedstock for GMAW-based 3-D metal printing. 06.05.2016. Materials Science & Engineering A 673(2016) 511-523. Elsevier.

[18] Mondolfo L.F. Aluminium-Magnesium, Aluminium-Manganese Alloys. London: Butterworth & Co (Publishers) Ltd; 1976. p. 806-841. ISBN: 0 408 70680 5

[19]: J. R. Davis. Alloying Understanding the Basics. Aluminum and Aluminum Alloys. 2001. ASM International. P:351-416. DOI: 10.1361/autb2001p351.

[20] J. Gilbert Kaufman. Introduction to Aluminium Alloys and Tempers. 2000-11. ASM International, Materials park, Ohio. ISBN: 0-87170-689-X. 2000; p.235.

[21] Johansen A. Microstructures and properties of Aluminium-Magnesium alloys with additions of manganese, zirconium and scandium. Trondheim: NTNU; 2000. 230 p. ISBN: 82-7984-048-6

[22] Promet. The effects of different alloying elements in aluminium alloy. [Internet] Hong Kong, CHN: Technology and Logistics center of Lee Kee group. [Retrieved 2018-05-13] Available from URL: http://prometlab.com/imgs/t_pdf/tech_e_6.pdf

[23] Charles Kittel. Introduction to Solid State Physics. 8th Edition. England: John Wiley & Sons, Ltd; 2004. 704p. ISBN: 9780471415268

[24] P. C. Hemmer. Faste Stoffers Fysikk. Bergen: Fagbokforlaget Vigmostad & Bjørke AS; 1987. 221p. ISBN: 978-82-519-0815-3

[25] Richard J. D. Tilley. Understanding Solids: The Science of Materials. West Sussex PO19 85Q, England: John Wiley & Sons Ltd; 2004. 593p. ISBN: 0 470 85276 3

[26] David B. Williams, C. Barry Carter. Transmission Electron Microscopy: A Textbook for Material Science. Part 1: Basics. 2nd edition. US: Springer Science+Business Media, LLC 1996; 2009. 760p. ISBN: 978-0-387-76502-0

[27] Louis-Victor de Broglie. Recherches Sur la Théorie des Quanta. Paris; 1925. 128p.

[28] Yang Leng. MATERIALS CHARACTERIZATION: Introduction to Microscopic and Spectroscopic methods. Hong Kong University of Science and Technology: John Wiley & Sons (Asia) Pte Ltd: Singapore; 2008. 337p. ISBN: ISBN 978-0-470-82298-2 (HB)

[29] JEOL Ltd. Ultra-high voltage electron microscope [Internet] jeol.co.jp. [Retrieved 2018-03-05] Available from URL: https://www.jeol.co.jp/en/words/emterms/search_result.html?keyword=UHV-EM

[30] Struers. Product data sheet: Silicon carbide grinding paper(SiC paper). [Internet] Copenhagen, Denmark; Struers. [Retrieved 2018-04-03] Available from URL: https://www.struers.com/Products/Grinding-and-Polishing

[31] Struers. Metallographic preparation of aluminium and aluminium alloys. [Internet] Copenhagen, Denmark: Struers ApS; 2016-02 [Retrieved 2018-04-19] Available from URL: https://www.struers.com/en/Material

[32] Struers. e-shop Struers. Safety Data Sheet Dp-Suspension P/M [Internet] Hørsholm, Denmark: DHI – Environment and toxicology; 2018-01-10 [Retrieved: 2018-04-19] Available from URL: https://e-shop.struers.com/US/EN/documents/40600255_Msds_US_English_606bac621b38740a35ce7bcc2453a8f5.aspx

[33] Struers. Lectropol. [Internet] Copenhagen, Denmark; Struers [Retrieved: 2018-04-3] Available from URL: https://www.struers.com/en-GB/Products/Electrolytic-Preparation/Electrolytic-equipment/LectroPol

[34] Struers. Preparation of ferrous metals for electron backscatter diffraction (EBSD) analysis. [Internet] Copenhagen, Denmark; Struers [Retrieved: 2018-03-07] Available from URL: https://www.struers.com/en/Material

[35] Ünlü N. Preparation of high quality Al TEM specimens via double-jet electropolishing technique [electronic article]. Materials Characterization 59 (2008) 547-553. 2007 Feb. [Retrieved: 2018-02-28]; Available from: https://www.sciencedirect.com/science/article/pii/S1044580307001301

[36] H. You Kim, T. Y. Park, S. W. Han, H. M. Lee. Effects of Mn on the crystal structure of α-Al(Mn,Fe)Si particles in A356 alloys. JCrysGro 2006-02. [Retrieved 2019-05-02]; vol(291) p.207-211. Doi: 10.1016/j.jcrysgro.2006.02.006

[37] Y. Liu, G. Huang, Y. Sun, L. Zhang, Z. Huang, J. Wang and C. Liu. Effect of Mn and Fe on the formation of Fe- and Mn-Rich Intermetallics in Al-5Mg-Mn Alloys Solidified Under Near-rapid cooling. MDPI. 2016-01-29. [Retrieved: 2018-05-12]; 9(2), p.88. Doi: 10.3390/ma9020088.

[38] A. Hassan, K. Ranjbar, S. Sami. Microstructural evolution and intermetallic formation in Al-8wt% Si-0.8wt% Fe alloy due to grain refiner and modifier additions. Int.JMMM. 2012-08. [Retrieved: 2018-05-12]; vol.19(8) p.739. Doi: 10.1007/s12613-012-0621-3

[39] M. Svoboda, J. Janovec, M. Jenko and A. Vrankovic. The Characterization of Intermetallic-Compound Particles In An Annealed Al-Mg-Cr-Fe Alloy. MTAEC9 2004-11; [Retrieved 2018-05-03]; 38(6)289. ISSN: 1580-2949. Available from URL: http://mit.imt.si/Revija/izvodi/mit046/svoboda.pdf

[40] M.V. Kral. A crystallographic identification of intermetallic phases in Al-Si alloys. Mat. Let. 2005-08 [Retrieved 2018-05-12]; vol.30(18): p.2271-2276. Available from doi: https://doi.org/10.1016/j.matlet.2004.05091

[41]: C. J. Simensen, P. Fartum and A. Andersen. Analysis of Intermetallic Particles in Aluminium by Dissolution of the Sample in Buthanol. Fresenius Z. anal. Chemie 319 (1984) p. 286-292.

# Appendix

## Appendix A-1

The produced TEM samples by jet-polishing were given the names top, middle and bottom by the origin at the sample wall of AA5083_S3. The parameters used for the different samples is shown in table A.1 below

**Table A.1: Jet-polishing parameters used on the TEM samples of wall AA5083_S3:**

| Place in box: | Prøveopphav: | Temperature [°C]: | Voltage [V]: | Flowrate: | Sensitivity: |
|---|---|---|---|---|---|
| B2 | ”bottom1” | -25±2 | 30 | 9 | 2 |
| B4 | ”bottom2” | -25±2 | 30 | 8 | 2 |
| B6 | ”bottom3” | -25±2 | 30 | 10 | 1 |
| C1 | ”top1” | -25±2 | 40 | 8 | 3,5 |
| C3 | ”top2” | -25±2 | 40 | 7 | 3,5 |
| C5 | ”top3” | -25±2 | 15 | 7 | 3,5 |
| D2 | ”middle1” | -30±2 | DNF @15[3] | 7 | 3,5 |
| D4 | ”middle2” | -30±2 | 30 | 7 | 3,5 |
| D6 | ”middle3” | -30±2 | 30 | 7 | 3,5 |
| D8 | ”middle4” | -25±2 | 30 | 7 | 3,5 |
| D10 | ”middle5” | -25±2 | 30 | 8 | 3,5 |
| C7 | ”middle6” | -25±2 | 30 | 8 | 3 |

The following images (figure A.1) were acquired with the Hitachi TM3000 TableTop SEM and shows the result of the samples after jet polishing. The naming is corresponding to the slot it was placed in the TEM-sample box.

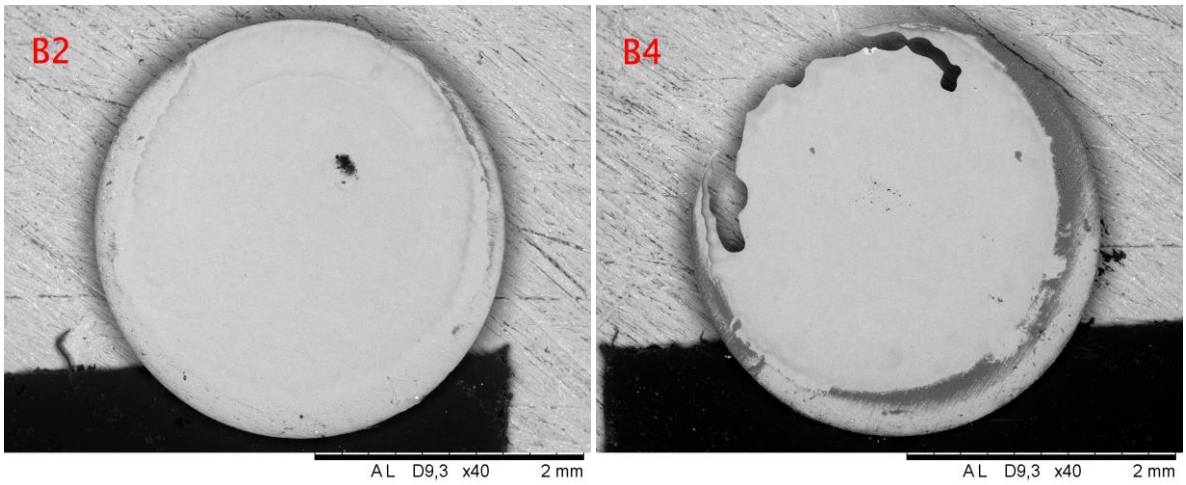


[3] Not completed at 15V. The voltage was changed to create a hole, that is, the value is not consistent.

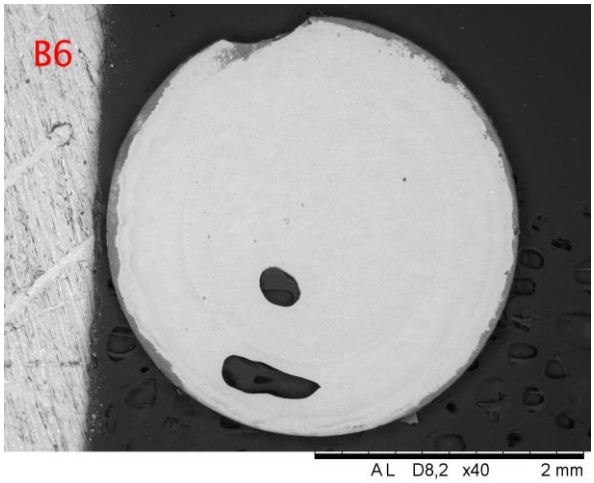
B6
AL D8,2 x40 2 mm

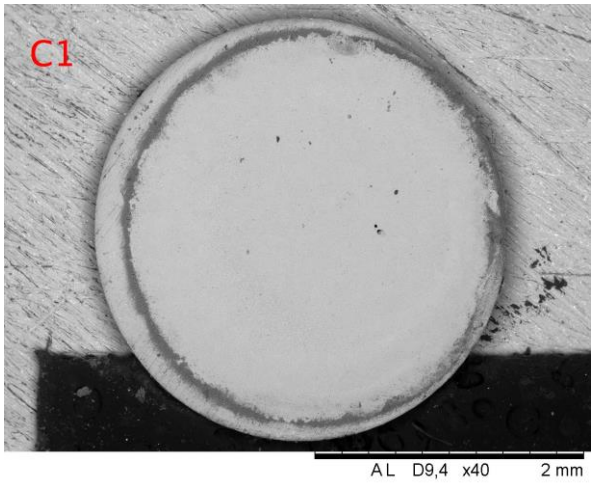
C1
AL D9,4 x40 2 mm

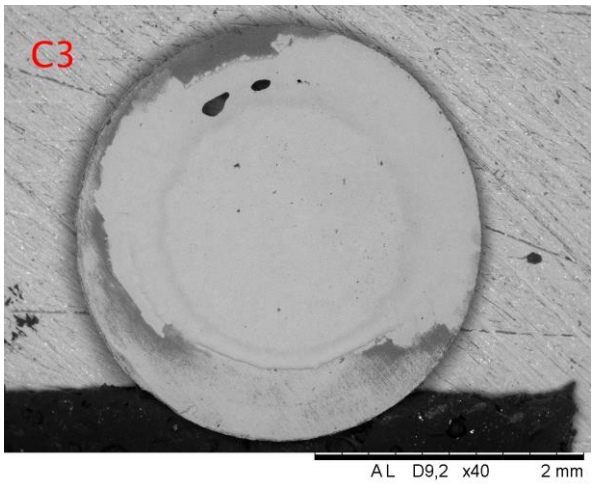
C3
AL D9,2 x40 2 mm

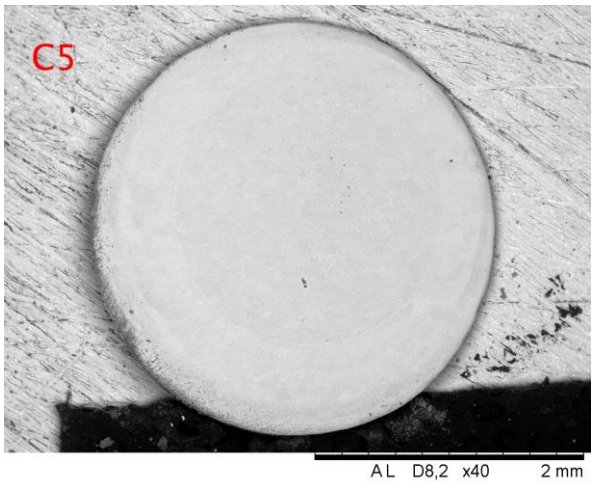
C5
AL D8,2 x40 2 mm

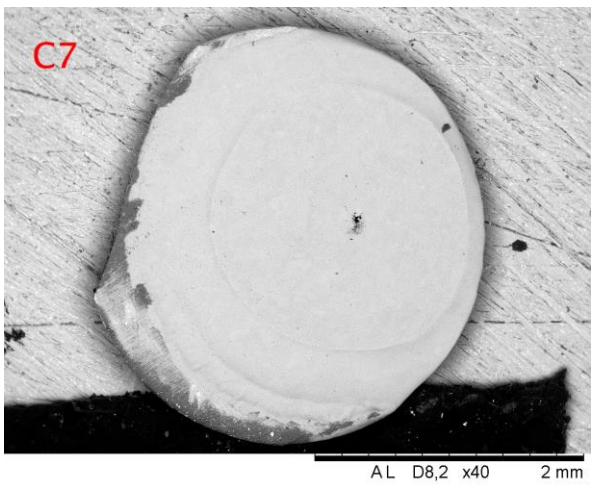
C7
AL D8,2 x40 2 mm

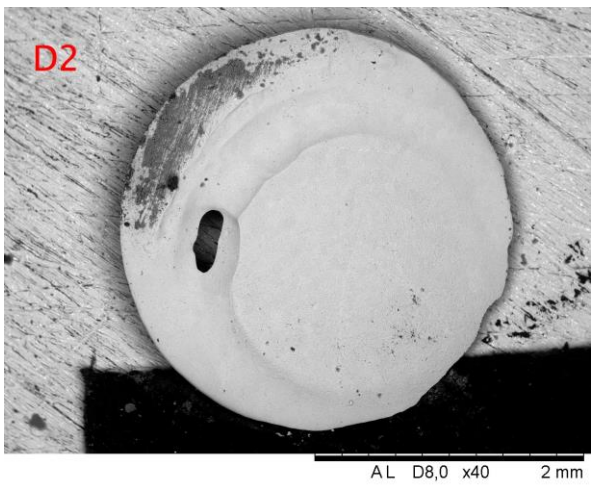
D2
AL D8,0 x40 2 mm

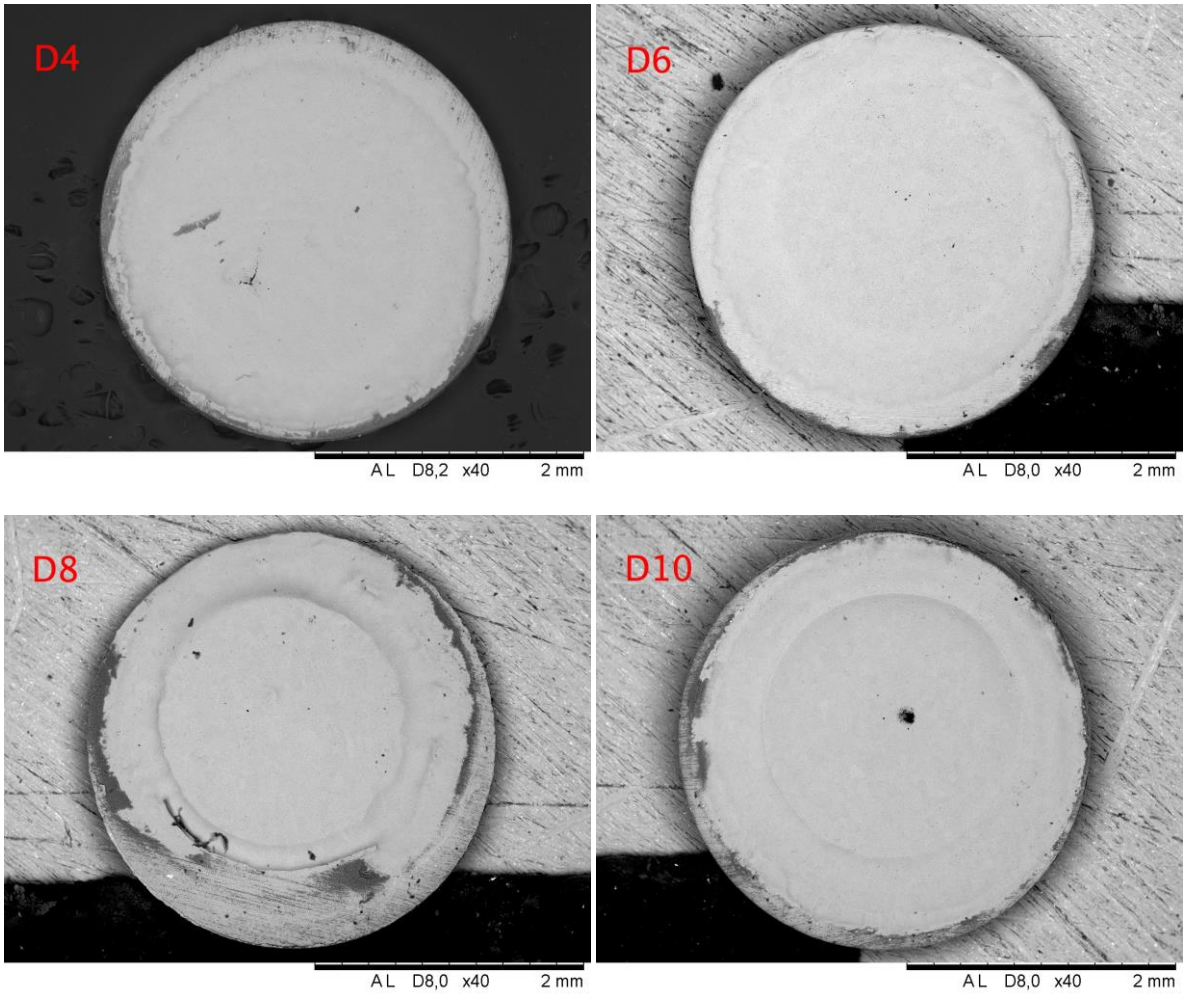


Figure A.1: SEM images of the produced samples of wall AA5083_S3

## Appendix A-2

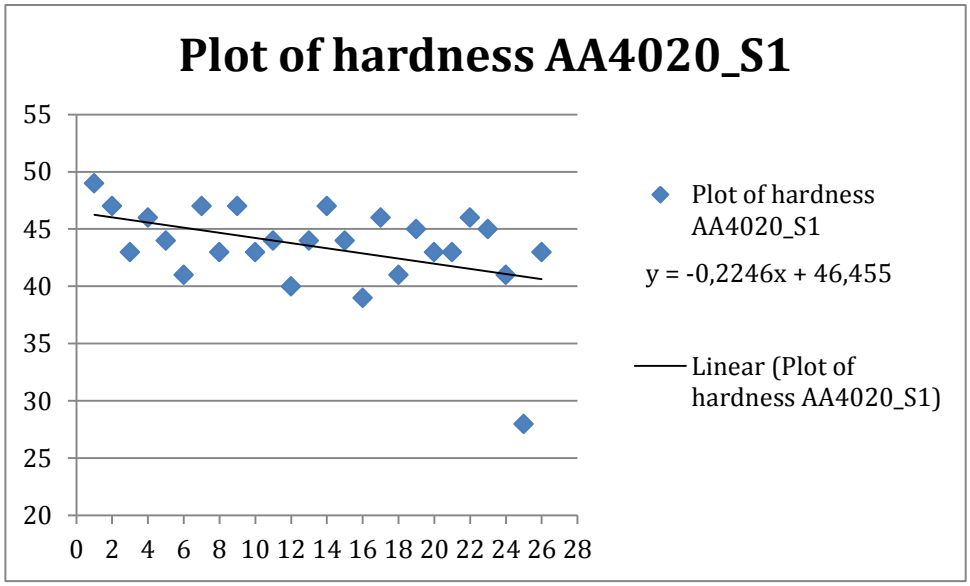


Figure A.2: scatter plot of the hardness of wall AA4020_S1 with linear regression line.

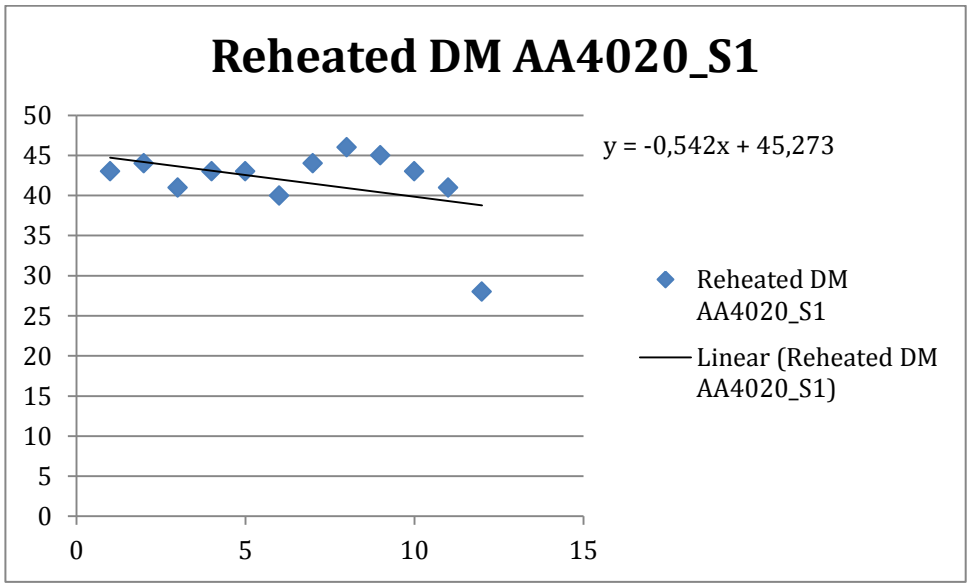


Figure A.3: scatter plot of the hardness at the reheated deposited material (DM) of wall AA4020_S1 with linear regression line.

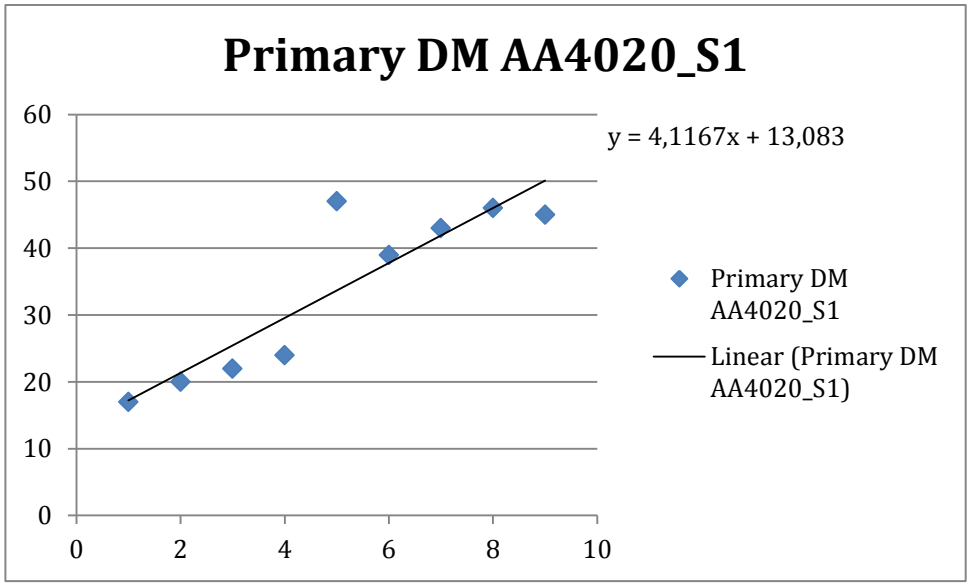


Figure A.4: scatter plot of the hardness at the reheated deposited material (DM) of wall AA4020_S1 with linear regression line.

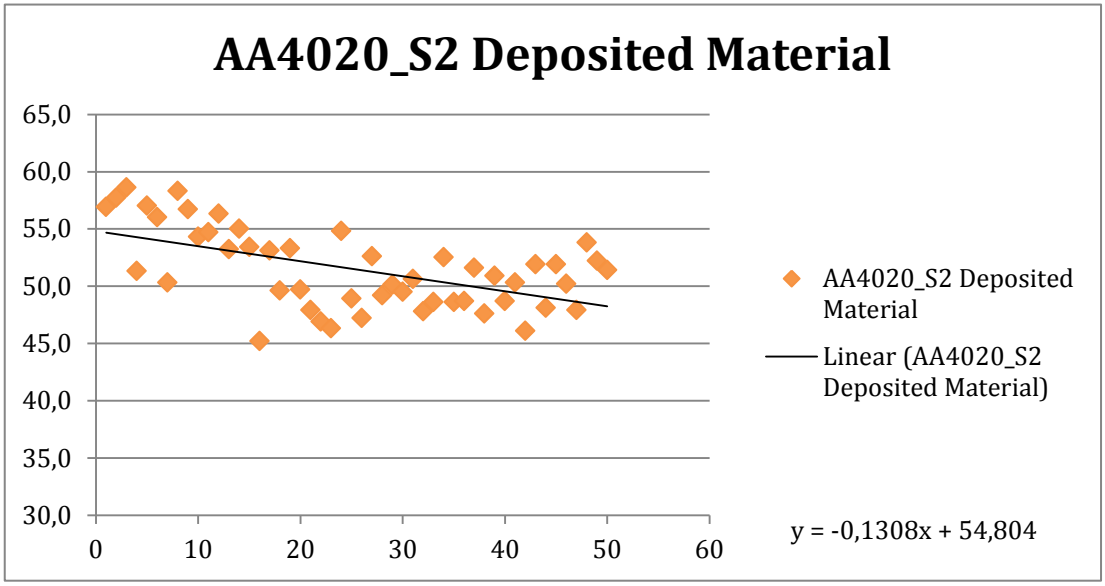


Figure A.5: scatter plot of the hardness at the complete deposited material (DM) of wall AA4020_S2 with linear regression line.

## Appendix A-3:

### Grain boundary 1 at FIB sample:

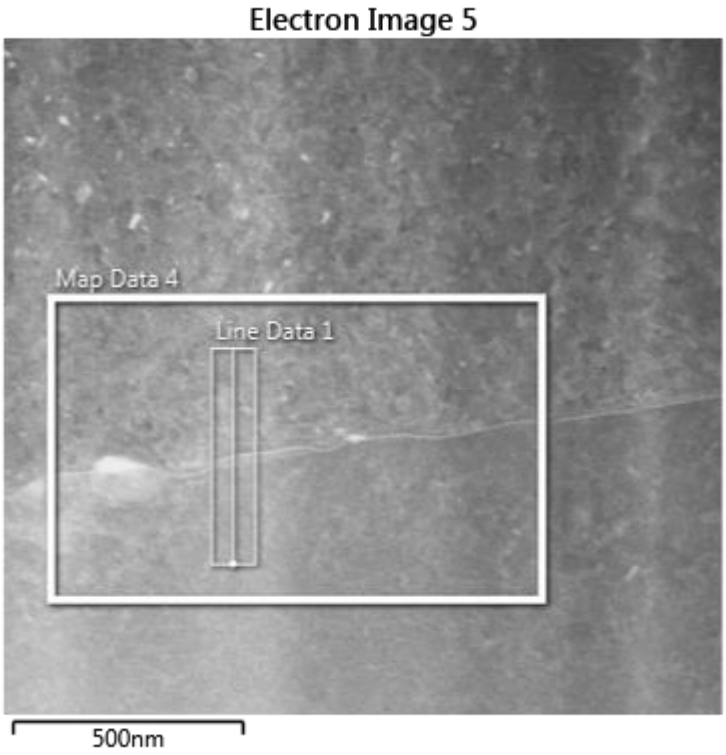


Figure A.6: STEM image a grain boundary.

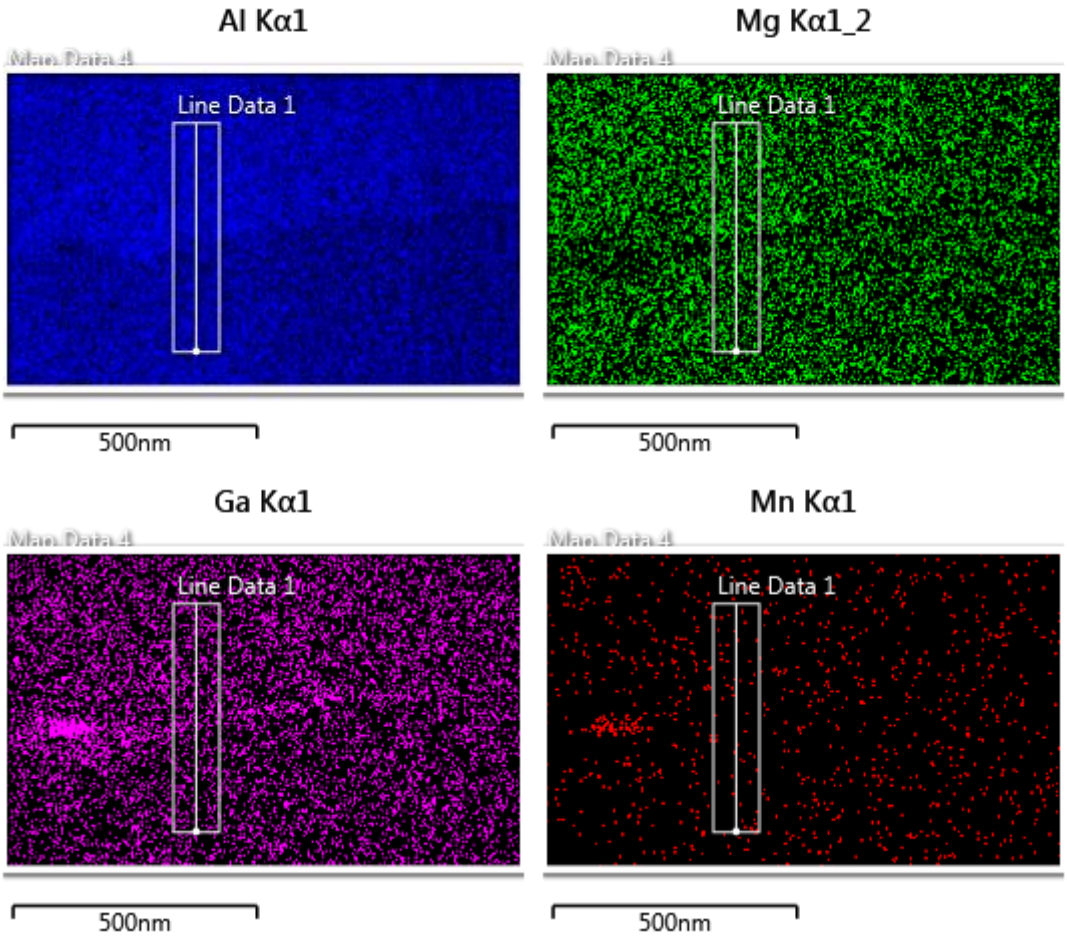


Figure A.7: elemental maps of the grain boundary in fig. A.6 showing gallium at the grain boundary.

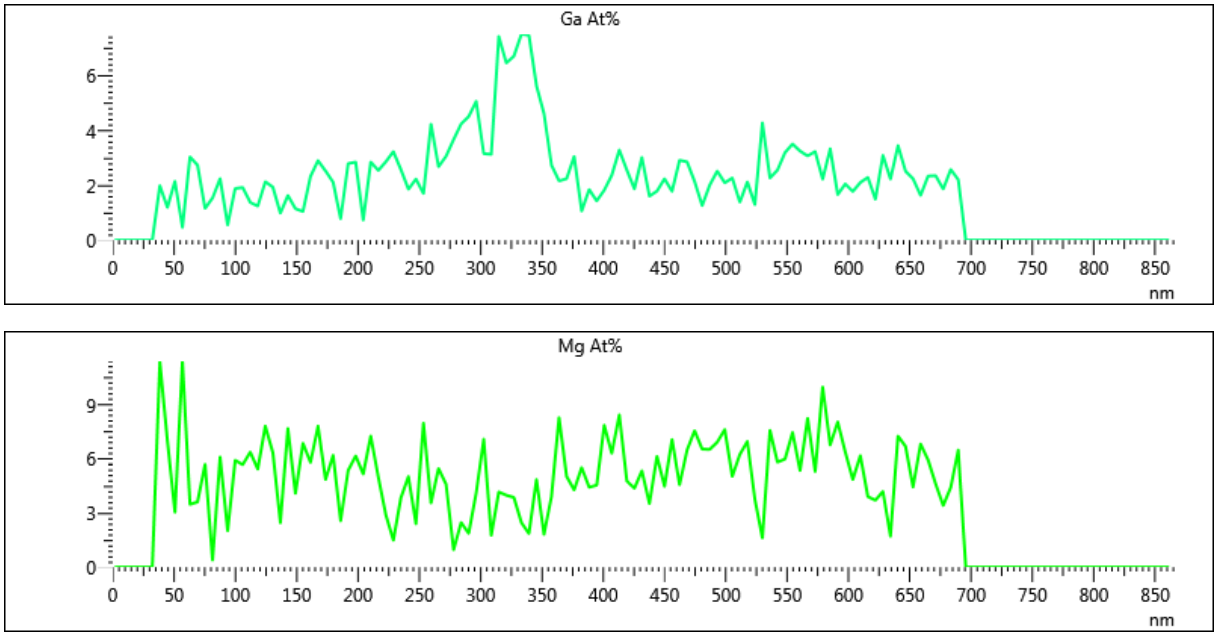

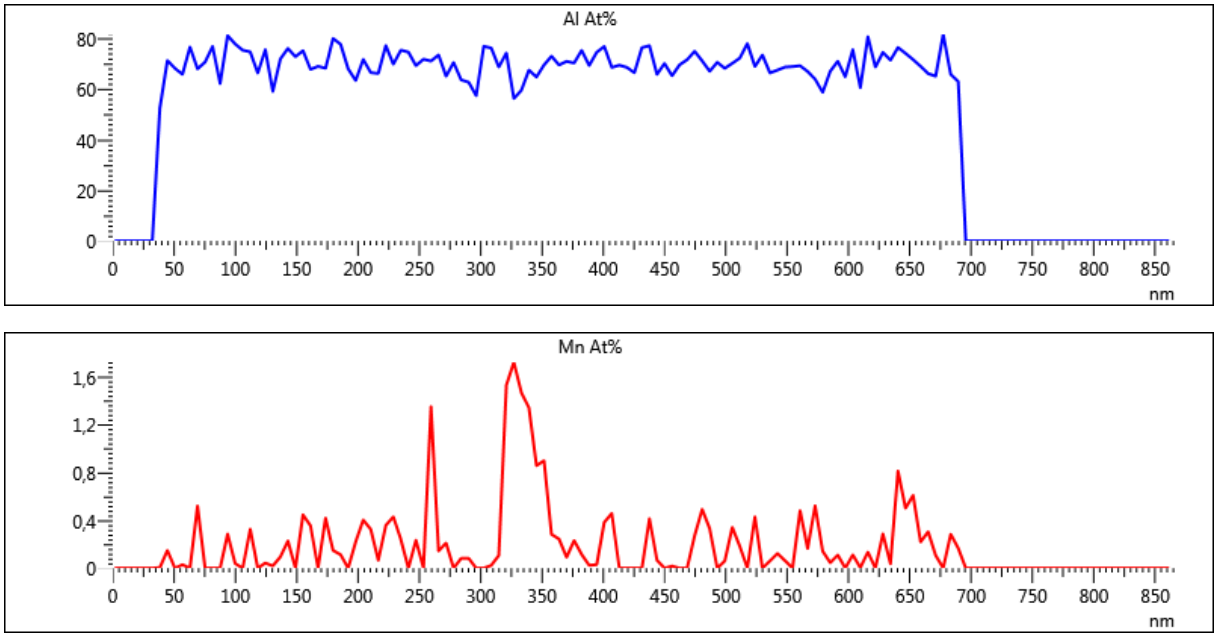


Figure A.8: Linescan plots over the grain boundary in figure A.6, showing an gallium increase at the grain boundary caused by the FIB sample preparation.